University of Alberta

Functional Magnetic Resonance Imaging: Determination of its Feasibility at 4.7T and Applications in Parkinson's Disease Research at 1.5T

by

Alexander Holden

A thesis submitted to the Faculty of Graduate Studies and Research in partial fulfillment
of the requirements for the degree of Master of Science

Department of Electrical and Computer Engineering
Department of Biomedical Engineering

Edmonton, Alberta

Spring 2004

Library and
Archives Canada

Published Heritage
Branch

395 Wellington Street
Ottawa ON K1A 0N4
Canada

Bibliothèque et
Archives Canada

Direction du
Patrimoine de l'édition

395, rue Wellington
Ottawa ON K1A 0N4
Canada

Your file Votre référence
ISBN: 0-612-96486-8
Our file Notre référence
ISBN: 0-612-96486-8

The author has granted a non-exclusive license allowing the Library and Archives Canada to reproduce, loan, distribute or sell copies of this thesis in microform, paper or electronic formats.

The author retains ownership of the copyright in this thesis. Neither the thesis nor substantial extracts from it may be printed or otherwise reproduced without the author's permission.

L'auteur a accordé une licence non exclusive permettant à la Bibliothèque et Archives Canada de reproduire, prêter, distribuer ou vendre des copies de cette thèse sous la forme de microfiche/film, de reproduction sur papier ou sur format électronique.

L'auteur conserve la propriété du droit d'auteur qui protège cette thèse. Ni la thèse ni des extraits substantiels de celle-ci ne doivent être imprimés ou aturement reproduits sans son autorisation.

In compliance with the Canadian Privacy Act some supporting forms may have been removed from this thesis.

While these forms may be included in the document page count, their removal does not represent any loss of content from the thesis.

Conformément à la loi canadienne sur la protection de la vie privée, quelques formulaires secondaires ont été enlevés de cette thèse.

Bien que ces formulaires aient inclus dans la pagination, il n'y aura aucun contenu manquant.

Canada

Reproduced with permission of the copyright owner. Further reproduction prohibited without permission.

Abstract

The objectives of this thesis are two-fold: the investigation of Parkinson's disease using functional magnetic resonance imaging (fMRI) at 1.5T and determination of the feasibility of fMRI at 4.7T. At 1.5T, following paradigm and triggering development, two separate fMRI experiments were conducted. The first utilized a conventional block-design paradigm to study basal ganglia behaviour and the other an event-related paradigm to study response inhibition. The results from these studies suggest that Parkinson's patients use a different cortical network to process inhibition stimuli than age-matched healthy controls, and also that several nuclei in the Parkinsonian basal ganglia appear to be functionally impaired during motor switching tasks. At 4.7T, images collected of phantoms and in vivo suggest that the magnetic field homogeneity is not presently sufficient for echo-planar functional imaging. However, using the conventional gradient echo sequence, under comparable conditions, twice the BOLD signal was observed at 4.7T compared to 1.5T.

Acknowledgements

Several people deserve special thanks for their efforts and support relating to this Masters degree. I would foremost like to thank my parents for their encouragement, advice and for supporting me through difficult times. I would also like to thank Dr. Alan Wilman for his guidance and for always making time to answer my questions. Thank-you to all those who volunteered for the various studies described in this thesis, especially Chilo Bonilla, Yusuf Bhagat, and Amir Eissa who volunteered on numerous occasions. Finally, a special thanks to Atiyah Yahya for answering innumerable questions over the past two and a half years.

Table of Contents

Chapter 2: The Physics Behind Magnetic Resonance Imaging

Chapter 3: The BOLD mechanism

Chapter 4: Paradigm Designs

Chapter 5: Statistical Parametric Mapping

Chapter 6: Parkinson's Disease

Chapter 7: Parkinson's Experiments

Chapter 8: Echo-Planar Imaging

Chapter 9: Functional Imaging at 4.7T

List of Tables

List of Figures

Symbols

ψ	signal to noise ratio
φ	phase angle
θ	phase angle
μ	magnetic dipole moment
γ	magnetogyric ratio
ω_0	Larmor frequency
ω_{eff}	effective precession frequency
χ	magnetic susceptibility parameter
$\hbar$	Planck's constant divided by 2π
ρ	refers to the rotating frame of reference when a subscript and to the proton spin density when not a subscript
σ	chemical shift shielding constant
$\delta\omega$	frequency shift due to the chemical shift effect
μ_0	magnetic constant (permeability of space)
Δ	a change in some variable
$\Omega(x,y,z,t)$	the angular frequency component corresponding to $\mathbf{b}(x,y,z,t)$
$\Phi(x,y,z)$	the angular frequency component corresponding to $\beta(x,y,z)$.
τ	the duration of the phase encode gradient
ΔB_0	magnetic field imperfections
Δf	frequency shift
$\mathbf{b}(x,y,z,t)$	local time-dependent magnetic field disturbance
$\beta(x,y,z)$	local non-time-dependent magnetic field disturbance
$\mathbf{B_0}$	static magnetic field
$\mathbf{B_1}$	radio frequency magnetic field
$\mathbf{B_{eff}}$	effective static magnetic field
bw	pixel-wise bandwidth
BW	bandwidth
d_{cs}	chemical shift in mm

d_{csp}	chemical shift in pixels
dB	decibels
E	energy
G	gradient magnetic field
$\mathbf{I}$	spin angular momentum
k	Boltzmann's constant
$\mathbf{M}$	net magnetization vector
$\mathbf{M_0}$	longitudinal component of the net magnetization vector before $\mathbf{B_1}$
M_x	x-component of transverse magnetization
M_y	y-component of transverse magnetization
M_{xy}	transverse magnetization
$M_{x\rho}$	transverse magnetization (x_ρ-component)
$M_{y\rho}$	transverse magnetization (y_ρ-component)
$M_{z\rho}$	transverse magnetization (z_ρ-component)
$n\downarrow, n\uparrow$	the number of spins pointing antiparallel or parallel to $\mathbf{B_0}$ respectively
R_2	transverse relaxation rate
R_2^*	apparent transverse relaxation rate
t	time
T_{acq}	the total acquisition time (time to acquire a single k_y line)
T_{RO}	the readout or acquisition time (time to acquire a single k_x line)
t_{rf}	time of application of the r.f. pulse $\mathbf{B_1}$
T	torque or temperature
T_1	longitudinal relaxation time
T_2	transverse relaxation time (irreversible)
T_2'	transverse relaxation time (reversible)
T_2^*	apparent transverse relaxation time (reversible + irreversible)
Y	oxygen saturation of hemoglobin

Abbreviations

ADC	analog to digital conversion
BA	brodmann area
BG	basal ganglia
BOLD	blood oxygenation level dependent
bw	pixel-wise bandwidth
BW	bandwidth
CBF	cerebral blood flow
CBV	cerebral blood volume
$CMRO_2$	cerebral metabolic rate of oxygen consumption
$CMR_{glucose}$	cerebral metabolic rate of glucose consumption
CN	caudate nucleus
CSF	cerebrospinal fluid
DOF	degrees of freedom
efMRI	event-related functional magnetic resonance imaging
EMF	electromotive force
EPI	echo planar imaging
ERP	event-related potential
EV	extravascular
FFX	fixed effects
FID	free induction decay
fMRI	functional magnetic resonance imaging
FOV	field of view
FT	Fourier transform
FWHM	full width half maximum
GE	gradient echo
GP	globus pallidus
HRF	hemodynamic response function
HbO_2	oxyhemoglobin

Hb	deoxyhemoglobin
IFT	inverse Fourier transform
ISI	interstimulus interval
IV	intravascular
L	left
MIP	maximum intensity projection
MNI	Montreal Neurological Institute
MRI	magnetic resonance imaging
PD	Parkinson's disease
PE	phase encode
PET	positron emission tomography
PFC	prefrontal cortex
PSF	point spread function
R	right
RBC	red blood cell
RFX	random effects
RO	readout
ROI	region of interest
SE	spin echo
SNc	substantia nigra pars compacta
SNr	substantia nigra pars reticulata
SPM	statistical parametric map
ssEPI	single-shot EPI
SVC	small volume corrected
TE	echo time
TR	repetition time

Chapter 1

Introduction

Functional magnetic resonance imaging primarily uses the blood oxygenation level dependent or BOLD physiological contrast mechanism. Although a connection had been established between a measurable proton relaxation rate (T_2) and the oxygenation level decades ago (Thulborn 1982), demonstrations showing that intrinsic blood oxygenation could create image contrast depicting functional activation in the brain occurred much more recently (Ogawa 1992; Kwong 1992; Bandettini 1992). As evidenced by these dates, the field of functional magnetic resonance imaging (fMRI) is still in its infancy with countless opportunities for study.

One such avenue of study yet to be explored fully, is the use of higher strength magnetic fields for functional imaging. Stronger magnetic fields enable greater signal to noise, greater BOLD sensitivity and increased specificity. Another foray is the application of fMRI to patients in order to better understand disease-related mental processing aberrations inducing characteristic symptoms or behaviours. This thesis is intended to advance the field of functional magnetic resonance imaging along two separate avenues: development/demonstration of fMRI at 4.7T and the clinical application of fMRI in order to investigate the functional role of the basal ganglia in Parkinson Disease.

This thesis begins with an introduction to the fundamentals of Magnetic Resonance Imaging (Chapter 2). The chapter progresses from the initial placement of the sample or subject in the magnetic field through to image generation. Topics presented include: the formation of an observable magnetic resonance signal, relaxation mechanisms leading to signal decay and controllable image contrast, and spatial encoding and slice selection.

Chapters 3 to 6 set the stage for the ensuing experiments. Chapter 3 continues the discussion of image formation, explaining the physiological basis by which functional activation can be mapped. This is known as the Blood Oxygenation Level Dependent (BOLD) mechanism. Finally, two different functional magnetic resonance imaging experimental designs are compared: event-related and epoch-based (Chapter 4).

Chapter 5 explores the statistical method used to analyze the data. This section summarizes the pre-processing and analysis steps used by the statistical package SPM99. Chapter 6 presents the final piece of background information. It prepares the reader for the clinical work of this thesis through an overview of Parkinson's Disease. This section looks at both characteristics of the disease and at previous functional imaging findings.

One of the primary focuses of this thesis is the investigation of the behaviour of the basal ganglia in Parkinson's patients compared to healthy control subjects (Chapter 7). This was studied using two different experimental approaches: block based and event-related fMRI.

Chapter 8 introduces echo-planar imaging. It explores both the advantages and disadvantages of this fast imaging technique.

Chapter 9 contains the second focus of this thesis, namely, it questions whether or not functional imaging at 4.7T is either feasible or advantageous. This question is ultimately answered by comparing the results from a simple motor experiment conducted using the same subjects, at both 1.5T and 4.7T.

This document concludes by exploring future extensions of the research presented in this thesis.

Chapter 2

The Physics Behind Magnetic Resonance Imaging

2.1 Introduction

This chapter introduces magnetic resonance imaging to the reader. It begins with a simple overview of the steps involved in a magnetic resonance experiment, then proceeds to the concept of relaxation and its importance in imaging. Next, echo production, which is a constituent of all imaging sequences is explained. The chapter concludes by presenting topics specific to imaging, namely spatial encoding, k-space and slice selection. After completing this chapter the reader will be able to appreciate the basic steps involved in creating a magnetic resonance image.

In magnetic resonance imaging (MRI), the measurable signal comes from nuclei. Not all nuclei, however are suitable for imaging. In order for a nucleus to be viable for MRI, it must have a net magnetic moment. Without going into great detail, a net magnetic moment is created by internal circulating currents within the nucleus. If the nucleus contains an even number of protons and neutrons, these currents cancel, and the nucleus has no magnetic moment. This is not the case in atomic nuclei with either an odd number of protons and or neutrons. Furthermore, it will be shown later that net unpaired electronic spins within certain ions also have magnetic moments, in this case ionic magnetic moments, although these ions are relatively scarce. Most elements have isotopes with a net magnetic moment, but these isotopes must also be present in sufficient quantities in order to be detected. Examples of such isotopes are given in the table below, which also quantifies their "Biological" and "Natural" abundances. Biological abundance is the fraction of one type of atom in the human body, while Natural abundance is the prevalence of an isotope for a given element.

Table 2-1. Properties of some nuclei suitable for NMR research (Hornak 2000)

Element	**Biological abundance**	**Useful Isotopes**	**Natural Abundance**	**Unpaired protons**	**Unpaired Neutrons**	**γ (MHz/T)**
Hydrogen	0.63	^{1}H	99.985	1	0	42.58
		^{2}H	0.015	1	1	6.54
Carbon	0.094	^{13}C	1.11	0	1	10.71
Nitrogen	0.015	^{14}N	99.63	1	1	3.08
Sodium	0.00041	^{23}Na	100	2	1	11.27
Phosphorus	0.0024	^{31}P	100	0	1	17.25

Of those in the body, the unpaired proton of hydrogen is the most prolific. As a result, the majority of MRI research involves imaging hydrogen.

2.2 Stages of a Magnetic Resonance Experiment

Magnetic Resonance Imaging (MRI) is a non-invasive procedure that may be broken down into three stages: preparation, excitation and acquisition.

2.2.1 Preparation

The body can be modeled as a bag of protons, where each is a magnetic dipole (or magnetic moment) oriented in a random direction at thermal equilibrium. If this bag is then placed inside a static, uniform magnetic field (denoted $\mathbf{B_0}$), the proton dipoles will orient themselves in one of two energy states, either parallel or antiparallel to this field. This behaviour arises from quantum mechanics which governs the possible orientations of atoms in a static magnetic field through a parameter known as the atoms' nuclear spin angular momentum (**I**). For protons this value is ½, thus the proton magnetic dipoles will exist in one of two orientations when placed in a static magnetic field: parallel or antiparallel to that field. The parallel orientation is the lower energy, hence the preferred state. The ratio of populations of protons within the two energy states is given by classical Maxwell-Boltzmann statistics as (see mathematical details below):

$$n\downarrow/n\uparrow = \exp(-\Delta E/kT) \quad (\mathbf{B_0}\text{ points } \uparrow). \qquad (1)$$

Finally, the individual magnetic moments can be combined and expressed as a single resultant vector, M_z, that points in the direction of $\mathbf{B_0}$. Figure 2-1 illustrates these concepts.

2.2.1.1 Preparation - Mathematical Details

Two characteristics of the proton are its spin angular momentum $I\hbar$ and the fraction of the magnetic dipole moment μ along the magnetic field direction, which are related by

$$\mu = \gamma I \hbar \qquad (2)$$

where γ = the magnetogyric ratio, a constant that is specific to a nuclear species (4257 Hz/G for protons)
$\hbar$ = Planck's constant.

The potential energy of a proton within the external field is given by

$$E = -\boldsymbol{\mu} \bullet \mathbf{B_0}$$
$$= -\gamma I \hbar B_0 \qquad (3) \qquad \text{(by Eqn (2))}$$

At this point, quantization rules concerning angular momentum reveal that the eigenvalues of **I** are mI = $\pm 1/2$, and thus

$$E = \pm\gamma\hbar B_0/2 \qquad (4)$$

where the energy of the higher (antiparallel) state is $+\gamma\hbar B_0/2$ and that of the lower (parallel) state is $-\gamma\hbar B_0/2$.

The resonance frequency is defined as $\omega_0 = \gamma B_0$. Thus the energy difference between the parallel and antiparallel states is

$$\Delta E = \gamma\hbar B_0 = \hbar\omega_0 \qquad (5)$$

The ratio of populations of protons within the two energy states is given by classical Maxwell-Boltzmann statistics as

$$n\downarrow/n\uparrow = \exp(-\Delta E/kT) \quad (\mathbf{B_0} \text{ points } \uparrow)$$

At room temperature (300K) and 1.5T there is roughly a 1 ppm difference for protons between the two orientations.

Thermal Equilibrium

After Application of $\mathbf{B_0}$

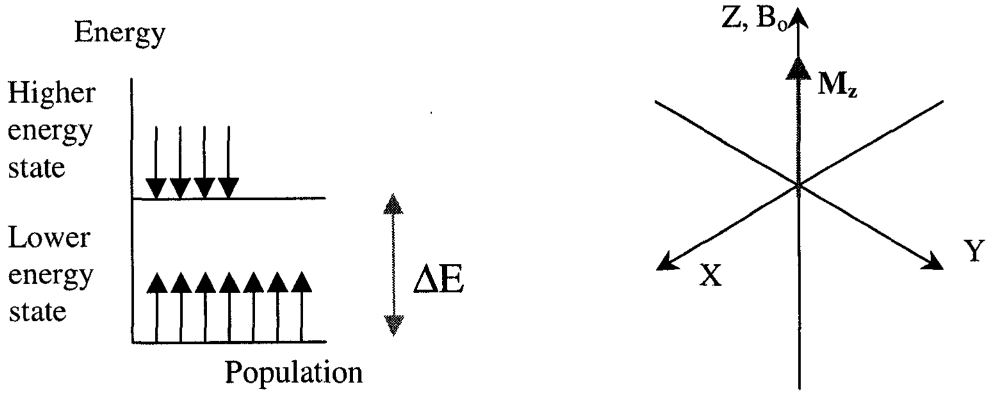

Distribution of Protons within $\mathbf{B_0}$

Net Magnetization Vector (M_z) Produced by the summation of all Magnetic Dipoles

Figure 2-1. Orientations of proton magnetic dipoles at different stages during preparation (Allen 1992)

2.2.2 Excitation

Of fundamental importance to this section is the equation

$$T = \mathbf{M} \times \mathbf{B} \qquad (6)$$

which relates torque (T) to the cross product of a vector (**M**) and the magnetic field (**B**).

In the Excitation stage, a second magnetic field (**B**$_1$) is applied to the system. Compared to **B**$_0$ which is static, uniform, and strong, **B**$_1$ is time-dependent, circularly polarized and much weaker in strength. This secondary field rotates in the negative sense at the frequency $\omega_0 = \gamma B_o$ (the Larmor frequency), and is oriented perpendicular to **B**$_0$ and M_z. As a result, **B**$_1$ applies a torque to the net magnetic moment M_z, pulling it down into the transverse plane in a spiral trajectory. Once the magnetization is tipped into the transverse plane, **B**$_1$ is switched off. The magnetization, now denoted M_{xy}, is perpendicular to **B**$_0$ and experiences a torque from the static magnetic field. This torque causes M_{xy} to precess about the z-axis in the same sense (in the negative direction - from the y to x axis) and at the same frequency as **B**$_1$ (i.e. the Larmor frequency). (See Appendix A for further details)

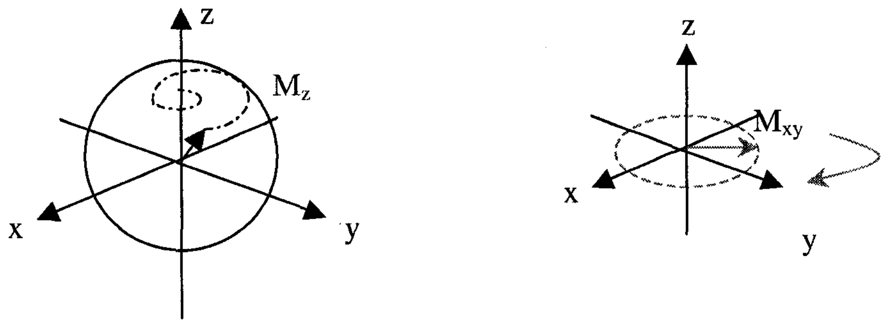

B$_1$ pulling M_z into the transverse plane via spiral trajectory

Rotation at ω_0 due to the torque effect of **B**$_0$ on M_{xy}

Figure 2-2. The Torque Phenomena in the Excitation Stage (Allen 1992).

2.2.3 Acquisition

The Excitation phase results in a metamorphosis of the net Magnetization vector into a rotating vector in the x-y plane. If a stationary coil is placed around this rotating (time-dependent) magnetization vector, the vector will induce a sinusoidal EMF (decaying in the presence of relaxation), oscillating at ω_0 in the coil (Faraday's Law). Alternatively, one may think of the resultant EMF as a delta function in frequency space, centred at ω_0

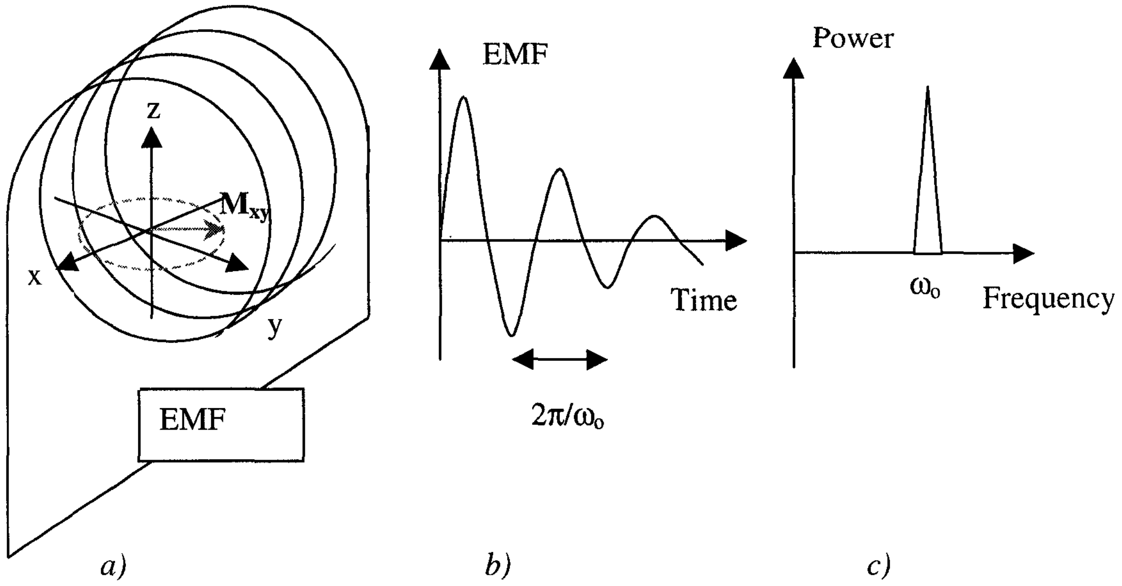

Figure 2-3. a) Rotating transverse magnetization is received within the stationary coil as an EMF; b) received EMF in time domain and, c) received EMF in the frequency domain (Allen 1992)

The above procedure is not yet capable of forming an image. It is merely part of the image formation process. To produce an image, the concepts of spatial encoding and contrast mechanisms first need to be addressed.

Following perturbation into the xy plane, the net magnetization vector will not precess indefinitely about the z-axis but rather returns to equilibrium via two separate, simultaneous mechanisms – T_1 and T_2 relaxation.

2.3 Relaxation

The two relaxation mechanisms are related yet separate, thus they will be dealt with individually. The first is T_1 relaxation, also known as longitudinal or spin-lattice relaxation.

2.3.1 T_1 Relaxation

As mentioned in the introduction, magnetic moments arise within atoms containing unpaired protons and or neutrons and also from net unpaired electrons within ions. It was also previously mentioned that protons are prolific in the body. Unpaired electrons on the other hand are rare, given that most biological molecules have fully paired electrons (covalently bonded), as do most ions (including Na^+, Cl^- etc.) A source of biological unpaired electrons does exist, however, in the form of select transition ions including Fe^{2+}, and Fe^{3+}. These particles have a net ionic magnetic moment resembling that of protons, but about 700 times the strength.

Magnetic moments' role in T_1 relaxation is similar to that of B_1 during Excitation. Remember that during Excitation a time-dependent (fluctuating) magnetic field at the Larmor frequency induces reversals in spin states culminating in a change in M_z. Net magnetic moments exude magnetic fields. The random thermal movement of molecules possessing moments creates microscopic fluctuating magnetic fields which occupy a whole range of frequencies. Furthermore, even the strength of the weak proton dipole is comparable to that of some $\mathbf{B_1}$ pulses ($\sim 10^{-5}$ to 10^{-4} T). As a result, random fields in the range of the Larmor frequency act as $\mathbf{B_1}$ did, eliciting transitions in spin states.

Despite the same underlying mechanism, fluctuating fields induce signal decay and not excitation (like $\mathbf{B_1}$) due to a difference in energy source. The transition probability between low and high energy spin states is the same for either direction flip. The reason that $\mathbf{B_1}$ application yields excitation is that at equilibrium more protons exist in the lower state and thus more flips occur to the higher state. In the relaxation process, thermal phonons are responsible for the motion-induced fluctuations. The phonons populate their energy states with a progressively larger density at lower energy states. In addition, this density dwarfs that of the nuclear states (with parallel and antiparallel states for protons), giving the thermal system a greater thermal capacity. The end result is that the thermal energy system removes energy from the nuclear energy system until the two reach an equivalent Boltzmann temperature distribution thereby restoring the ratio of proton distribution in the antiparallel relative to the parallel states to its equilibrium value.

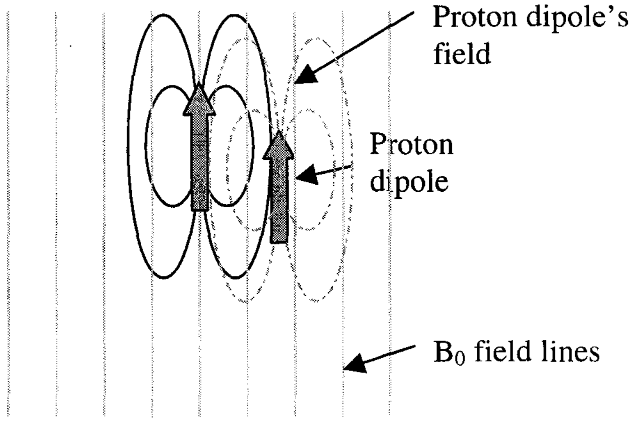

The proton on the right experiences B_0 AND an additional field from the presence of the left proton dipole

Figure 2-4. Microscopic Variation in Magnetic Fields

For simplicity it has thus far been assumed that in magnetic resonance experiments, M_z is tipped only into the transverse plane. This isn't entirely true. Under certain circumstances it is desirable to flip the magnetization beyond the transverse plane onto the negative z-axis. Therefore $M_z = 0$ after a 90 degree pulse, but if $\mathbf{B}_1(t)$ is applied for twice that duration, $M_z = -M_0$ (known as a 180° or inversion pulse).

The recovery of the signal in either case, by longitudinal relaxation, may be approximated by the first order rate equation

$$dM_z(t)/dt = k[M_0 - M_z(t)] \qquad (7)$$

where k is a constant = $-1/T_1$ (T_1 is the longitudinal relaxation time).

which yields solutions of

$M_z(t) = M_0(1-\exp(-t/T_1))$ if $M_z(t=0) = 0$ (i.e. a 90 degree pulse) (8)
$M_z(t) = M_0(1-2\exp(-t/T_1))$ if $M_z(t=0) = -M_0$. (i.e. an inversion pulse) (9)

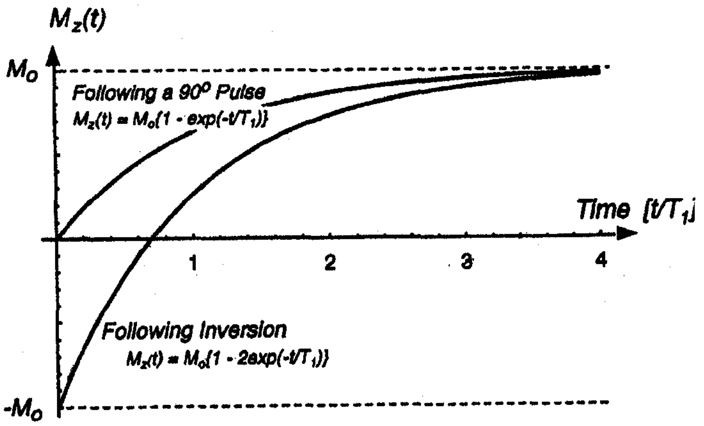

Figure 2-5. T_1 relaxation (longitudinal magnetization recovery) following a 90° and a 180° inversion pulse (Allen 1992).

T_1, the longitudinal relaxation time constant describes the time required to restore the longitudinal magnetization by a factor of e. That is, T_1 governs the rate of z-axis recovery.

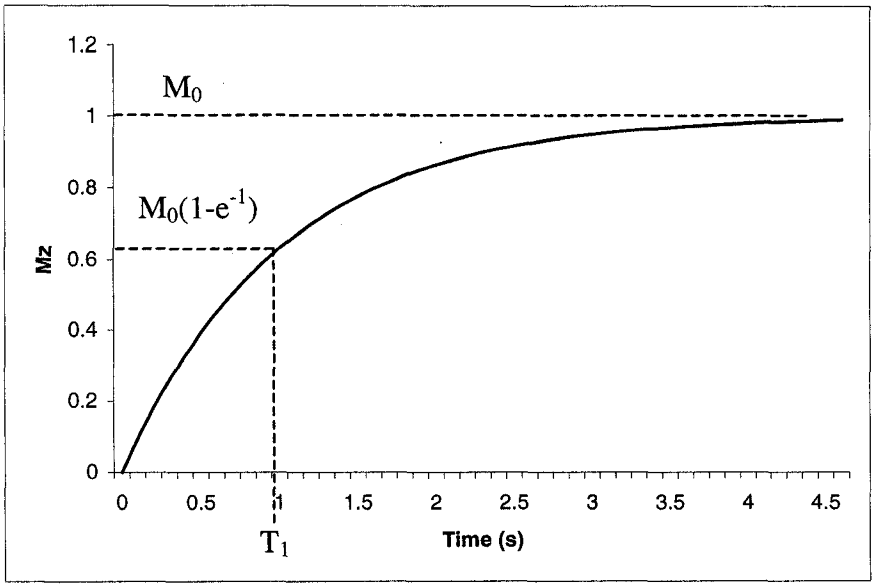

Figure 2-6. Illustration of the meaning of T_1 – a relaxation time constant describing the time required to restore the longitudinal magnetization by a factor of e. Note that here M_0 was set to 1 and the recovery follows a 90° pulse (see Eqn 8 and Figure 2-5).

Different tissues have different T_1 values. If this property is exploited, it provides a means of creating contrast in images. For example consider Figure 2-7. If two separate tissues (with different T_1's) are inverted, both recover at their respective T_1 rates. If, at the moment that one of their longitudinal magnetizations passes through zero, one was to apply a 90-degree pulse to the system (e.g. at time = 1 in the diagram) then only one tissue (short T_1) would produce any signal at all!

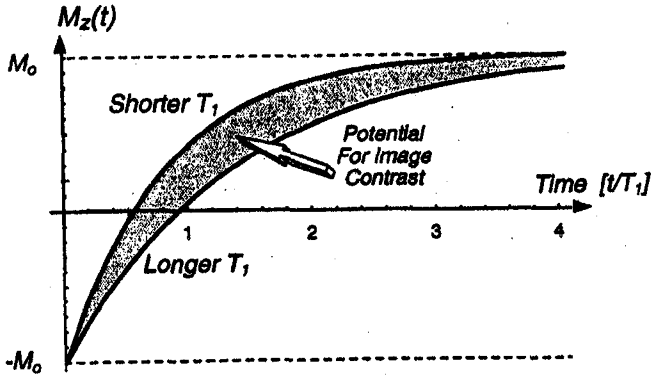

Figure 2-7. Example of longitudinal magnetization recovery of two tissues with different T_1 values following a 180° pulse (Allen 1992).

2.3.2 T_2 Relaxation

T_2 relaxation, also known as spin-spin or transverse relaxation, arises from local magnetic field disturbances. These non-uniformities can be classified as either static or time-dependent, which in turn makes their effects either reversible or irreversible respectively.

2.3.2.1 Irreversible Effects

Irreversible effects arise whenever magnetic dipoles experience time-dependent local magnetic field variations. The one underlying cause in common between T_1 and T_2 relaxation is dipole-dipole interactions. In this case field variations at the Larmor frequency influence the transverse magnetization. However, dipole-dipole interactions have an additional effect specific to T_2 relaxation. This process, which encompasses all of the remaining T_2 effects, is a loss in phase coherence.

A local time-dependent magnetic field disturbance **b**(x,y,z,t) adds to the existing static field (**B_0**) causing a proton to precess at the frequency

$$\omega = \gamma(B_0 + b(x,y,z,t)) = \omega_0 + \Omega(x,y,z,t), \qquad (10)$$

where $\Omega(x,y,z,t)$ is the angular frequency component corresponding to **b**(x,y,z,t).

Within a collection of neighbouring protons, since each perceives a slightly different magnetic field (governed by its position, motion, specific environment, etc.) each also precesses at a slightly different frequency. Because phase $\theta = \omega t$, over the time course of the experiment (i.e. from **B_1** application to data acquisition) neighbouring dipoles with different precessional frequencies, will accrue different phases (a process known as dephasing). Dephasing or loss of coherence leads to minimization of the net magnetization **M** (figure 2-9) with time. Thus the microscopic dephasing leads to irreversible signal decay, known as intrinsic transverse relaxation (denoted by T_2).

Time-dependent magnetic variations may additionally arise when proton-based water molecules diffuse from one region to an adjacent one of a different magnetic field strength within the timeframe of the standard signal decay (~100ms). Note that in this case the regional inhomogeneity itself is static - the time dependence of the fluctuations arises from the movement of the water molecules.

While inhomogeneity of the **B_0** field itself does create such pockets of non-uniformity, the spatial scale is generally so large that a proton will not cross such regions in the allotted timeframe. However, magnetic susceptibility differences between molecules are small enough in spatial scale to contribute to dephasing. Two such examples are iron accumulation in the Parkinsonian basal ganglia and deoxygenated hemoglobin in functional MRI studies (to be discussed later). In the former the magnetic disturbances are ~μm long and therefore easily traversed in ~10ms.

2.3.2.2 Reversible Dephasing

Reversible dephasing occurs when a proton remains within a single static area of non-uniformity. Examples of extraneous static fields are those caused by magnetic field gradients, differences in magnetic susceptibility at non-homogeneous tissue interfaces (e.g. bone-air), and inherent magnetic field imperfections (ΔB_0). In each of these the spatial variation is relatively extensive; despite a proton's movements, it sees a constant field.

In this case

$$\omega = \gamma(B_0 + \beta(x,y,z)) = \omega_0 + \Phi(x,y,z) \qquad (11)$$

where $\Phi(x,y,z) = \gamma\beta(x,y,z)$.

This decay is called T_2'. It results in signal loss if a volume element contains protons that accrue different phases in accord with the unique field experienced by each.

The effective transverse relaxation constant is T_2*, given by

$$1/T_2^* = 1/T_2 + 1/T_2'. \qquad (12)$$

A first order approximation for modeling this decay is

$$dM_{xy}(t)/dt = k'[-M_{xy}(t)] \qquad (13)$$

where $k' = -1/T_2$ (T_2 is the transverse relaxation time),

which has a solution

$$M_{xy}(t) = M_{xy}(0)\exp(-t/T_2). \qquad (14)$$

The T_2 constant is the time it takes for the transverse magnetization to decay by a factor of e. T_2 is always less than or equal to T_1 and both processes occur simultaneously.

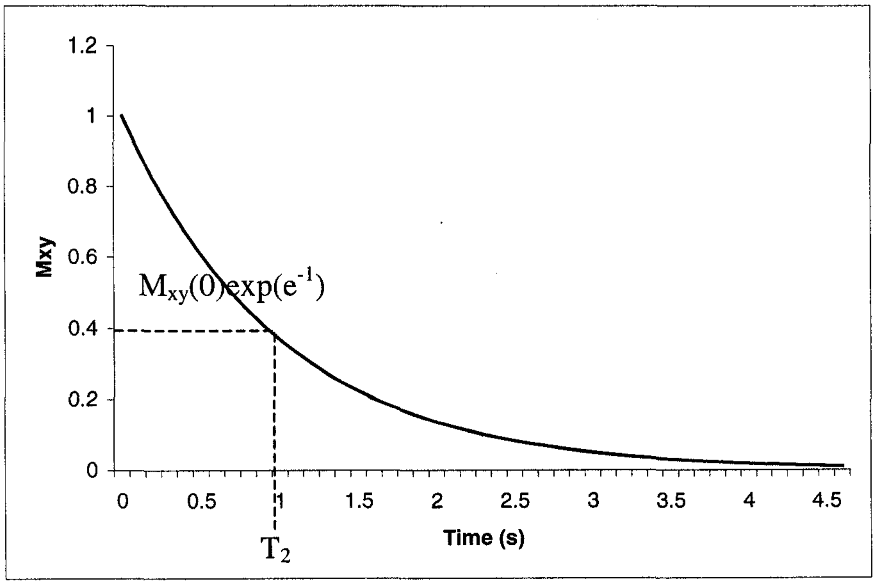

Figure 2-8. Pictorial definition of the T_2 transverse relaxation time constant (here Mxy(0) = 1).

As the name suggests, reversible dephasing can be undone – specifically through the application of a refocusing (180°) pulse along the appropriate axis.

Figure 2-9a. Dephasing Summary

Ideal Case (no Inhomogeneities hence no dephasing)

Suppose the sample consists of 4 protons, whose dipoles are aligned with $\mathbf{B_0}$.

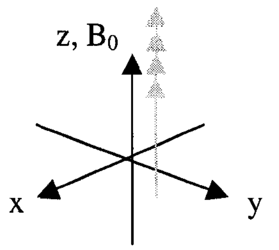

After application of $\mathbf{B_1}$ they are tipped into the transverse plane and all rotate at $\omega_0 = \gamma B_0$.

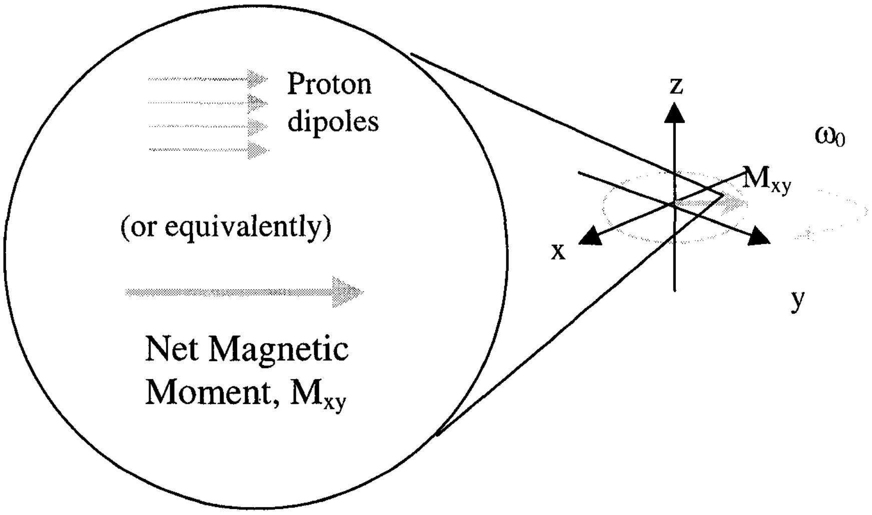

Over time t, all protons acquire the same phase.

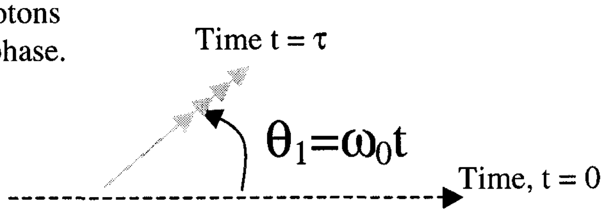

Recorded Induced EMF

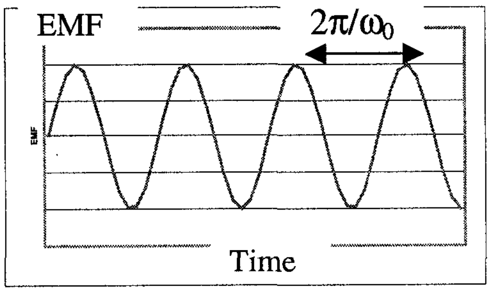

Figure 2-9b. Dephasing Summary

Realistic Case (Microscopic Inhomogeneities exist ⇒ dephasing)

Again the sample consists of 4 protons, whose dipoles all line up with B_0.

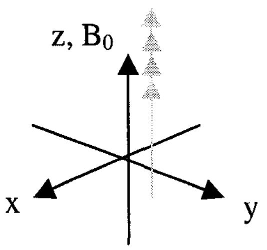

B1 tips the spins into the transverse plane. Non-uniformities exist therefore each proton encounters a slightly different field. If B varies, $\omega = \gamma B$ varies. Thus each proton rotates at a different precessional frequency.

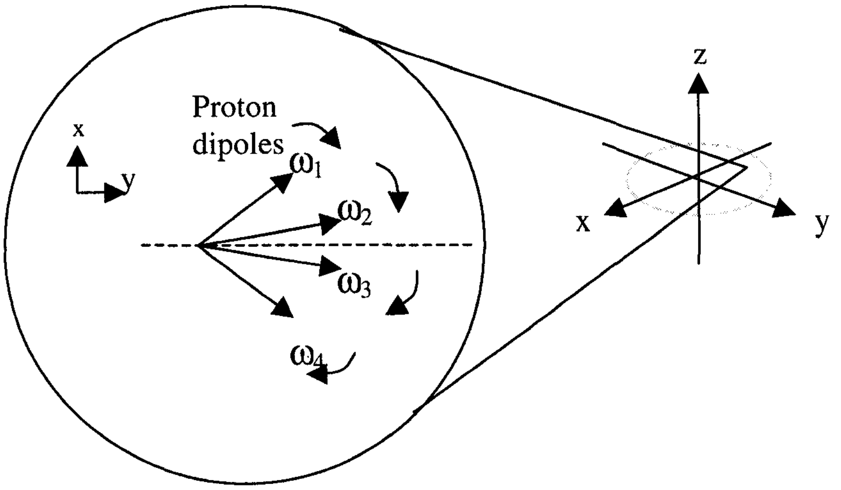

B variation, by $\theta = \omega t = \gamma B t \Rightarrow$ signal loss. As time progresses, the phase dispersion increases leading to a smaller net magnetic moment or signal decay

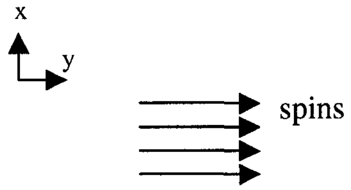

Initially, at time = 0

Time = t

$\theta_1 = \omega_1 t = \gamma[B_0 + b_1(x,y,z,t) + \beta_1(x,y,z)]t$

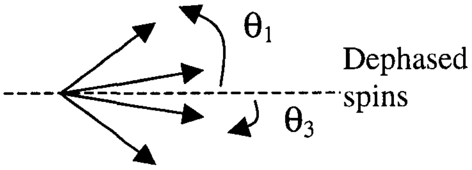

$\theta_3 = \omega_3 t = \gamma[B_0 + b_3(x,y,z,t) + \beta_3(x,y,z)]t$

Net Magnetic Moment

Net Magnetic Moment
(now smaller)

Table 2-2. Tissue T_1 and T_2 values at 1.5T (Stark 1988; Wood 1992)

Tissue	T_1 (ms)	T_2 (ms)
Skeletal Muscle	870	47
Liver	490	43
Spleen	780	62
Fat	260	84
Grey Matter	920	101
White Matter	790	92
CSF	>4000	>2000

2.4 FIDs and Refocused Echoes

Once the magnetization has been nutated into the transverse plane, an EMF is observable in the reception coil. This magnetization immediately begins both longitudinal recovery and transverse decay through both irreversible and reversible mechanisms. The experimenter now has a choice concerning signal loss due to T_2' dephasing – either to accept it or to counteract it.

When no attempt is made to counteract reversible decay, the measured signal suffers from both T_2 and T_2' effects (collectively known as T_2^* effects) and is called the Free Induction Decay or FID. While this may sound like a disadvantage, T_2^* contrast is particularly well suited to certain imaging applications. For example, functional MRI (fMRI) most often uses this contrast. The alternative, T_2 contrast, indeed suffers from less dephasing and signal loss; however, in fMRI this also means less signal difference between resting and active states and hence a weaker differential activation signal.

There are three methods that neutralize signal loss due to T_2' dephasing. Spin echo uses a 180° refocusing pulse to flip the spins 180° about the x or y axis, while gradient recalled echo employs a gradient to reverse the identity of the spins. The common thread uniting these approaches is that each recovers the signal by producing an echo.

2.4.1 Echo Production

To simplify visualization, the frame of reference can be defined such that the entire axis now rotates about the z-axis at ω_0 (figure 2-10). The axes' directions are labelled with the subscript ρ.

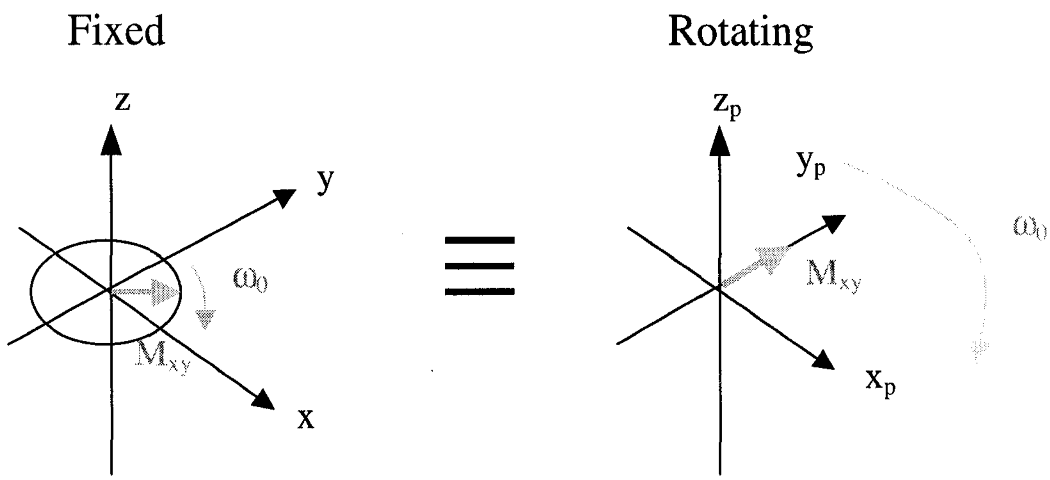

Figure 2-10. Depiction of the fixed and rotating frames of reference. In the fixed frame, only the transverse magnetization rotates at ω_0 while in the rotating frame both the magnetization and the axis rotate at ω_0.

Consider an isochromat or small bundle of magnetic moments. As depicted in figure 2-9b, following nutation into the transverse plane, local inhomogeneities lead to a spectrum of precession frequencies within that isochromat. Some spins experience a field greater than B_0 and precess more quickly than the rotating frame (fast spins), while others experience a field smaller than B_0 and accordingly precess more slowly than the rotating frame (slow spins). In this rotating axis, these latter spins appear to rotate in the opposite direction (figure 2-11).

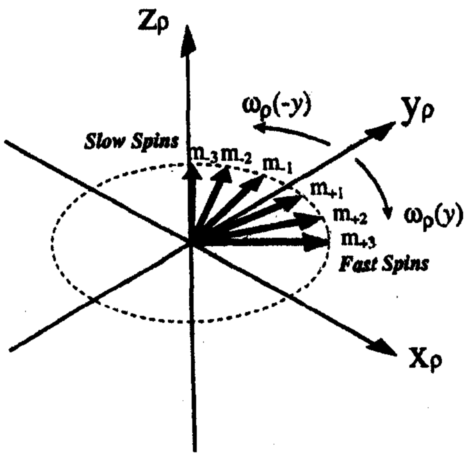

At t = After Pulse

*Figure 2-11. Illustration of fast and slow spins in the rotating frame of reference. Fast spins see a greater field than **B_0**, thus rotate more quickly than the frame of reference, while slow spins experience a net field less than **B_0** and therefore rotate more slowly than the reference frame (Allen BME 564 course notes).*

Suppose that a $180°_x$ (**B_1**) pulse is applied τ seconds after excitation. The cross product in the equation of motion, Eqn (6), ensures that the x_ρ components of the spins are unaffected; however, the y_ρ components rotate about the x_ρ-axis exactly as before during excitation (i.e. same sense and $\omega_1 = \gamma B_1$ frequency as before). Notice that as a result, the fast spins still precess more quickly than the reference frame, but now towards the $-y_\rho$ axis. Similarly the slow spins also converge towards $-y_\rho$. After an interval of τ seconds following the $180°_x$ pulse, the spins converge upon the $-y_\rho$-axis, or refocus, recreating the original signal amplitude but now along the $-y_\rho$-axis (figure 2-12). This is called a "spin echo".

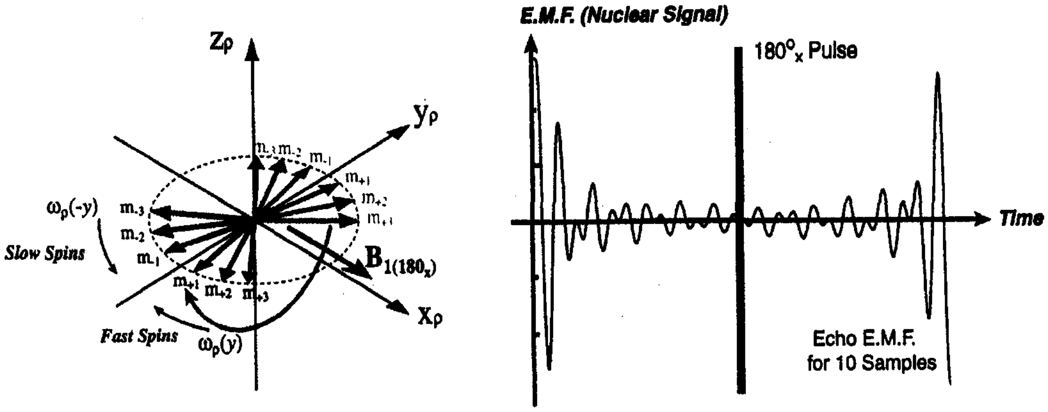

Figure 2-12. Refocusing following a $180°_x$ (B_1) pulse with the individual spins shown on the left and the recorded EMF on the right (Allen BME 564 course notes).

A $180°_y$ (B_1) pulse acts comparably, instead creating a flip about the y_ρ-axis such that the fast and slow spins refocus at the $+y_\rho$-axis (figure 2-13).

An important point to note, is that even though refocusing pulses generate echoes by refocusing reversible decay effects, they are unable to prevent the continuous decay according to irreversible mechanisms (figure 2-14)

The final refocusing approach is called gradient echo. This method is only applicable if the nature of the magnetic distortion is well understood. As an example, suppose that a linear magnetic field gradient is applied to the system. This artificially creates a spectrum of precession frequencies and is used to encode spatial information (discussed later). Exactly as above, this leads to signal dephasing in the rotating frame. By reversing the polarity of this gradient, the identity of the spins is reversed such that spins that had precessed at $\omega=\gamma(B_0 + G_r \bullet r)$, where G is the gradient amplitude and r the spatial position of the spins, now precess at $\omega=\gamma(B_0 - G_r \bullet r)$. This effectively undoes the gradient-induced dispersion and the spins refocus on the $+y_\rho$-axis (figure 2-13).

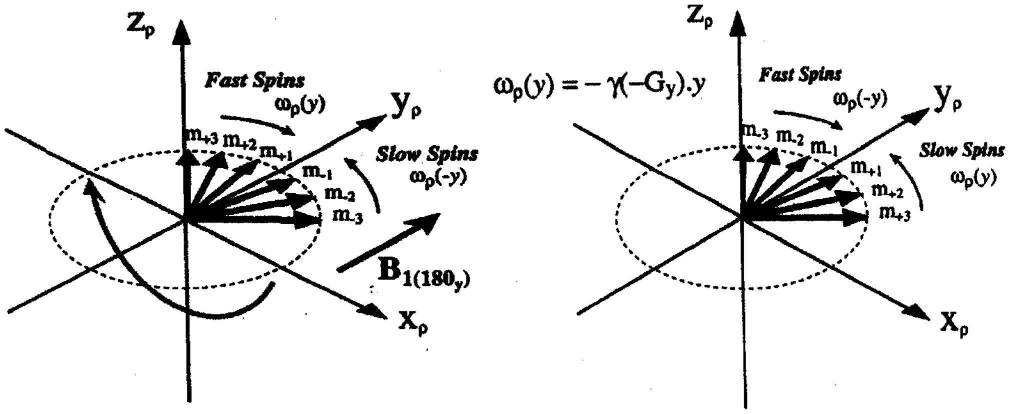

Figure 2-13. Refocusing following a 180$^\circ_y$ (B_1) pulse (left) and following a gradient polarity reversal (right) (Allen BME 564 course notes).

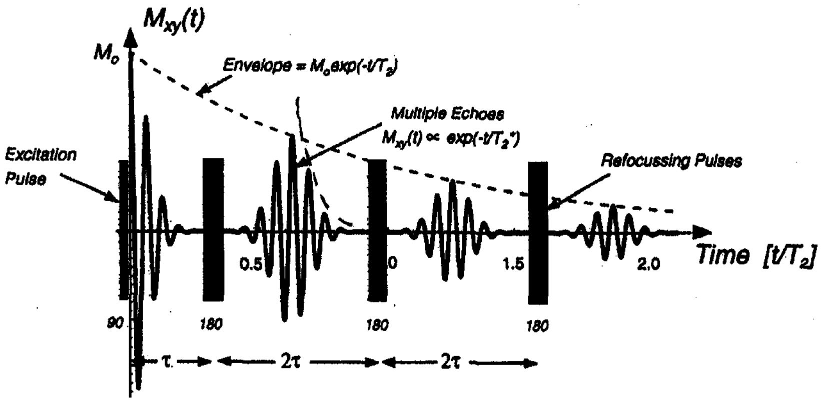

Figure 2-14. Illustration of a pulse sequence in which several refocusing pulses are used to generate several echoes. Although the T_2' inhomogeneity is refocused as is evident by the recovery of an echo following a 180 pulse, note that the ever-present irreversible decay mechanisms still cause the envelope of this signal to decay according to T_2 (Allen 1992)

Gradient echo and Spin echo refocusing techniques are the basis for Gradient echo (GE) and Spin Echo (SE) imaging. The former uses refocusing only to undo the effects of the applied spatial encoding gradient. This is because gradient echo formation requires precise knowledge about the inhomogeneity causing the distortion – something that is typically unknown. Thus GE images have a T_2* contrast (do not refocus T_2' effects) while the SE, which can refocus any reversible inhomogeneity without understanding its exact nature, yields images with T_2 contrast.

2.5 Imaging

The NMR experiment discussed to this point, is incapable of creating images. According to the previous material, all of the spins in a sample are excited and precess at $\omega = \gamma B_0$ in the absence of inhomogeneities. Critical to the imaging application are slice selection and spatial encoding of information – both of which use magnetic field gradients.

In order to create an image, there must be some means by which the recorded signal can be disentangled to yield spatial information.

2.5.1 Spatial Encoding

2.5.1.1. Frequency Encoding

NMR encodes spatial location information into the precession frequency through the application of linear magnetic field gradients. A linear magnetic field gradient is a field aligned with B_0, but whose amplitude varies linearly with position (figure 2-15). Thus the net field, frequency and phase all depend on position.

$$\mathbf{B} = \mathbf{B_0} + \mathbf{G_r} \bullet \mathbf{r} \qquad (15)$$

$$\omega = \gamma(B_0 + G_r \bullet r) \qquad (16)$$

$$\theta = \gamma(B_0 + G_r \bullet r)t \qquad (17)$$

where $\mathbf{G_r}$ = the amplitude of the linear gradient (varying in the r direction)
$\mathbf{r}$ = the position of a hypothetical spin
t = the duration of gradient application.

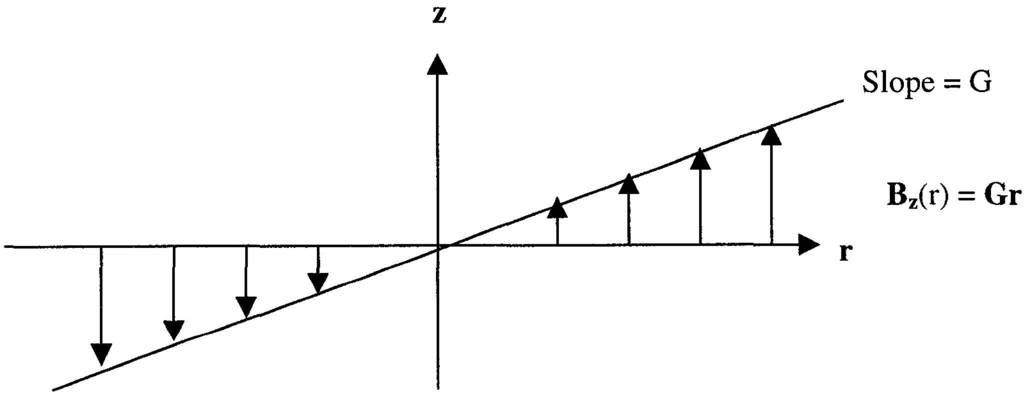

Figure 2-15. A linear magnetic field gradient along the r-direction.

The creation of a 2-D image necessitates spatial encoding in 2 orthogonal directions. Two-fold frequency encoding by simultaneous application of two orthogonal gradients seems an obvious approach. Unfortunately, this only results in 1-D encoding along the direction given by the vectorial sum of two gradients – for example along an x-y diagonal line. An alternate method is therefore required.

2.5.1.2 Phase Encoding

In NMR the most common tactic for producing a 2-D image is to combine frequency encoding in one direction, with phase encoding along a second, orthogonal direction. If a gradient is applied for time τ, the spins dephase according to the equation

$$\varphi(r) = \omega(r)\,\tau = \gamma G r \tau. \tag{18}$$

Thus by applying a gradient pulse, phase information is encoded into the spins that is a function of the spatial location.

Suppose that following excitation, one first applies a phase encoding (y) gradient and then acquires the data while administering an orthogonal frequency encoding (x) gradient. The sampled time-series data points are frequency encoded along the entire x-direction (because spins precess at a frequency proportional to their x position) and all have been given the same phase offset via phase encoding. In order to complete the phase encoding along the entire y-direction, this same sequence must be repeated many times, each with a different phase (figure 2-16).

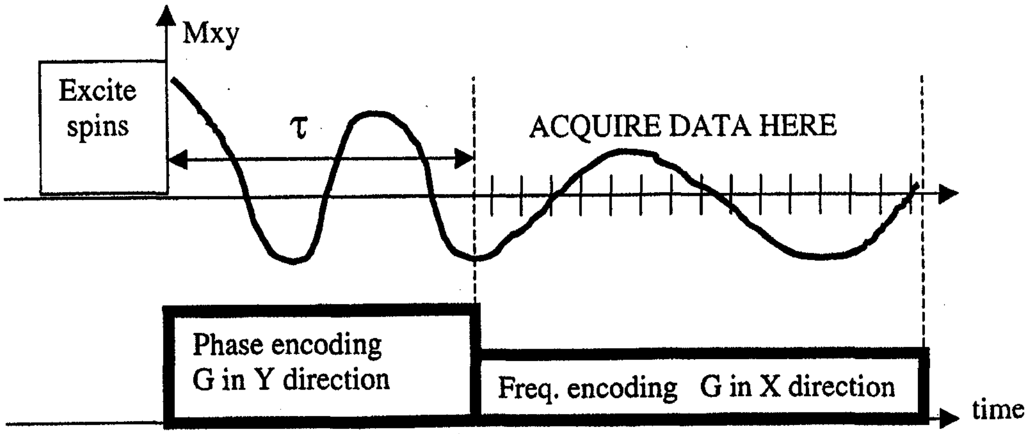

Figure 2-16. The basic NMR imaging experiment. Note that the above sequence is repeated many times, each time with a different value of G_y *in order to fully spatially encode the data (Wilman BME 564 course notes).*

Frequency and phase encoding are conceptually quite similar. In frequency encoding, data are sampled during the application of the frequency encoding gradient. Thus each subsequent point in time accrues an additional phase offset given by

$$\Delta\varphi(x) = \omega(x)\,\Delta t = \gamma G x \Delta t \qquad (19)$$

that is also a function of the x-position. In other words, during acquisition t is constantly advancing from one data point to the next. This yields, for example, 128 samples with increasing phase angle at each later point and in addition the phase at each specific instant in time is a function of x-position (common resolution in fMRI is 128*128, i.e. each image is composed of 128 pixels in the x direction and 128 in the y direction).

In phase encoding, the gradient is applied for a constant time. In order to add a different phase to the spins with each run of the above experiment the gradient amplitude is changed. Thus

$$\Delta\varphi(y) = \Delta\omega(y)\tau = \gamma\Delta G y \tau. \qquad (20)$$

In the rotating frame, frequency encoding separates the spins such that those experiencing the most positive gradient amplitude spin the most quickly, while those with the most negative amplitude precess the most slowly. This difference in precession rates (translatable to phase by $\varphi = \omega t$) allows for frequency encoding. Phase encoding begins in an identical manner: a similar gradient is applied that temporarily causes this same spread in precessional frequencies (and phases over time t). The difference is that it is then shut off. As a result the spins all revert to a common precessional frequency, but now each has a unique phase.

Having applied a gradient, the magnetization content at each frequency or position can be recovered by Fourier transform analysis of the recorded time-domain signal.
Spatial encoding involves both frequency and phase encoding or the application of both an x and a y-gradient (G_x, G_y) to a system of spins. The reception coil encompasses the entire sample, thus the detected signal, S(t), is given by integrating the magnetization M_{xy} over the range of x and y positions.

$$S(t) = \exp(-i\gamma B_0 t)\int\int M_{xy}(x,y)\exp(-i\gamma G_x x t)\exp(-i\gamma G_y y t)\,dx\,dy \qquad (21)$$

which in the rotating frame is

$$S(t) = \int\int M_{xy}(x,y)\exp(-i\gamma G_x x t)\exp(-i\gamma G_y y t)\,dx\,dy. \qquad (22)$$

Remember that the Fourier Transform itself is defined as

$$F(\omega) = \int_{-\infty}^{\infty} f(t)e^{-i\omega t}dt. \qquad (23)$$

Thus simple substitution of $\omega = \gamma Gt$, and extension into two dimensions shows Eqn (22) to be a 2D Fourier Transform. However, rather than use ω which already has other meaning, magnetic resonance convention is to define

$$k = \begin{array}{ll} \gamma Gt & \text{(for a rectangular gradient) or} \\ \gamma\int G(t)dt & \text{(for an arbitrarily shaped gradient).} \end{array} \qquad (24)$$

As a result NMR Fourier space is instead called k-space.
Thus

$$k_x = \gamma G_x t \qquad (25)$$

$$k_y = \gamma G_y t \qquad (26)$$

and from Eqns (22), (25), (26)

$$\begin{aligned} S(k_x, k_y) &= \int\int M_{xy}(x,y) \exp(-ik_x x)\exp(-ik_y y)dxdy \qquad (27) \\ &= FT\{Mxy(x,y)\}. \end{aligned}$$

Therefore, the IFT of the detected signal recovers the spatial distribution of the transverse magnetization, i.e. the magnetization content at each x-y location.

$$M_{xy}(x,y) = IFT\{S(k_x, k_y)\} \qquad (28)$$

For an illustration of the spatial encoding process see Appendix B.

2.5.2 K-Space

K-space provides an alternate way of viewing an MRI experiment. In particular, it elucidates the different ways in which pulse sequences sample data.

Eqns (25), (26) for rectangular gradients may be extended to arbitrarily shaped gradients as

$$k_x = \gamma\int G_x dt \qquad (29)$$

$$k_y = \gamma\int G_y dt. \qquad (30)$$

Furthermore, Eqn (27) shows the Fourier transform equation relating not frequency and time, but spatial position and k-space. Thus k-space is like frequency space, but more accurately is a "net gradient area space". The distance separating adjacent sampled data points in the phase and frequency directions is given as

$$\Delta k_{phase} = \gamma \Delta G \tau \qquad (31)$$

$$\Delta k_{frequency} = \gamma G \Delta t\,. \qquad (32)$$

The process of capturing all of the data necessary to form an image can be visualized in k-space - it is equivalent to covering all of k-space line by line. MRI sequences cover this area in different ways.

Two of the most common imaging sequences, spin echo and gradient echo, both acquire one k_x line with each r.f. pulse (figure 2-17). Single-shot echo planar imaging (EPI), on the other hand, covers the entire k-space, line after line, after only one r.f. pulse (figure 2-18). Finally many k-space sampling trajectories exist including top down, bottom up, centre out and spiral techniques.

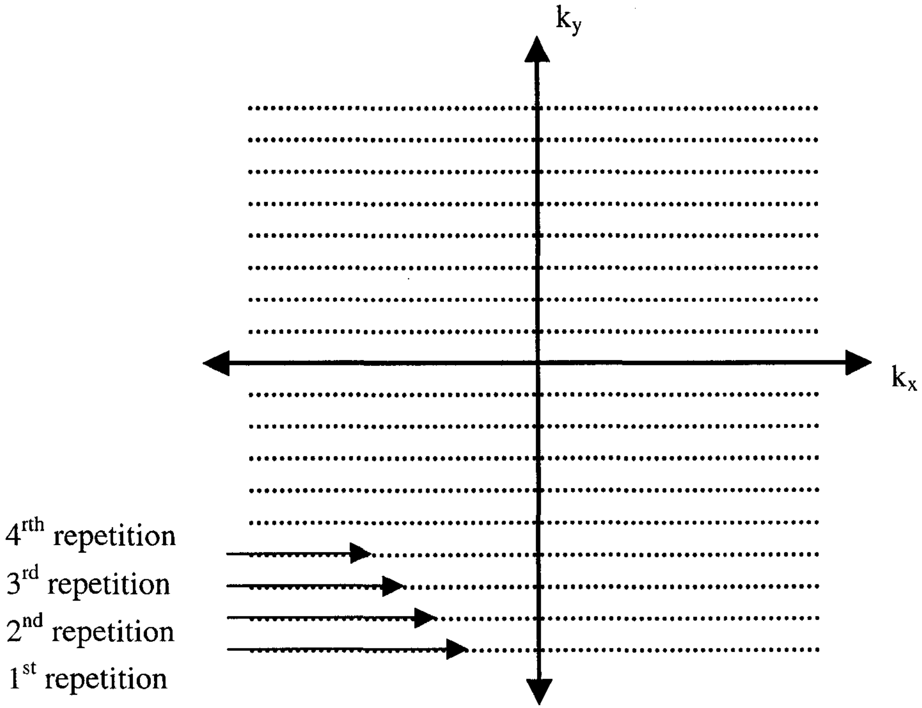

Figure 2-17. Bottom up k-space trajectory used by sequences such as gradient echo or spin echo imaging.

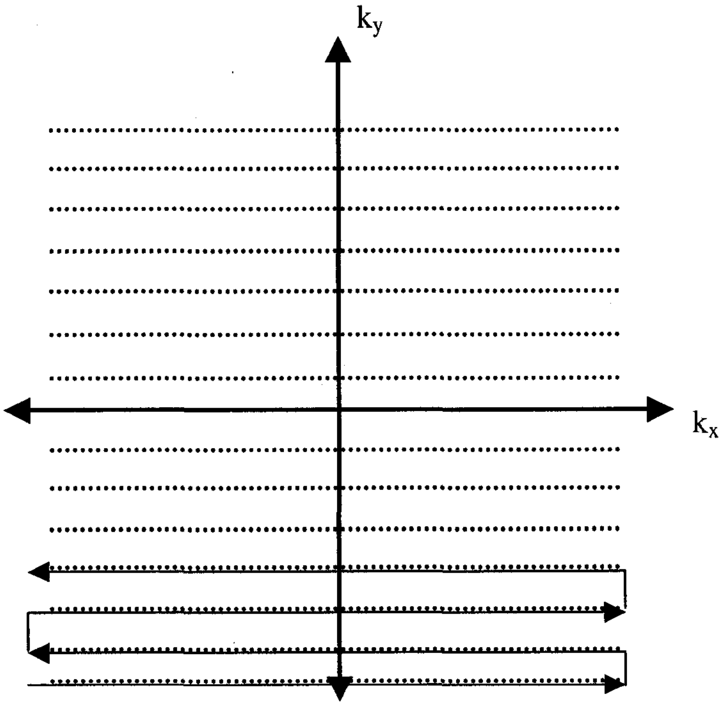

Figure 2-18. K-space trajectory for bottom up single shot echo planar imaging.

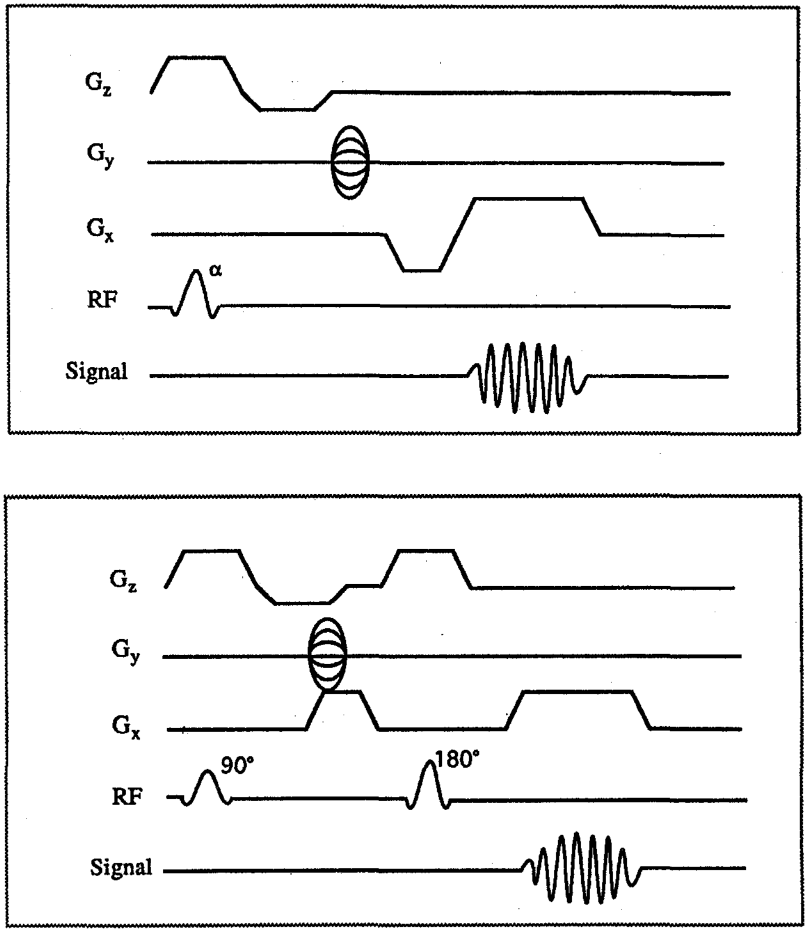

Figure 2-19. Timing diagrams for gradient echo (top) and spin echo (bottom) sequences.

2.5.3 Spatially Selective Excitation (slice selection)

Spatially selective excitation excites spins only in a specific slice, leaving the others unaffected and pointing in the longitudinal direction. It involves the interaction of a slice selective gradient and a spatially selective pulse. In particular, during rf excitation, a gradient is applied perpendicular to the imaging plane in order to differentiate spins in the slice selective (e.g. z) direction. Having created the spectrum of precessional frequencies along the z-direction, a segment of these spins can be preferentially excited by modulating the B_1 r.f. carrier envelope such that the r.f. pulse's excitation bandwidth is matched to their occupied frequency band (figure 2-20).

Suppose that the slice of interest is centred at $z = z_0$ and its thickness is Δz. By applying a z-gradient the precessional frequency bandwidth of the slice is

$$\begin{aligned}\Delta\omega &= \omega_{top} - \omega_{bottom} = \gamma[B_0 + G_z(z_0 + \Delta z/2)] - \gamma[B_0 + G_z(z_0 - \Delta z/2)] \qquad (33)\\ &= BW_{rf}.\end{aligned}$$

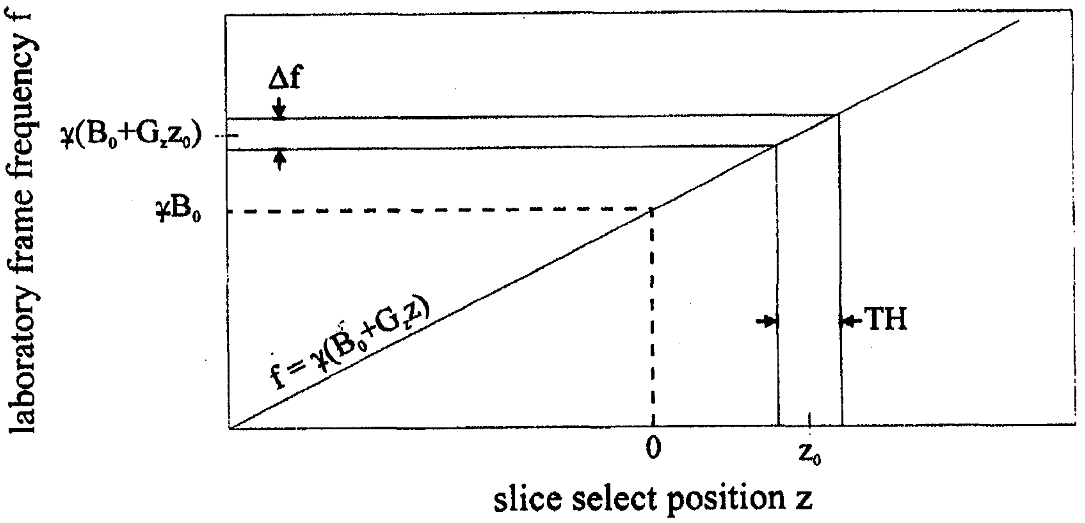

Figure 2-20. In order to selectively excite spins within a slice having thickness = TH and being centred at $z = z_0$, *the rf pulse must have a bandwidth* $BW_{rf} = \gamma G_z\Delta z$ *and a centre frequency shifted from the Larmor frequency* (ω_0) *by* $\gamma G_z z_0$ *(Haacke 1999).*

There is an approximate relationship between the slice profile and the excitation pulse ($B_1(t)$) envelope. Known as the "small tip angle approximation", for flip angles $\leq \pi/2$ the slice excitation profile is the Fourier transform of the r.f. envelope. Uniform selective excitation across a rectangular slice (or a rectangular block of precessional frequencies) requires a boxcar frequency excitation profile which under the small tip angle approximation, is a sinc shaped r.f. envelope in the time domain.

2.5.3.1 Rephasing

The application of a slice select (SS) gradient is essential for achieving slice selectivity during excitation. The underlying mechanism, the spreading out of precession frequencies, also causes a dephasing-related signal loss as encountered earlier with transverse gradients. This time the dephasing occurs in the slice select direction, beginning at the moment of r.f. pulse application. In order to approximate a compensatory mechanism to the dephasing, consider the simplified notion that at t = 0 (corresponding to the centre of the r.f. pulse in the SS gradient) the spins in a slice are instantaneously excited. At height z within the slice, the now transverse magnetization slice acquires a phase according to

$$\varphi(z,t) = -\gamma G_{ss}zt \qquad \text{(in the rotating frame).} \qquad (34)$$

Imagine that this slice is a collection of infinitesimal subslices each at a slightly different z position. By Eqn (34), this leads to dephasing within the slice and ultimately signal loss. As before the solution is to reverse the gradient. The application of the opposite polarity gradient field reverses the accrual such that all of the excited spins have zero initial phase (figure 2-21). In keeping with the above scenario, dephasing begins at instantaneous excitation (t=0) and ends with the cessation of the SS gradient (i.e., half of the total SS gradient). The total phase acquired

$$\varphi = -\gamma z \int_0^T G_{ss} dt \qquad (35)$$

is proportional to $\int^T_0 G_{ss} dt$, the area under the gradient. Reversal of phase effects is governed by the following equation

$$\left| \int G_{ss} dt \right| / \left| \int G_{refocus} dt \right| = 0.5. \qquad (36)$$

That is, for the refocusing gradient a negative polarity and any combination of gradient amplitude and duration in accord with Eqn (36) will suffice.

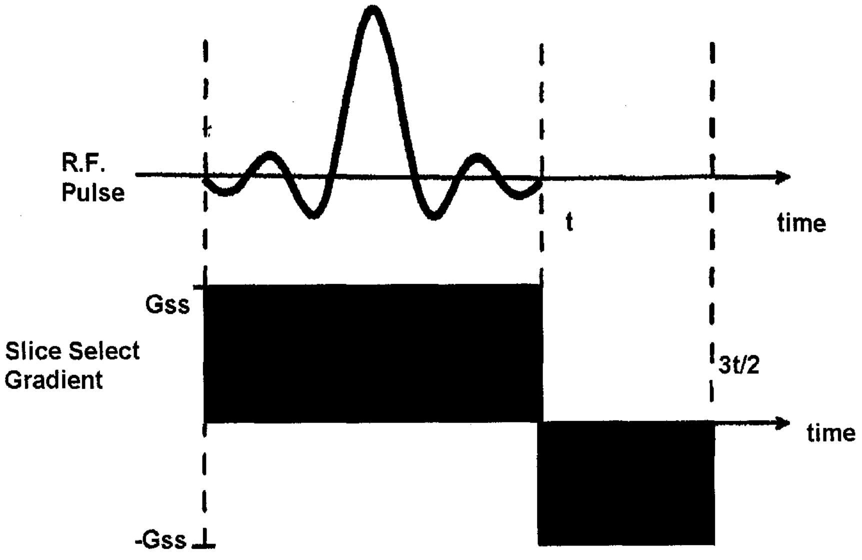

Figure 2-21. Illustration of the slice select gradient with refocusing lobe.

2.6 Conclusion

This chapter has discussed the basic components of an imaging experiment including preparation, excitation, acquisition, contrast mechanisms, spatial encoding and slice selection. With this background, the reader is now prepared for subsequent chapters which build on this knowledge, including Chapter 3 which explains the BOLD contrast mechanism that is based on T_2* relaxation, and Chapter 8 which describes echo-planar imaging.

2.7 References

Allen, P.S. Some Fundamental Principles of Nuclear Magnetic Resonance. The Physics of MRI 1992 AAPM Summer School Proceedings, American Institute of Physics, Inc, Woodbury, NY, 1993.

Haacke, E.M., Brown, R.W., Thompson, M.R., Venkatesan, R. Chapter 10 Magnetic Resonance Imaging – Physical Principles and Sequence Design, John Wiley and Sons Inc. New York, NY, 1999.

Hornak, J.P. The Basics of MRI (software file) Copyright © 1996-2000

Stark, D. D., MR Imaging of Focal Liver Masses. Radiology, 168: 323-326 (1998)

Wood, M. and Bronskill, MR Desktop Data. J Magn Reson Imag 2 (S):13 (1992)

Chapter 3

The BOLD Mechanism

3.1 Introduction

This chapter focuses on blood oxygenation level dependent or BOLD functional imaging. It begins with a simplified overview of the physiological response following neuronal activation that gives rise to the BOLD signal. Next, magnetic susceptibility is defined. This property is the basis of functional contrast on BOLD images. The chapter then proceeds to expand upon the BOLD mechanism, dividing it spatially into three different levels of effects: microscopic intravascular, or T_2 blood changes, macroscopic intravascular, or T_2' effects, and extravascular effects. Since one focus of this thesis is functional imaging at 4.7T, the chapter concludes by examining the influence of field strength on the BOLD signal.

3.2 Overview

Blood oxygenation level dependent (BOLD) functional magnetic resonance imaging records a physiological response in order to characterize a neuronal response. As opposed to directly recording neuronal firing within the brain, BOLD fMRI measures the local metabolic and hemodynamic changes associated with the local neuronal firing[1].

Blood oxygenation level dependent functional imaging is a rapidly developing field still in its infancy. The groundwork was laid with the observation that in blood the T_2 relaxation of protons was correlated to the oxygenation level (Thulborn 1982). The importance of this was realized by Ogawa who pioneered the use of BOLD contrast to detect physiological events that alter the oxy/deoxyhemoglobin ratio – although the initial application measured BOLD signal intensity changes induced by anesthetic inhaled gases and insulin-induced hypoglycemia in rats (Ogawa 1990). Similarly, Turner demonstrated that changes in blood oxygenation in cats resulted in susceptibility changes that could be monitored using T_2*-sensitive gradient-echo echo-planar imaging (1991). Accumulating evidence that BOLD could monitor in vivo hemodynamic changes such as CBF and $CMRO_2$, and increased data linking neuronal activity to blood oxygenation, led Ogawa and others to extend this work, using BOLD contrast as an indicator of local neuronal activity within the visual (Ogawa 1992, Kwong 1992) and motor (Bandettini 1992, Kwong 1992) cortices. Current research covers an enormous variety of diseases and conditions, across all regions of the brain.

The BOLD signal is formed primarily by the interaction of two physiological processes: cerebral metabolic rate of oxygen consumption ($CMRO_2$) and cerebral blood flow (CBF) (figure 6-1) (although cerebral blood volume (CBV) is sometimes included as well due to its strong relation to CBF)[2]. In particular, it is the uncoupling of $CMRO_2$ and CBF that yields an observable BOLD signal. This has been demonstrated empirically using visual and somatosensory stimulation wherein $CMRO_2$ changed by 0-5% while CBF changed from 40-51% (Moonen, C.T.W., Bandettini, P.A Functional MRI p.107).

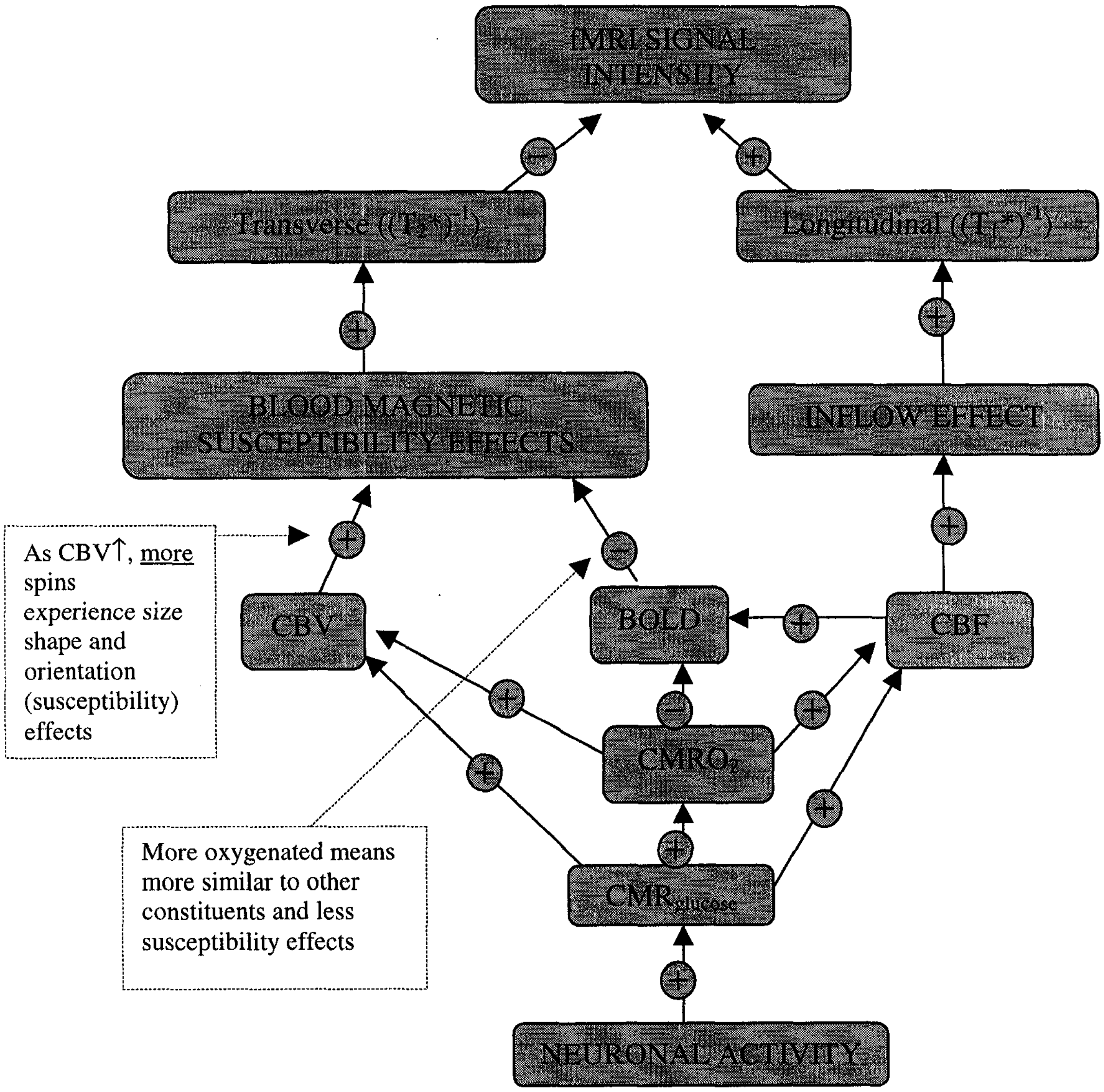

As CBV↑, more spins experience size shape and orientation (susceptibility) effects

More oxygenated means more similar to other constituents and less susceptibility effects

Figure 3-1 The complex inter-relationships between physiological phenomena and the resultant fMRI signal intensity. A (+) indicates proportionality while a (-) is inverse proportionality. Signal intensity changes may be influenced by both of the relaxation rates, or more precisely, by changes to their apparent and not intrinsic values. A given pulse sequence's parameters determines the respective influence of either of these rates. While T_1 is predominantly influenced by inflow effects[3], T_2 is affected by bulk magnetic susceptibility effects. Inflow effects are insignificant if the time between successive samples of the same slice is long enough to allow for full relaxation (i.e. $TR >> T_1 =$ 920ms at 1.5T (grey matter) which is the case in my experiments) (Moonen, C.T.W., Bandettini, P.A. Functional MRI p92).

3.3 Magnetic Susceptibility

Magnetic susceptibility (χ) is a dimensionless parameter which characterizes the degree to which a material alters the strength of a magnetic field applied to it. That is,

$$B_{seen} = (1+\chi)\, B_{applied} \qquad (1)$$

Microscopic magnetic components (dipoles) line up parallel to or antiparallel to B_0 in most materials. If they counteract the field, they are termed diamagnetic (e.g. most proteins, tissue water, oxyhemoglobin), whereas if they add to it they are paramagnetic (e.g. deoxyhemoglobin). Of fundamental importance to BOLD imaging, is the fact that the hemoglobin molecule has opposite magnetic properties depending on its oxygenated status. Oxyhemoglobin is diamagnetic (isomagnetic to the surroundings) while deoxyhemoglobin is paramagnetic[4].

Reiterating section 2.3 (Relaxation), neighbouring dipoles may encounter different magnetic fields due to local field inhomogeneities, leading to both reversible and irreversible signal decay. The presence of deoxyhemoglobin within the blood affects water protons both within the blood vessel and the surrounding tissue by this same mechanism: deoxyhemoglobin creates spatially variable magnetic field distortions such that adjacent protons experience different fields. The effect occurs both microscopically, as each single deoxyhemoglobin molecule creates its own field disturbance affecting neighbouring protons, and macroscopically in that vessels containing many such molecules act as little bar magnets generating a larger scale distortion affecting both intra and extravascular protons.

Oxyhemoglobin, however, doesn't have this effect because its susceptibility is equivalent to that of surrounding tissues and blood constituents. Therefore, it doesn't establish additional field distortions nor lead to subsequent signal decay.

3.4 The BOLD Mechanism

3.4.1 Overview

Functional image contrast (the difference in signal intensity between a pair of images due to different activation states, e.g. active vs. rest) is generated by the magnetic susceptibility differences between deoxygenated hemoglobin and neighbouring tissues/molecules. The stages linking neuronal activity to image intensity changes are as follows:

1) The subject conducts a task that elicits neuronal activation in a localized region of the brain

2) The neuronal activation gives rise to local O_2 consumption and hence an increase in deoxyhemoglobin concentration (because as oxygen is used up, formerly oxygenated hemoglobin becomes deoxygenated)

3) Next, CBF and CBV increase[5] (to compensate for the depletion of oxygen) while $CMRO_2$ remains constant.
    a. This provides a flood of incoming, fresh, oxygenated blood
    b. In turn, this decreases the fraction (or relative concentration) of deoxyhemoglobin (because adding a large amount of oxyhemoglobin reduces the relative concentration of deoxyhemoglobin)
    c. Less deoxyhemoglobin brings about less dephasing and signal decay
    d. Less signal decay leads to brighter signal intensity in areas during activation

Consequently, local neuronal activation will lead to brighter local image intensity compared to when that region is at rest (figure 3-2).

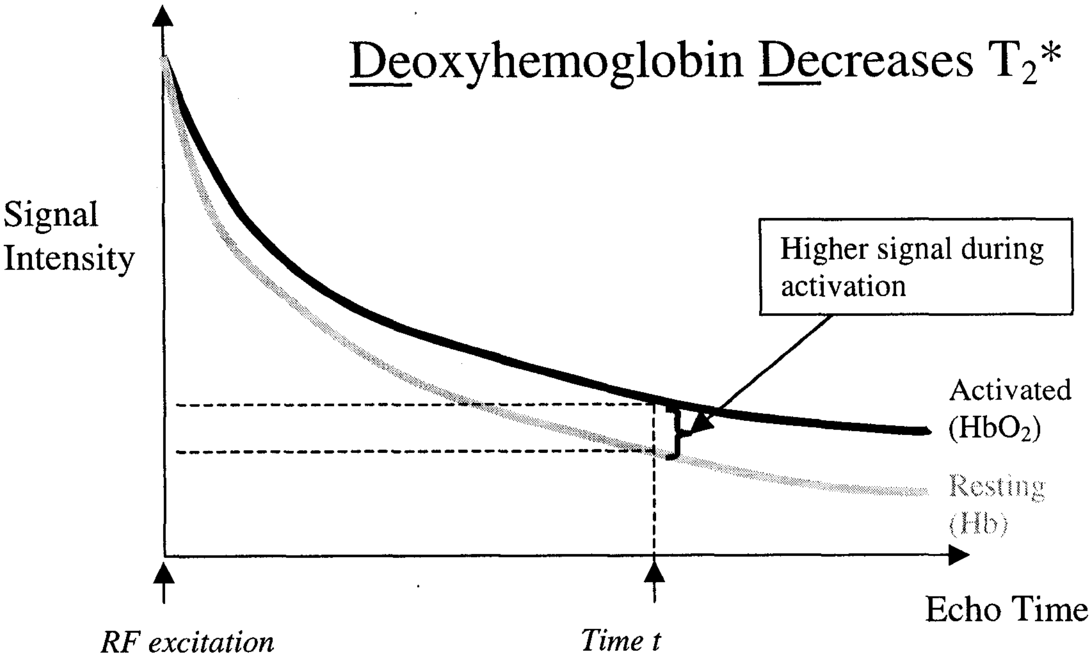

Figure 3-2. Activated versus resting signal time courses for a voxel in the brain. Suppose that two identical experiments were conducted - in each the signal is acquired at exactly the same time instant following r.f. excitation (Time t). In one case the brain voxel is activated, in the other it is resting. The relative decrease in deoxyhemoglobin in the active case results in less dephasing and hence slower signal decay – i.e. a brighter signal.

The BOLD mechanism defined above is typically subdivided spatially into 3 different levels of effects$_6$. This encompasses effects due to T_2 changes as well as both intra and extravascular bulk magnetic susceptibility effects influenced by the size, shape and orientation of a vessel containing many spins.

3.4.2 Blood T_2 Changes

Protons diffuse in random fashion about the blood vessel, experiencing different fields as they go, due to the microscopic disturbances caused by deoxyhemoglobin molecules (figure 3-3). This is an additional T_2 relaxation mechanism specific to BOLD. The dependence of blood T_2 on its oxygenation was first shown by Thulborn et al. (1982).

Quantitatively, in the event of a long TE (>20ms for GE sequences), the change in T_2 may be simplified as follows:

$1/T_2 \approx 1/T_{2\text{-naught}} + K(1-Y)^2$ (2) (Equation follows from empirical data)

where $T_{2\text{-naught}}$ = intrinsic T_2 of blood
K = a constant α B_0^2 and hematocrit$_7$
Y = oxygen saturation of hemoglobin.

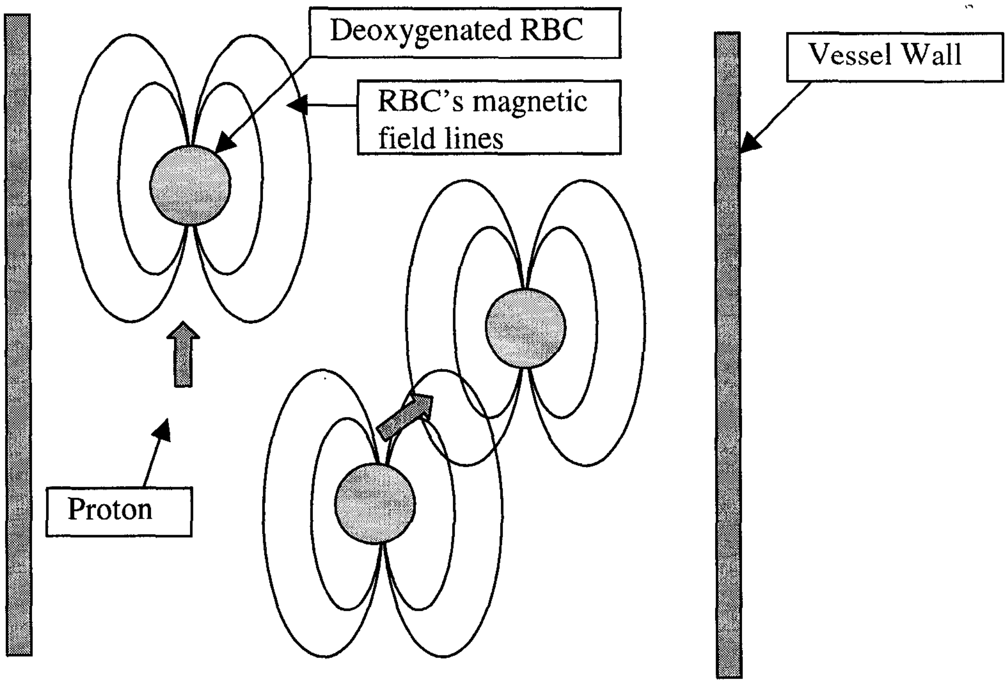

Figure 3-3. T_2 BOLD magnetic susceptibility effects.
*This diagram is a simplified cartoon meant only for didactic purposes. Note that each of the two neighbouring protons (gray arrows), moving and oriented in a random way, experiences a different net magnetic field. In addition to **B_0** (not shown), each proton senses a different susceptibility field - the left proton experiences a much smaller susceptibility field than the right one. Thus, neighbouring protons precess at different frequencies leading to greater-than-intrinsic T_2 relaxation rates.*

3.4.3 Vessel Size, Shape and Orientation Effects (T_2' effects[8])

T_2 changes describe the differences in B_0 homogeneity seen by individual neighbouring protons, i.e. microscopic effects. On a larger spatial scale, the bulk magnetic susceptibility effects of deoxyhemoglobin molecules give rise to a net frequency shift common to <u>all</u> protons in a given vessel segment, i.e. a macroscopic, ensemble effect (figure 3-4). This is analogous to a bar magnet where T_2 effects relate to the spatial scale of magnetic dipoles while T_2' effects are equivalent to the field of the entire bar magnet. The frequency shift of all protons in a vessel segment is described by[9]

$$\Delta f = K'(3\cos^2\theta - 1)(1-Y) \qquad (3)$$

where $K' \alpha B_0$
θ = angle of the vessel segment to B_0
Y = oxygen saturation of hemoglobin.

Capillaries and venules are randomly oriented in the cortex. If a voxel contains several microvessel segments, each at a different orientation, then by Eqn (3) protons within each segment develop a different frequency shift, resulting in intravoxel dephasing (figures 2-9b, 3-5). Similarly intravoxel dephasing occurs if part of a vessel is included with extravascular tissue in the same voxel (known as a partial volume effect); the vessel protons have a Δf shift while the tissue ones do not.

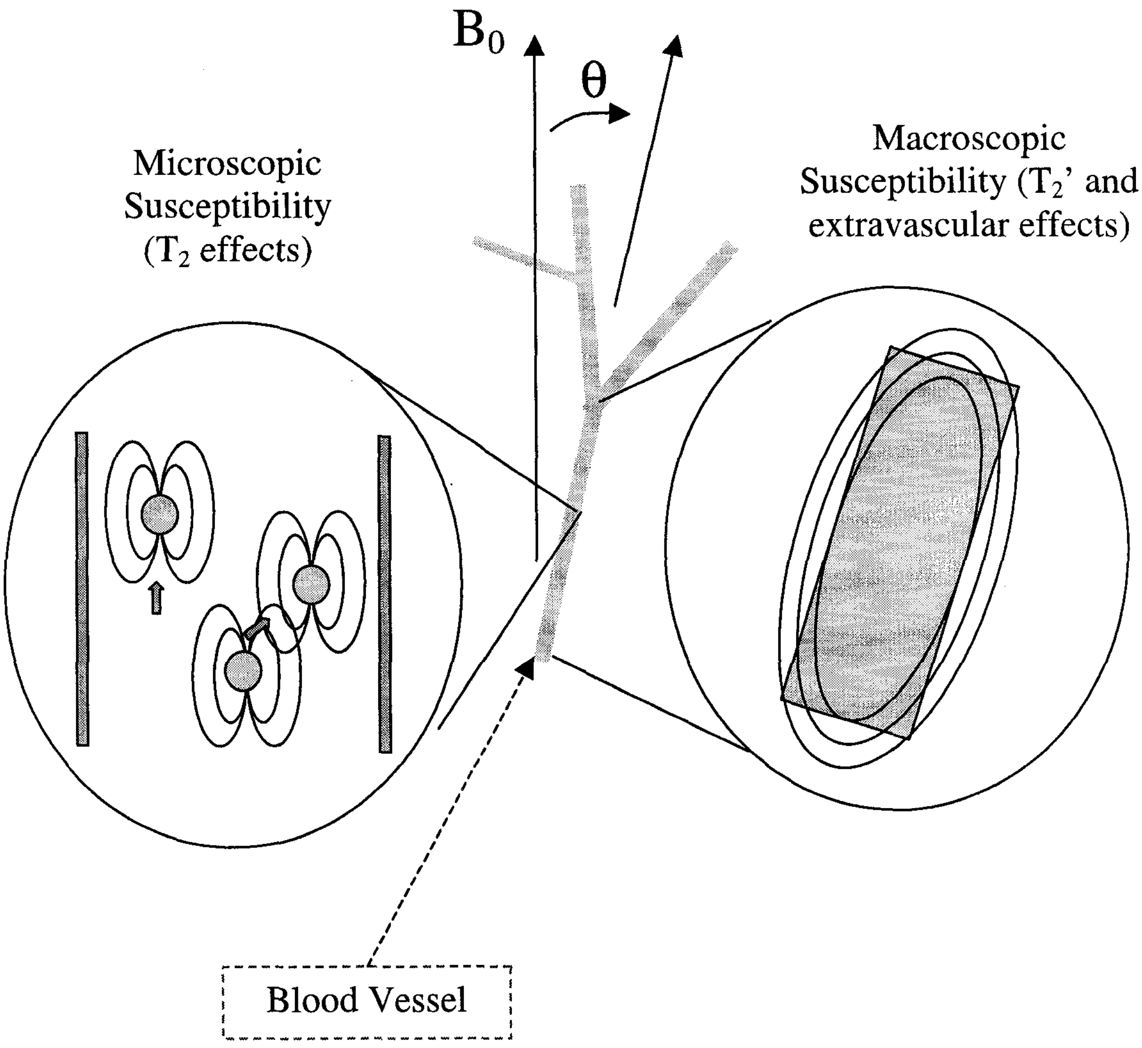

Figure 3-4. The difference in spatial extent between the T_2 and T_2' susceptibility effects of the BOLD mechanism.
In the macroscopic view, all intravascular protons (not shown) in the vessel experience the same field shift (the bar magnet view).

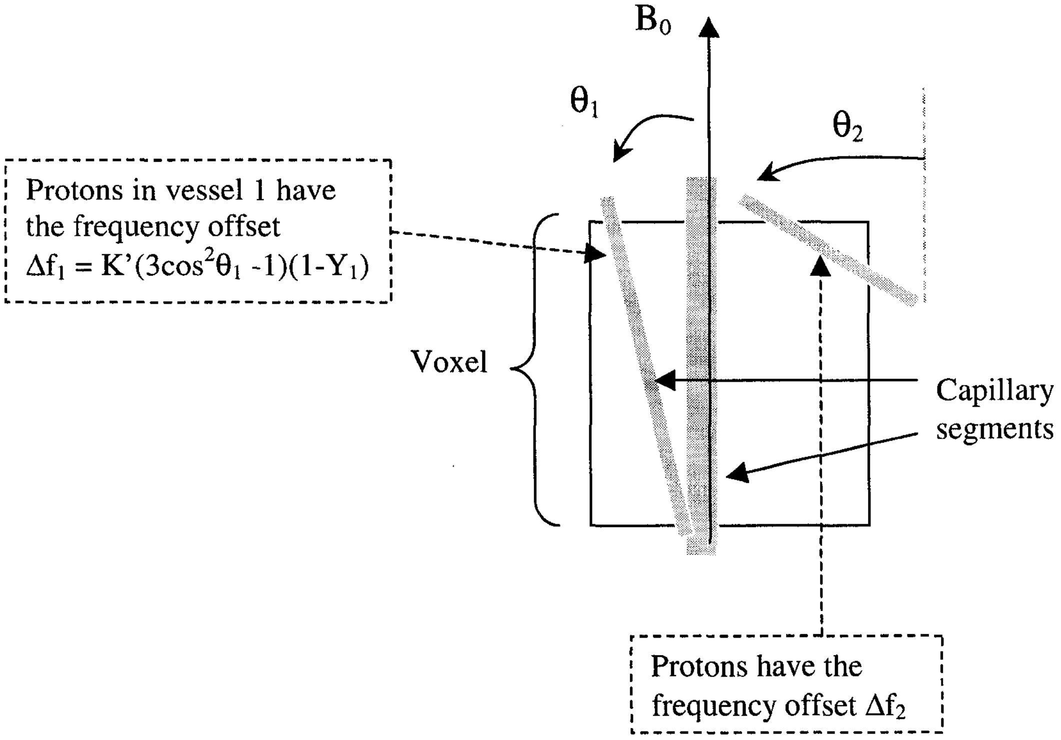

Figure 3-5. Intravoxel dephasing. Owing to T_2' effects, spins in each randomly-oriented vessel segment within the same voxel precess at a different frequency (according to the segment angle to $\boldsymbol{B_0}$). This leads to intravoxel dephasing (refer to figure 2-9b for details).

3.4.4 Extravascular Effects

The macroscopic magnetic field distortions of blood vessels containing deoxyhemoglobin extend beyond the vessel wall (figure 3-6). Extravascular protons diffusing through these disturbances lose coherence resulting in signal decay.

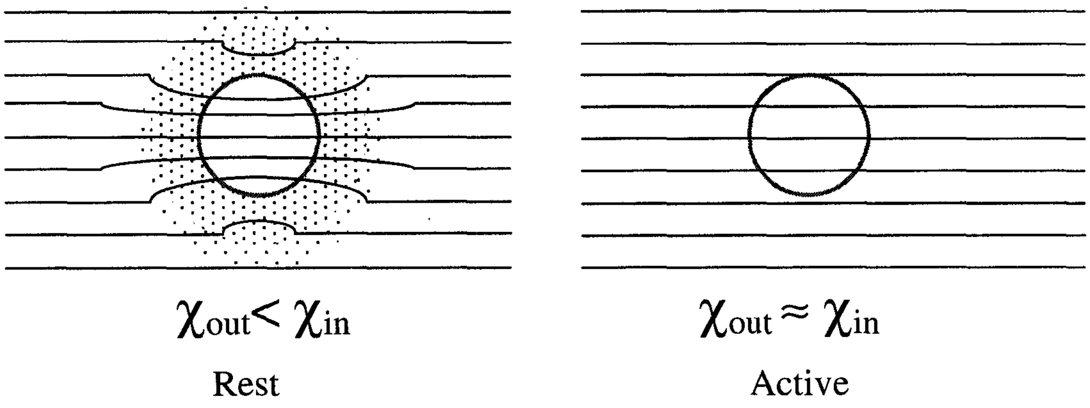

$\chi_{out} < \chi_{in}$

Rest

$\chi_{out} \approx \chi_{in}$

Active

Figure 3-6. A look at extravascular susceptibility effects.
The cross-section of a vessel is shown with the horizontal lines representing magnetic field (B_0) lines. At rest the susceptibility is slightly less negative inside than out due to the presence of paramagnetic deoxyhemoglobin (hence more dense field lines inside the vessel at rest) (Moonen, C.T.W., Bandettini, P.A. Functional MRI p94.).

3.5 The Effects of Field Strength on BOLD Imaging

The BOLD effect is composed of cerebral blood volume, blood flow and oxygenation changes in response to local neuronal activity. These influence signal intensity through the magnetic susceptibility difference between paramagnetic deoxyhemoglobin and surrounding diamagnetic constituents. This susceptibility difference increases with magnetic field strength, developing greater contrast between active and baseline signal intensities, thereby justifying imaging at higher fields.

Several authors have examined the relationship between field strength and BOLD signal changes concluding that higher fields offer greater signal-to-noise, greater functional contrast-to-noise and greater specificity.

The approach used by Gati (1997) was to characterize BOLD field strength effects in two separate compartments: voxels completely filled by large vessels, and voxels placed in cortical gray matter tissue, containing a mixture of microvessels whose diameters were smaller than the voxel itself[10].

The BOLD signal difference between active and resting states may be characterized by[11]:

$$\Delta S = S_0 \bullet \{\exp(-TE \bullet R_{2b}^*)[\exp(-TE \bullet \Delta R_2^*)-1]\} \qquad (4)$$

where S_0 = the fully relaxed signal at TE = 0
R_{2b}^* = the apparent baseline transverse relaxation rate ($1/T_{2b}^*$).

In addition, the change in R_2^* between active and baseline states, (ΔR_2^*) is[12],

$$\Delta R_2^* \approx -(\Delta S/S)/TE. \qquad (5)$$

Functional contrast to noise, is defined as follows[13]:

$$\Delta S/N = \psi \bullet (\Delta R_2^*/ R_{2b}^*) \qquad (6)$$

where ψ = the signal to noise ratio.

Gati found that the visual cortex BOLD differential (active-rest) signal, $\Delta S/S$, was much greater in vessels than in tissue, at all field strengths (at TE = T_2^*, 13.3 ± 2.3%, 18.4 ± 4%, 15.1 ± 1.2% (vessels) vs. 1.4 ± 0.7%, 1.9 ± 0.7%, 3.3 ± 0.2% (tissue) at 0.5, 1.5 and 4T respectively). This can be explained by the much greater blood volume fraction of those voxels within large vessels, and demonstrates the BOLD signal dominance by large vessels. (The negative implication of this large vessel dominance, is that the BOLD signal changes observed in large vessels, can occur downstream of the site of activity, i.e., the microvessel BOLD signal has a greater localization to the site of neuronal activity, or greater specificity).

The signal-to-noise ratio scaled linearly with B_0 in both compartments, while the apparent transverse relaxation rate, R_2^*, scaled greater than linearly in both[14] (figure 3-7). The change in R_2^* between active and baseline states, (ΔR_2^*), was sublinear in vessels yet supralinear in tissue (figure 3-7). As a result (by Eqn (6)), and perhaps most importantly, the functional contrast-to-noise grew less than linearly with B_0 in vessels yet greater than linearly in tissue (figure 3-8). In other words, not only do signal-to noise and functional contrast-to-noise improve with field strength, but the BOLD signal source becomes increasingly tissue-based, that is, more localized to neuronal activity.

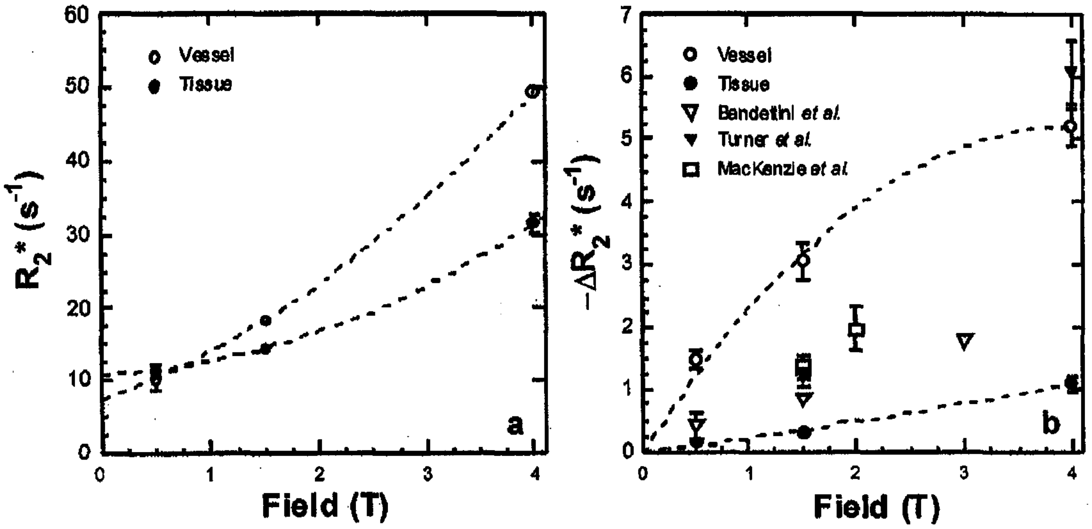

Figure 3-7 The dependence of the apparent (left) and differential apparent (between activation and rest) (right) transverse relaxation rates on field strength. (Moonen, C.T.W., Bandettini, P.A. *__Functional MRI__ p.280 from Gati 1997).*

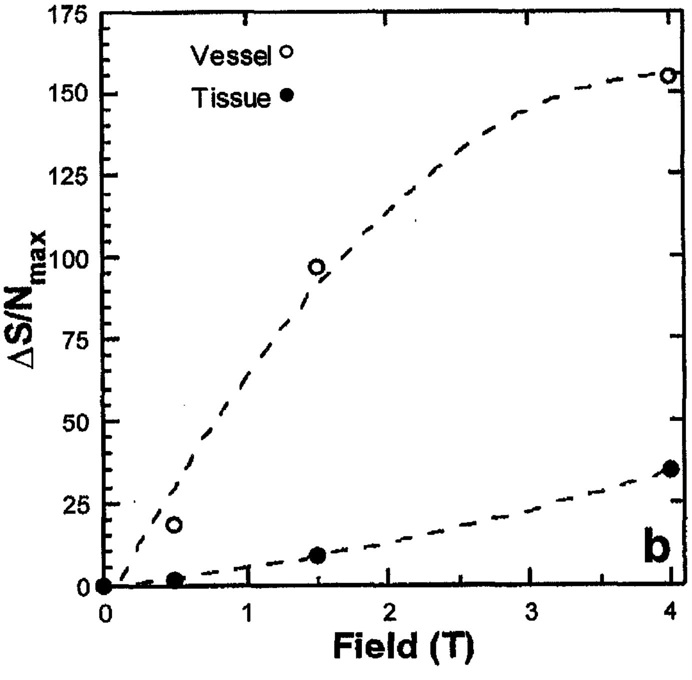

Figure 3-8. The scaling of functional contrast-to-noise with magnetic field strength (Moonen, C.T.W., Bandettini, P.A. *__Functional MRI__ p.281 from Gati 1997)*

Work by Song et al. (1995, 1996 – Functional MRI p106) further reinforced the notion that, by scanning at higher field strengths, the measured BOLD signal is more localized to its neural source. Through careful specification of a dipolar diffusion gradient, he was able to remove intravascular BOLD signals from vessels with flow velocities above a certain threshold. Because flow velocity correlates with vessel size, this allowed him to selectively null any of the larger vessels' intravascular signals, and thereby examine the intra and extravascular BOLD contribution at a given field strength. At 1.5T, the application of a small dipolar gradient ($b = 42\text{s/mm}^2$), dispersing intravascular signals from vessels flowing faster than a few mm/s (i.e. non-capillary vessels), removed almost all of the BOLD signal, while at 3 and 4T, even with a strong gradient ($b = 400\text{s/mm}^2$) a significant amount of the GE BOLD signal survived. This demonstrated that at lower fields the BOLD signal is predominantly non-capillary intravascular while at higher fields it is increasingly extravascular in nature. Since extravascular signals are more localized to the neuronal activity, higher fields tend to increase specificity.

Turner (1993) directly compared the visual cortex BOLD signal intensity measured at 1.5T vs. 4.0T (figure 3-9). Using the same photic stimulation, subjects, sequence and slice position, he found the typical intensity to be 15.1 ± 6.0 % at 4T while 4.7 ± 2.0% at 1.5T[15]. He credited this to the increasing influence of susceptibility effects with field strength.

Empirical findings, such as presented above, have demonstrated activation-induced BOLD signal changes in primary cortical areas ranging from 5-20% at 4T, compared to 1-3% at 1.5T. Using Monte Carlo simulation[16] Ogawa (1993) expanded the current understanding of the BOLD mechanism, quantifying the relative importance of water diffusion, blood volume fraction, magnetic field strength, and oxygenation on the observable signal intensity. This was captured in the following equations:

$$\begin{aligned} R_2^* &= \alpha v b_l && \text{larger vessels (radius} > 8\mu\text{m)} && (7)\\ &= \beta v^2 (b_s)^\gamma p && \text{small vessels} && \end{aligned}$$

and

$$\Delta S/S \approx TE \bullet \Delta R_2^* \qquad (8)$$

where γ, α, and β are constants

v = frequency shift caused by the susceptibility difference between blood and surrounding tissue (i.e. $v = \Delta\chi(1-Y)\omega_0$) (note v is proportional to ω_0 and therefore to B_0)

b = blood volume fraction

p = active vessel fraction (relevant only to small vessels)

$\Delta S/S$ = activation-related signal change

ΔR_2^* = the difference in apparent relaxation rates between active and resting states.

These equations lead to the following conclusions:

1. The BOLD signal intensity change within a voxel consisting of both large and small vessels will have an R_2* decay rate weighted by both vessel terms in Eqn (7).
2. By Eqn (7) and Eqn (8), the intravoxel signal change increases at least linearly with field strength.
3. Finally, once again, small vessels should increase in relative importance at higher fields, thereby leading to greater localization or specificity.

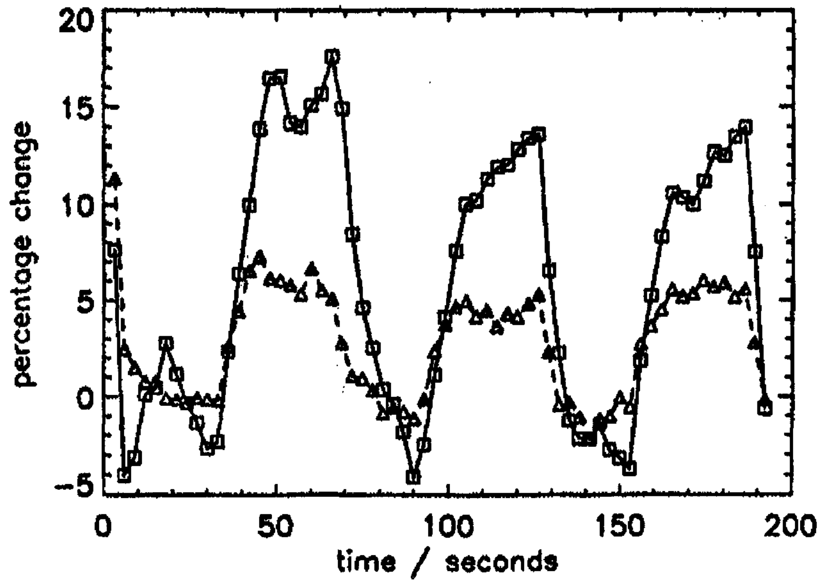

Figure 3-9. The signal intensity during episodes of photic stimulation in a single subject at 4.0T (boxes) and 1.5T (triangles). The data come from an 8 voxel region of interest within the same slice of the visual cortex (Turner 1993).

3.6 Conclusion

The BOLD effect is a physiological response consisting of changes to cerebral blood volume, blood flow and blood oxygenation in response to local neuronal activity. These changes result in a decrease in the intravascular fraction of deoxyhemglobin, reducing the signal decay by dephasing, and thereby leading to functional image contrast between active versus resting states. This effect is the basis for the functional imaging study examining basal ganglia behaviour within Parkinson's patients (Chapter 7). Chapter 9 expands on the advantages in operating at higher field strengths, presented at the end of this chapter, by demonstrating increased functional contrast to noise at 4.7T compared to 1.5T.

3.7 Endnotes

1. The accuracy of BOLD in representing neuronal activity has been addressed by others. It has been shown that BOLD changes are well correlated (both behaviourally and spatially) with cerebral blood flow changes (Zhu et al 1998), which are in turn assumed to reflect neuronal responses.

2. $\{(\Delta CMRO_2/CMRO_2) + 1\}/\{(\Delta CBF/CBF) + 1\} = -\Delta Y/(1-Y) + 1$

   and

   $CMRO_2/(CBF \bullet Ch) = (1-Y)$

   where

   Ch = heme concentration
   Y = oxygenation of venous blood.
   (Grubb 1974 or Boxermann 1995 can be reviewed for the CBF to CBV relationship – the latter assumed CBV α $(CBF)^{0.4}$)

3. Inflow effects can lead to poor localization, that is, they can induce fMRI signal changes downstream of the actual site of neuronal activity, and are therefore typically eliminated.

4. The hemoglobin molecule contains Fe^{2+} ions. When oxygenated, this ferrous iron in hemoglobin exists in a diamagnetic low spin state (S=0), which changes to a paramagnetic high-spin state (S=2) when deoxygenated. (Oxygenation doesn't affect iron's ionic state, but rather results in a binding-induced conformation change altering its ionic spin).

5. This mechanism is not well understood. It is believed however, that the CBF increase begins about 1 second after the initial $CMRO_2$ increase (see Moonen text page 99).

6. The proposed treatment considers tissue and vascular protons separately, but is this reasonable?

   Over the time course of an experiment (say 50ms from RF application to data acquisition) a freely diffusing proton within whole blood at body temperature randomly moves ~25um (from sqrt(6DT), where D, the diffusion coefficient in whole blood ~ $1um^2/ms$). This proton could therefore bump into other protons, RBCs and the capillary wall. Furthermore, protons freely diffuse in and out of RBCs (5ms residence time). Capillary endothelium (the capillary wall) however, is relatively resistant to water transport so that over 50ms, less than 5% of the capillary water protons diffuse into the surrounding tissue.

Outside the vessel, extravascular (EV) protons diffuse through intra and extracellular spaces readily, again with D ~ $1um^2/ms$

Thus, over the typical BOLD fMRI time scale, intravascular water stays within the vessel, extravascular water remains outside the vessel and the two compartments can be dealt with separately.

7. Hematocrit is the percentage by volume of RBCs within a particular unit of blood

8. Since the protons typically move only about 5-25μm over the course of the experiment - less than the capillary segment length - they experience a constant field. Therefore, T_2' effects are refocusable

9. This is a simplification relevant to large vessels. (It is only valid when RBC distortion is confined to the vessel and with a minimal spacing between RBCs).

10. Other authors conducted BOLD vs. field strength experiments; however, only Gati used a high enough resolution to separately consider vessels and tissue. His study therefore better controlled voxel composition as either being large vessel based or strictly microvessel based – in turn making his findings more significant.

11. assuming that the system is fully relaxed (no inflow effects) and that signal decay is mono-exponential with TE.

12. assuming $TE \bullet \Delta R_2^* << 1$ and no inflow effects

13. assuming no inflow, that noise was predominantly thermal (i.e. mostly random vs. instrument instability and physiological change related), and that $TE \approx TE_{opt} = T_2^*$, so that S_0/N or $S/N(TE = 0) \approx \psi \exp(1)$. Insert this final term into (4).

14. Gati empirically characterized the field strength dependence of the R2* values in vessels (R_{2vb}^*) and tissue (R_{2tb}^*) as follows:

$$R_{2vb}^* = 1.27B_0^2 + 5.46B_0 + 7.25$$

$$R_{2tb}^* = 1.09B_0^2 + 0.81B_0 + 10.72$$

It can be seen in the vessel equation that at low fields (0.5, 1.5T) the linear term dominates while at high fields (4T) the linear and quadratic terms are about equal. In contrast, in tissue, at the lower fields the linear and quadratic terms are equal while the quadratic term dominates at high fields.

15. The typical intensity came from an 8 voxel visual cortex ROI, averaged across sessions.
16. The simulations looked at deoxyhemoglobin-induced intravoxel dephasing of protons in tissue surrounding blood vessels.

3.8 References

Bandettini, P.A., Wong, E.C., Hinks, R.S., Tikofsky, R.S., Hyde, J.S. Time Course EPI of Human Brain Function during Task Activation. Magnetic Resonance in Medicine 25:390-397 (1992)

Gati, J.S., Menon, R.S., Ugurbil, K., Rutt, B.K. Experimental Determination of BOLD Field Strength Dependence in Vessels and Tissue. Magnetic Resonance in Medicine 38:296-302 (1997)

Kwong, K.K., Belliveau, J.W., Chesler, D.A., Goldberg, I.E., Weisskoff, R.M., Poncelet, B.P., Kennedy, D.N., Hoppel, B.E., Cohen, M.S., Turner, R., Cheng, H-M., Brady, T.J., Rosen, B.R. Dynamic magnetic resonance imaging of human brain activity during primary sensory stimulation. Proc. Natl. Acad. Sci. USA 89:5675-5679 (1992)

Moonen, C.T.W., Bandettini, P.A. Functional MRI. Springer-Verlag Berlin Germany 1999 Chapters 9-11 and 25.

Ogawa, S., Lee, T.M., Kay, A.R., Tank, D.W. Brain magnetic resonance imaging with contrast dependent on blood oxygenation. Proc. Natl. Acad. Sci. USA 87:9868-9872 (1990)

Ogawa, S., Tank, D.W., Menon, R., Ellermann, J.M., Kim, S-G., Merkle, H., Ugurbil, K. Intrinsic signal changes accompanying sensory stimulation: Functional brain mapping with magnetic resonance imaging. Proc. Ntal. Acad. Sci. USA 89:5951-5955 (1992)

Ogawa, S., Menon, R.S., Tank, D.W., Kim, S-G., Merkle, H., Ellerman, J.M., Ugurbil, K. Functional brain mapping by blood oxygenation level-dependent contrast magnetic resonance imaging. A comparison of signal characteristics with a biophysical model. Biophys J 64:803-812 (1993)

Thulborn K.R., Waterton, J.C., Matthews, P.M. Radda, G.K. Oxygenation dependence of the transverse relaxation time of water protons in whole blood at high field. Biochim Biophys Acta. 714(2):265-70 (1982).

Turner, R., Le Bihan, D., Moonen, C.T.W., Despres. D., Frank, J. Echo-Planar Time Course MRI of Cat Brain Oxygenation Changes. Magnetic Resonance in Medicine 22:159-166 (1991)

Turner, R., Jezzard, P., Wen, H., Kwong, K.K., Le Bihan, D., Zeffiro, T., Balaban, R.S. Functional Mapping of the Human Visual Cortex at 4 and 1.5 Tesla Using Deoxygenation Contrast EPI. Magnetic Resonance in Medicine 29:277-279 (1993)

Zhu, X., Kim, S.-G, Andersen, P., Ogawa, S., Ugurbil, K., Chen, W. Simultaneous Oxygenation and Perfusion Imaging Study of Functional Activity in Primary Visual Cortex at Different Visual Stimulation Frequency: Quantitative Correlation Between BOLD and CBF Changes. Magnetic Resonance in Medicine 40:703-711 (1998)

Chapter 4

Paradigm Designs

4.1 Introduction

In the context of fMRI, the experimental paradigm is a model describing the sequence of stimuli presented to the subject. There are two different types of paradigms used to bring about BOLD-based functional activation – epoch and event-related paradigms. This chapter explains the distinction between the two methods and outlines their respective advantages. Finally, the chapter explores both the necessity of timing synchronization between the MRI scanner and the paradigm generating computer for event-related fMRI, and its implementation in the 1.5T system.

The long half-life of radioactive tracers forced PET scientists to evaluate continuous performance or repeated stimulus presentation paradigms (i.e. long mental states). It was likely a carry-over of techniques from PET to fMRI that led to the appearance of epoch-based experiments in the latter. And while PET and epoch-based fMRI paradigms share similar designs, so also do electrophysiology (evoked potentials) and event-related fMRI studies.

4.2 fMRI Paradigm Design Types

Epoch-based fMRI is more widespread and applies long blocks of stimuli in an alternating on/off pattern (e.g. 30sec of finger tapping alternating with 30 sec of rest). It records the hemodynamic response resulting from repeated stimuli or continuous performance and therefore may be confounded by effects such as attentional set, habituation, anticipation, etc. (Samuel 1998).

The more novel approach in magnetic resonance imaging is event-related or efMRI. While this stimulus presentation model has been used in electrophysiology, it has only recently been applied to fMRI. The distinction between epoch-based fMRI and efMRI is that the former measures the superimposed hemodynamic responses resulting from many events (such as finger taps every 2 sec for a 30 sec period) while efMRI measures the hemodynamic response to a single event (for example one finger tap) (figure 4-1).

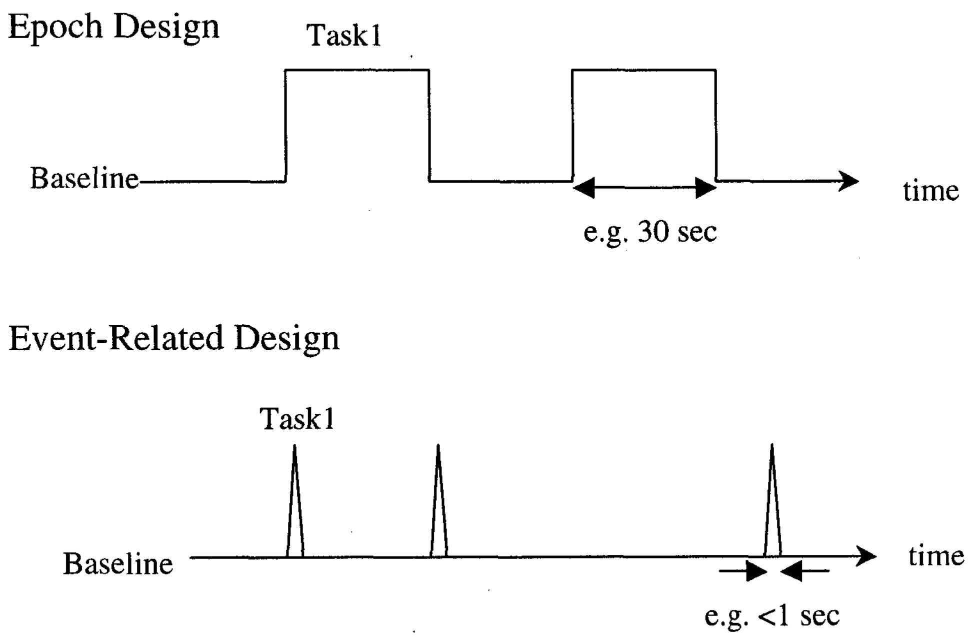

Figure 4-1. Comparing Epoch and Event-related Paradigm Structures.

4.3 Comparing Event-related and Epoch Approaches

4.3.1 Post-hoc Processing

EfMRI allows the researcher to categorize data post hoc on the basis of subject performance, reaction time, etc.

As an example consider Figure 4-2. The diagram shows a typical Go/NoGo paradigm in which the subjects tap their finger following a "Go" stimulus, and withhold a response after a "NoGo" stimulus. The diagram depicts both the epoch-based (top) and event-related (bottom) implementations.. At the top, the subject fails to tap in the centre of the 2nd "Go" block. This block can no longer be statistically modeled as "Go" because any brain activity within that period of time is a combination of both "Go " and "No-Go" actions i.e. finger tapping is confounded by a mistaken rest. This block of data cannot be salvaged and must be removed. In efMRI (bottom diagram), the subject misinterprets a "No-Go" or no response cue, instead finger tapping at that time. Here the researcher can simply reclassify the data, post hoc, as a "Go" or finger tap and the data can be saved.

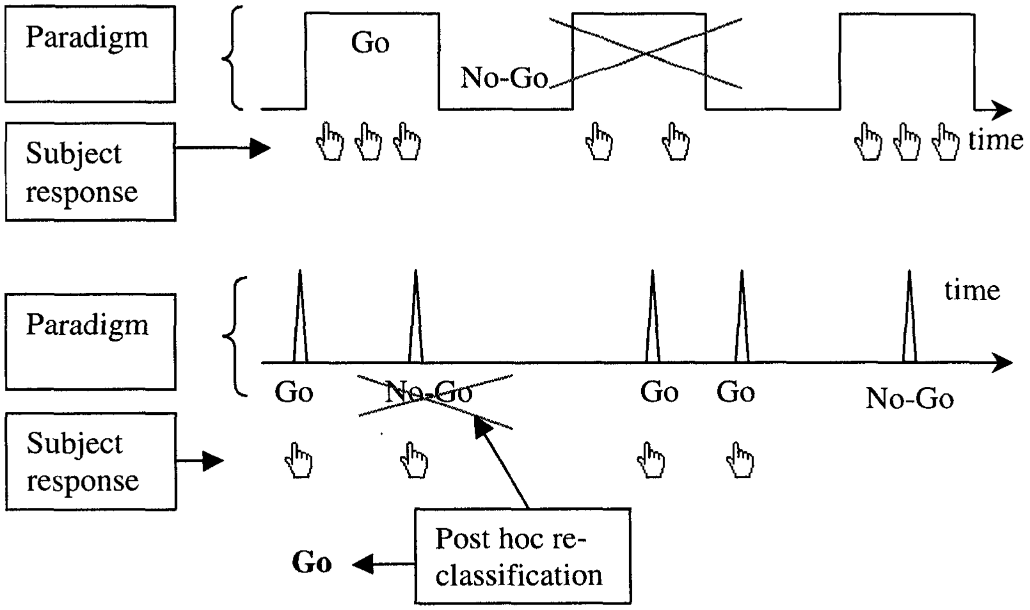

Figure 4-2. efMRI vs. epoch fMRI: post hoc processing. Specifically, this diagram shows that re-classification of an event type following an error by the subject is possible in efMRI, but not in epoch-based fMRI.

4.3.2 Unblockable experiments e.g. oddball experiments

Some experiment types do not lend themselves to the block design; one such example is oddball experiments. An oddball experiment observes the effect of a stimulus defying the prevailing context. Typically such a stimulus is presented both infrequently and randomly and hence is an oddball. The block design with regularly timed, predictable and equiprobable stimuli is not conducive to this type of experiment (figure 4-3).

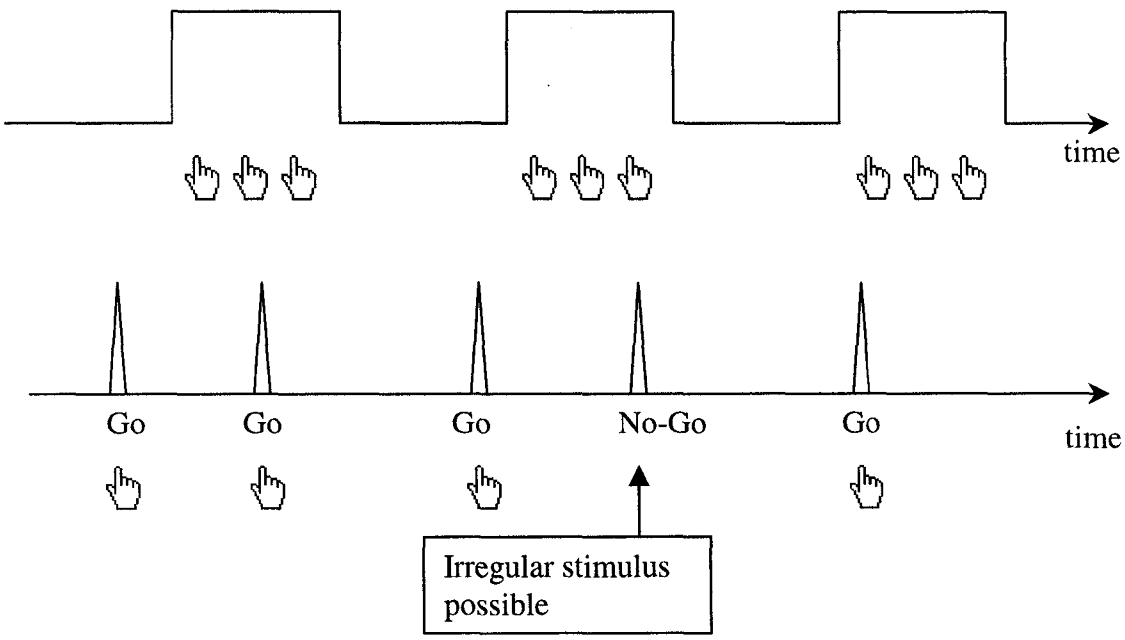

Figure 4-3. efMRI vs. epoch fMRI: oddball experiments. The diagram illustrates that oddball paradigms can only be applied as efMRI and not as block-based designs.

4.3.3 Unpredictable events

Event-related paradigms alone are suited for modeling unpredictable events that can only be indicated by the subject e.g. hallucinations. Within the confines of the regular intervals of block design it is unrealistic to have a hallucination for 30sec, then rest for 30 sec etc. It is however, possible to design this as an efMRI experiment, implemented as a button press each time the subject experiences a hallucination (figure 4-4).

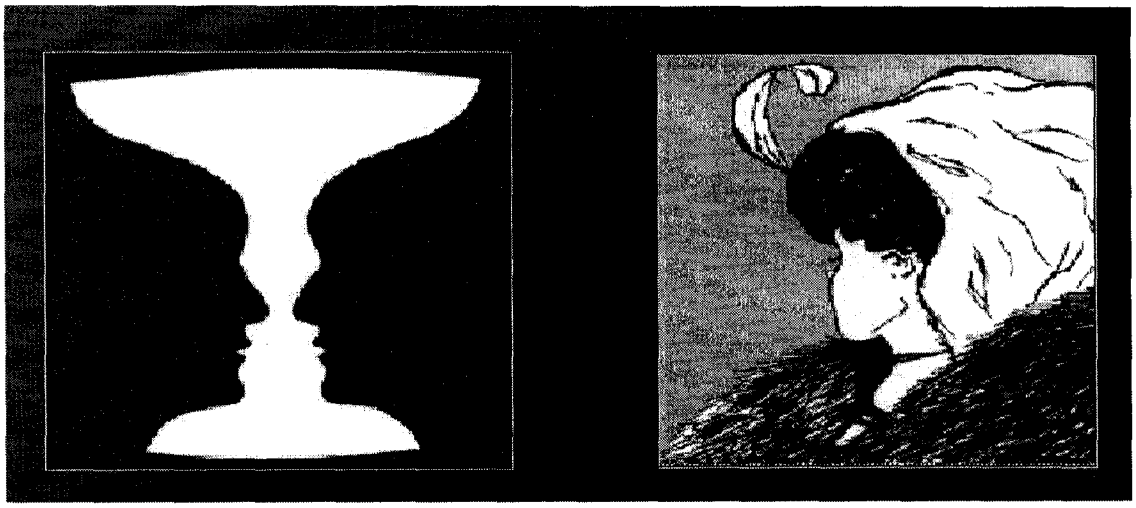

Figure 4-4. efMRI vs. epoch fMRI: modeling unpredictable events.
In efMRI, a possible experiment using either of these images, might be for a subject to push a button each time his/her perception changes. The most reasonable block equivalent would ask the subject to maintain each perceived image for 30sec – this is unrealistic and would be rife with errors (SPM 2002 course notes - reference 1).

4.3.4 Randomization of Trials and Controllable Context

EfMRI design offers a great deal of freedom, allowing individual stimuli to be presented at random intervals and different types to be intermixed in any way. Randomization of stimuli, or trials, ensures that neither cognitive (e.g. attentional) state nor previous trials alter or confound the hemodynamic stimulus response. An example of the former is habituation, which can develop over the course of continuous performance and hence plagues block designs yet is relatively non-existent in efMRI (figure 4-5). In essence, the random timing and order of stimuli in efMRI prevent the subject from predicting responses, thus efMRI requires greater attention to the task throughout the experiment.

Furthermore, efMRI allows for controllable context. Suppose that a block design consists of task A regularly alternating with task B. Since B always follows A, it is possible that neural activity during the B block is shaped by having conducted A earlier. That is, one assumes that the response to B is the same whether or not task A is conducted at all; however, in reality A could precondition the response to B in some way. EfMRI allows randomization of trial types and thus one controls this preconditioning entirely – it can be included, avoided through randomization, or even tested for, by comparing B activations when B follows A as opposed to when it follows another B.

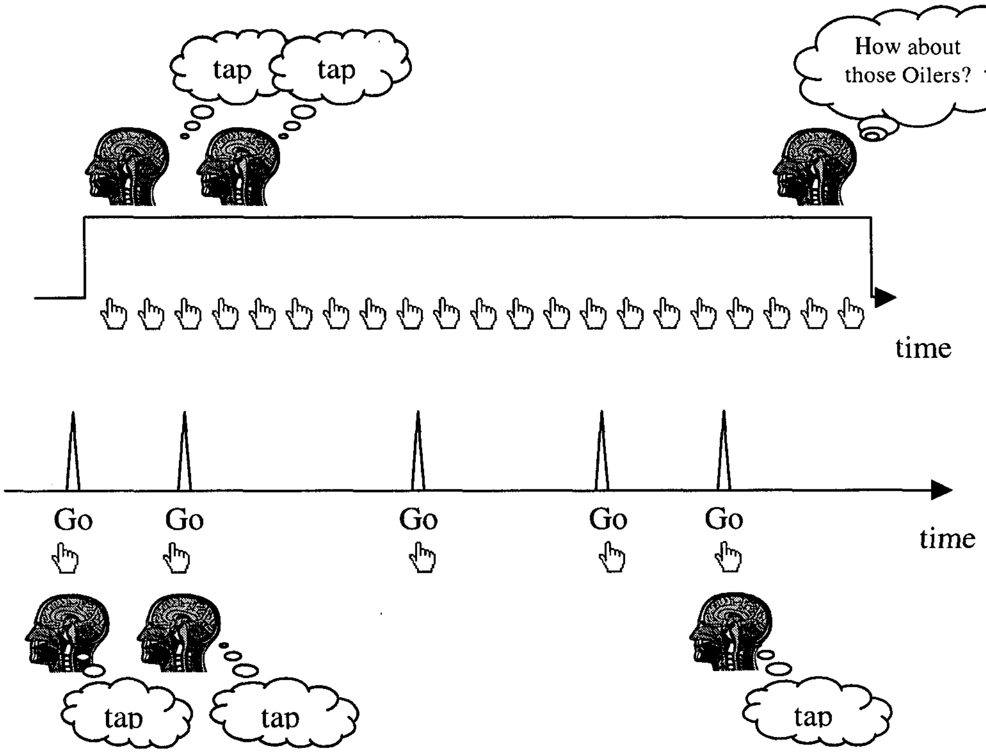

Figure 4-5. efMRI vs. epoch fMRI: the effects of habituation/boredom.
The epoch design (top) is susceptible to such effects while efMRI (bottom) is largely immune to them due to less common, less regular stimulus occurrence.

4.3.5 Latency Information

EfMRI provides much more temporal information about the hemodynamic response function (hrf) (see figure 4-6 for an example). For example, activations in the same brain region, elicited by two separate tasks, can be compared temporally in order to see if one task induces a faster response than the other. In epoch experiments, the observed signal intensity time course represents the summation of many such individual hrfs and thus information about specific shape or timing is lost (figure 4-6).

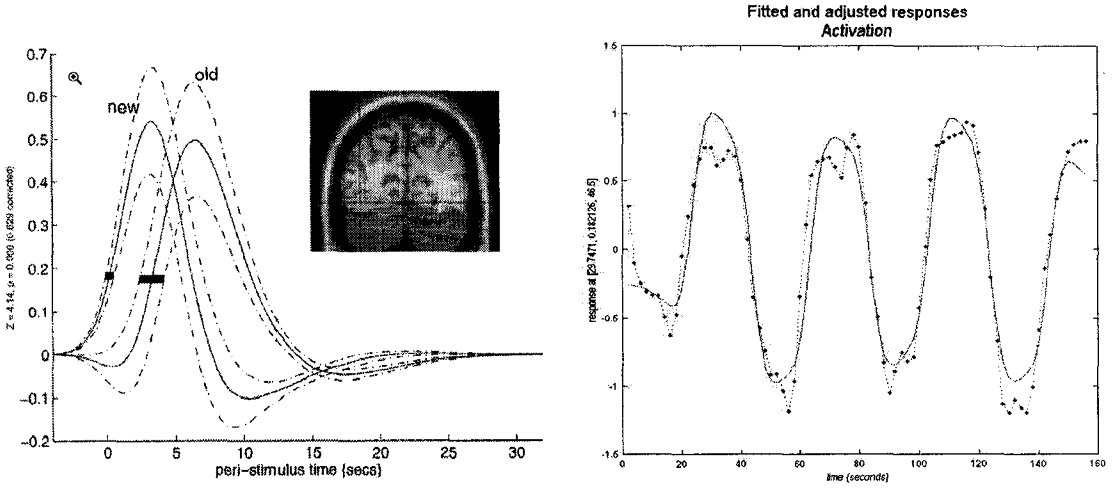

Figure 4-6. efMRI (left) vs. epoch (right) fMRI: latency information.
The left shows two hrfs (each with 2 dotted standard error curves) elicited from the same region of the brain - one resulting from the "new" stimulus, the other from the "old" one. It is clear that the "new" stimulus evokes a more rapid hemodynamic response. The right diagram shows a typical activation from a block design. Each rounded peak is the summation of many individual hrfs which can no longer be individually resolved (Friston 1998).

4.3.6 Event-related vs. Epoch Analysis for Epoch Paradigms

Under certain conditions, modeling blocked data by single events yields a better fit of the model to the data. For example, if the interstimulus interval within an epoch is relatively large, such a model would better account for intra-epoch response fluctuations (figure 4-7).

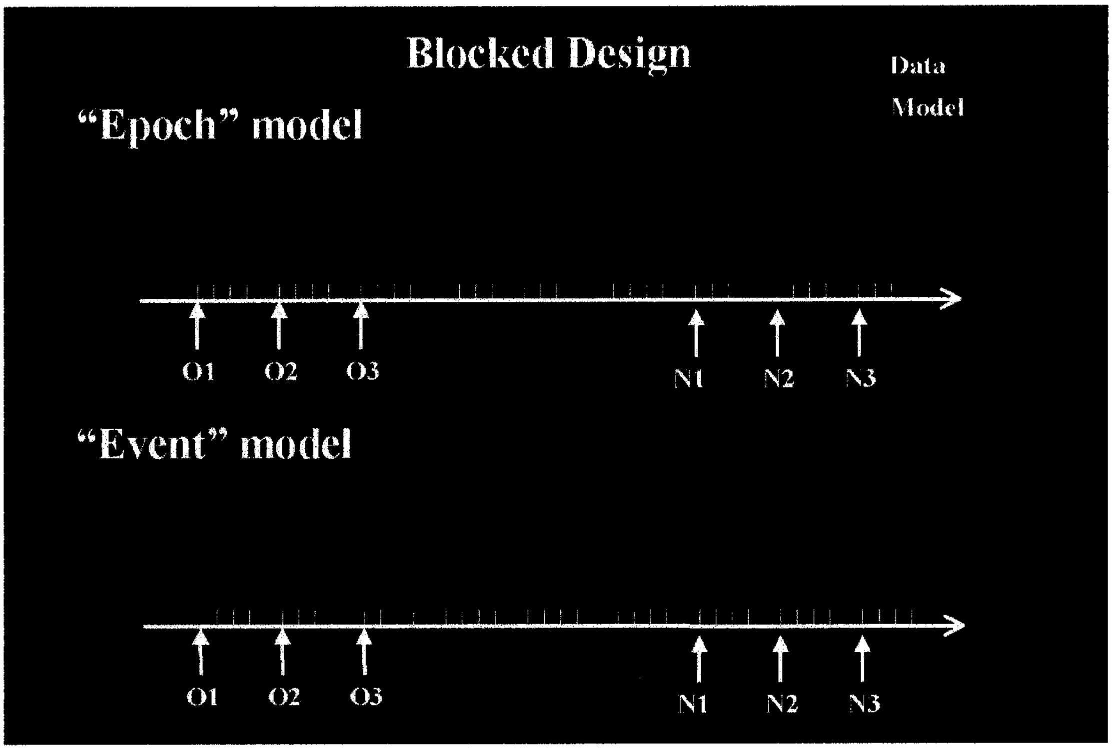

Blocked Design

Data

Model

"Epoch" model

"Event" model

Figure 4-7. efMRI vs. epoch fMRI: choosing the best model for the data. Modeling blocked data as single events as opposed to a "top hat" may yield a better fit of the predicted (modeled) activity to the observed data (SPM 2002 course notes - reference 1).

4.3.7 Statistical Strength

Block-design experiments are more powerful statistically than event-related ones and are thus more efficient in detecting effects (Bandettini 2000)[1]; if a loosely equivalent paradigm could be applied to both experiment types, the block version would display a greater functional contrast (more significant activation). The explanation is simple: epoch paradigms have a greater density of stimuli over time (i.e. a greater number of "active" observations) increasing the statistical certainty of the observations. This is a considerable strength, especially when studying a region such as the basal ganglia which has small BOLD signal and inconsistent activation among subjects.

4.3.8 "Blocked" Tasks: Physiological Processes or Parametric Variations

Just as some particular experiments can only be tested with efMRI designs (e.g. oddball), others require epoch designs. Some psychological processes, such as task switching, may be better suited to the block design.

4.3.9 Sequential Dependencies

Proponents for randomization of stimulus types point out that block designs with repetitive blocks of identical stimuli permit the subject to create specific retrieval strategies. For example, during an epoch one may get into the mode of conducting a certain task. This may be avoided by a randomized design.

This has been challenged by others, using event-related potentials (ERPs), who point out that the neural response to stimulus type A may be different depending on the preceding stimulus or sequence of stimuli leading up to A (e.g. Duzel and Heinze 2002)[2] (figure 4-8). If one stimulus type does influence another, the randomized approach averages the response of one task in many different contexts, for example the "A" response could be averaged from A following B, A following BB, and A following A, all of which may be slightly different. These scientists conclude that randomized designs do not necessarily yield a homogeneous dataset (i.e. a uniform response to "A") and that under certain conditions block designs with fewer sequence effects may be preferable[3].

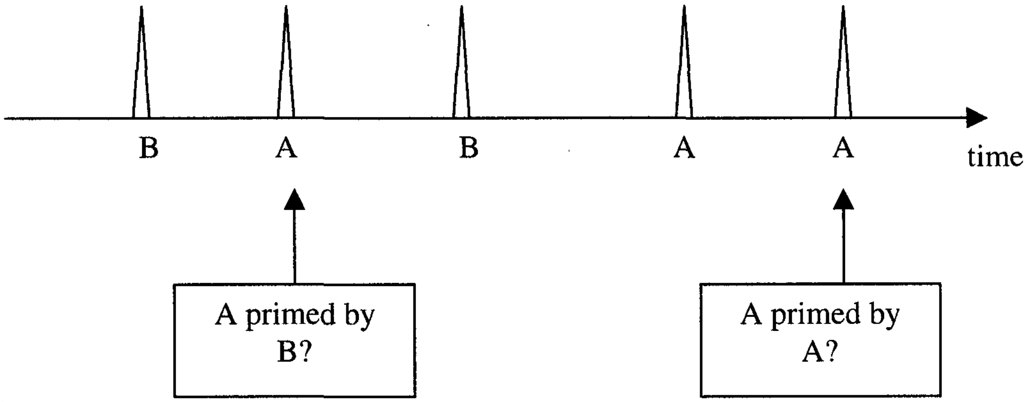

Figure 4-8. An illustration of potential sequential dependency effects. In this example the response to stimulus A may be affected by the preceding stimulus or stimuli.

4.4 The Precise Timing Requirements of efMRI

While efMRI offers several advantages over the block approach, it also requires much more precise stimulus timing. Stimulus timing errors can have serious consequences such as removing true activation, adding false activation and befuddling intentional hemodynamic oversampling. These errors were circumvented by creating a trigger circuit synchronizing the paradigm computer to the MRI scanner. These topics are discussed below in greater detail.

4.4.1 The Source of the Faulty Timing

During a functional imaging study, two separate computers control the image acquisition and the stimulus presentation – the former is the MRI scanner computer, the latter the paradigm machine. The paradigm machine uses Superlab® stimulus presentation software. This program is able to coordinate visual and auditory stimuli as well as record subject pushbutton responses. Superlab allows the user to specify stimulus duration in ms resolution which suggests precise timing control, and yet in practice, for unknown reasons, this program produces erratic timing. Over the course of an experiment this can result in a several second discrepancy between the theoretical experiment length and the actual delivery time measured with an independent clock.

The example relevant to this thesis, is the event-related recreated Garavan study (Garavan 1999) presented in Chapter 7. This experiment displays 1000, 500ms visual stimuli (single letters of the alphabet). When each was given this duration in Superlab, the experiment was several seconds late. The optimal specified time was 493ms. Even at this time the sequence was usually about 1 second short; however, when extended to 494ms per stimulus the sequence became 5 seconds too long (1000 * (+1) ms should have added only 1 second). Finally, for a single duration (e.g. 493ms), the overall experiment length fluctuated from session to session.

4.4.2 The Consequences of Timing Error in Block and Event-Related Experiments

In the subsequent discussion, a temporal shift refers to a shift in both the stimulus, and naturally, in the resultant hemodynamic response (hrf).

The lengthy blocks of stimuli (e.g. ~ 30seconds) characterizing epoch designs, makes them largely immune to temporal shifts of even a few seconds (over the course of the experiment). Under these circumstances, even if the researcher is unaware of the shift, sufficient overlap (correlation) still exists between the unshifted user-specified model and the shifted hrf, such that SPM classifies the voxel as being active (figure 4-9).

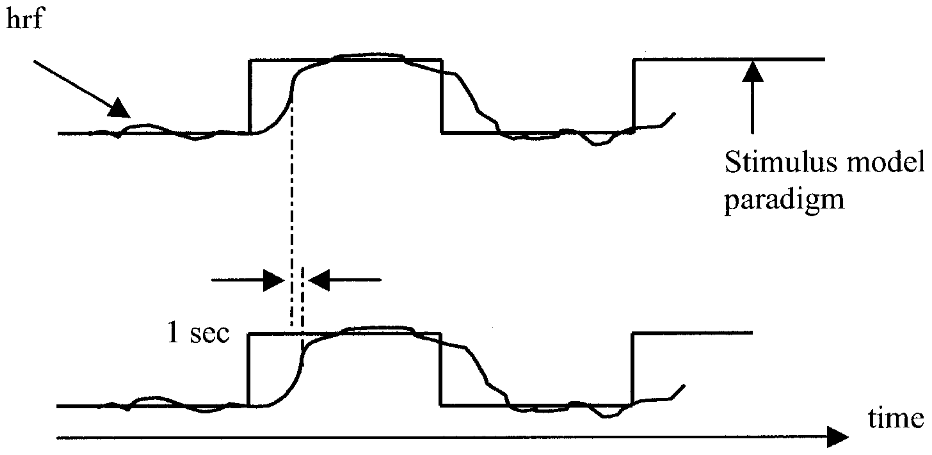

Figure 4-9. The effect of stimulus presentation timing errors on epoch-based fMRI. The hrf of an active voxel (red line) is shown superimposed on the user-specified stimulus model (black). The top line depicts the ideal case. Despite a 1 second delay in stimulus presentation compared to the model, sufficient overlap of the hrf and model remains and SPM99 still identifies the voxel as being active (bottom).

In event-related fMRI, stimulus shift effects can be devastating. Precise definition of stimulus application times is critical because here the stimulus is modeled not as a block of data, but as a delta function. Incorrect modeling can introduce a number of harmful effects including: adding false activations, removing true activations, creating an artificial hrf delay and confounding oversampling.

4.4.2.1 EfMRI timing errors: Removal of True Activations

Physiologically, there is a delay between a stimulus and the hemodynamic response (figure 4-10A). SPM accounts for this by convolving the modeled delta function by a "typical" hrf. If the actual stimulus and hrf are shifted forward relative to the modeled stimulus by a Superlab timing error, the hrf could precede the modeled stimulus. Since this is biologically impossible, an active voxel is falsely classified as inactive (figure 4-10B).

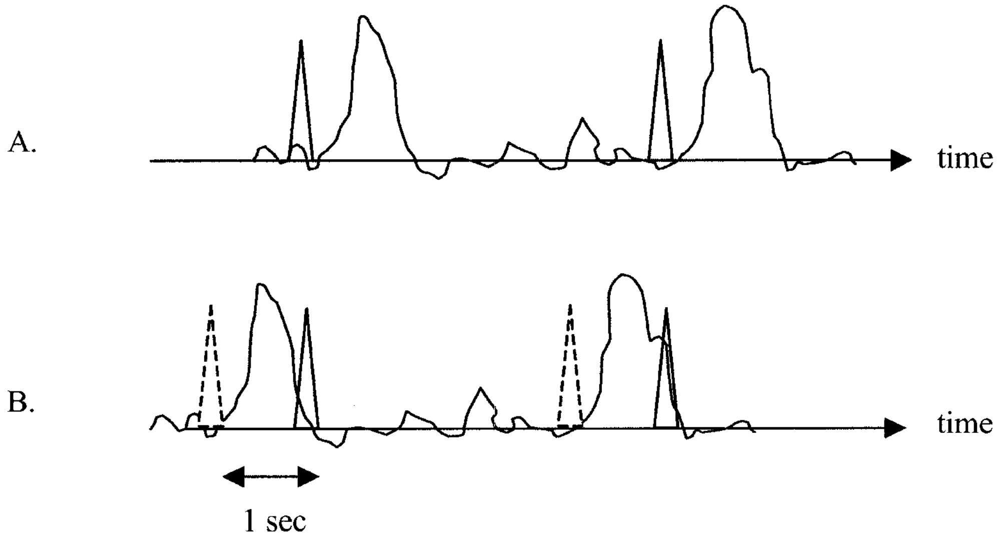

Figure 4-10. Timing inaccuracy leading to removal of true activation.
A physiological delay exists between the stimulus and the hrf (A). In the event that timing errors present the actual stimulus (blue/gray) earlier than modeled (black), the hrf within this active voxel could precede the modeled stimulus thereby making the voxel appear inactive.

4.4.2.2 EfMRI timing errors: Introducing False Activations

Just as temporal shifts can eliminate good activation, they can also lead to false activation. Expanding the Garavan example presented earlier, subjects respond exclusively to the letter "x" or the letter "y", ignoring all others. Once again, each stimulus lasts only 500ms. A several second shift from the modeled to the actual "x" presentation time, might result in the hrf being falsely attributed to the wrong stimulus type (figure 4-11).

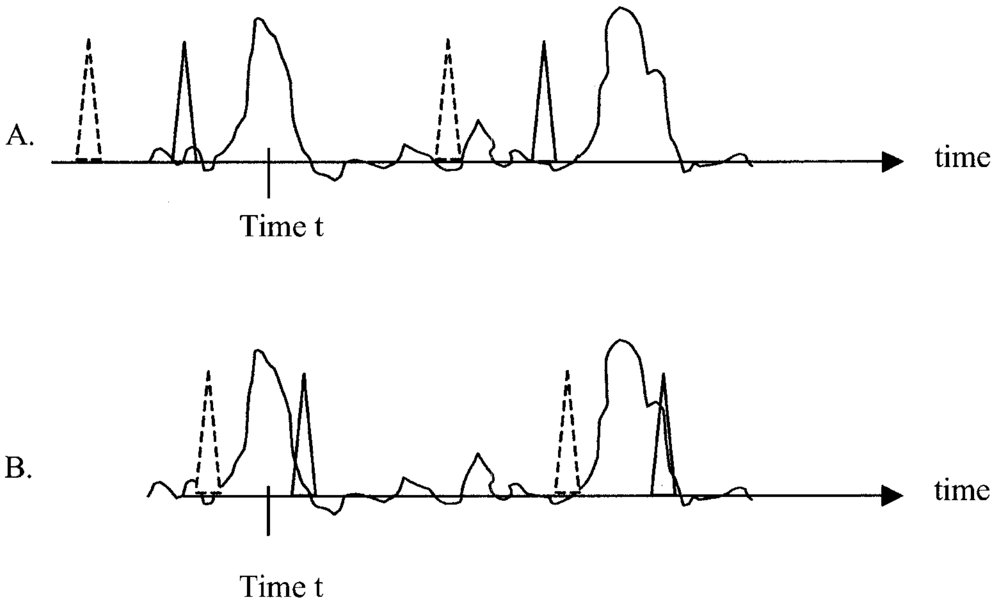

Figure 4-11. Timing errors leading to false activation.
Superlab presents the stimuli early. One stimulus type (black cone) induces the hrf (4-11A). The user model is late relative to the actual (Superlab) one; therefore, activation is incorrectly attributed to a second stimulus type (dotted cone) (4-11B).

4.4.2.3 EfMRI timing errors: False hemodynamic delays

Within efMRI research, one question of interest is: within a particular voxel, does task 1 evoke a faster hemodynamic response than task 2? Stimulus presentation timing errors resulting in incorrect specification of onsets hampers the validity of such analysis (figure 4-12).

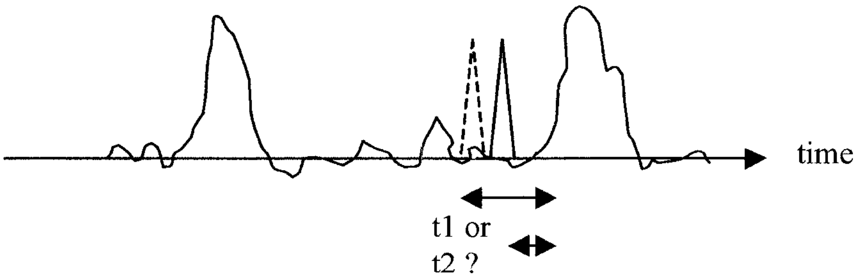

Figure 4-12. *Superlab inaccuracy resulting in an artificial hemodynamic response delay. The difference between the actual (solid cone) and the modeled stimulus (dashed blue) exaggerates the hemodynamic delay (t1 vs. t2).*

4.4.2.4 EfMRI timing errors: Confounding Oversampling of the hrf

Timing errors can adversely affect oversampling. In order to understand how they do so, one must first understand oversampling itself (Friston 1998, Josephs 1997).

Oversampling is a technique that increases the temporal resolution of the recorded data by altering the phase of the stimulus in relation to the acquisition. For multislice imaging, a finite delay is introduced between successive acquisitions of a particular slice, as the remaining slices are collected. This delay is the repetition time or TR. As a result, the hemodynamic response in a given slice is sampled regularly once every TR. If the stimuli were presented at exactly the same instant relative to each slice, then the resultant hrf would be sampled over and over at exactly the same time points and the resolution would be limited to TR. A better method is to alter stimulus presentation such that it does not coincide to even multiples of TR. This allows for much finer effective sampling of the hrf (figure 4-13).

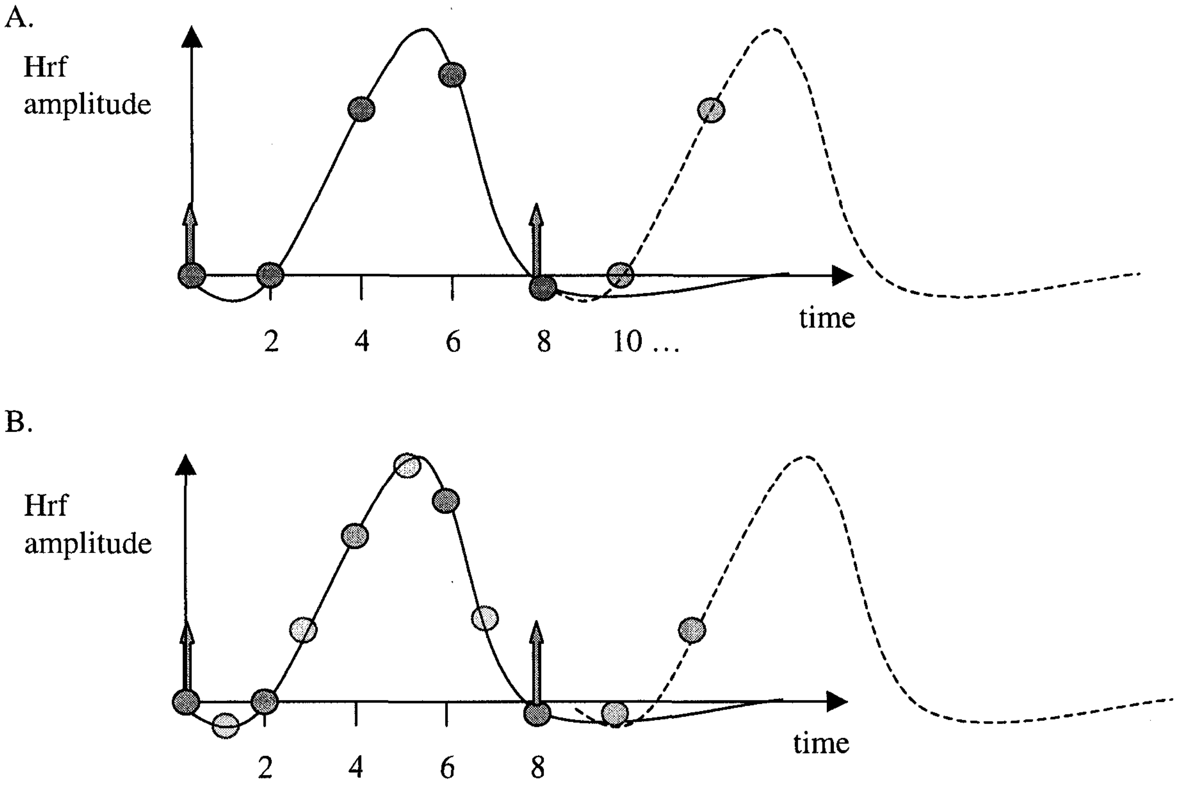

Figure 4-13. Oversampling the hemodynamic response function (hrf)
The diagram illustrates the stimuli (arrows) and the resultant hrfs (curves) for a single voxel in the brain.

A. *Stimulus presentation (SOA or stimulus onset asynchrony) is a multiple of TR (here 2 seconds). The dots illustrate the sampled points of the hrf. Note that all hrfs are sampled at the same time instants, thus the "typical" hrf resulting from the stimulus is sampled only every TR seconds.*
B. *SOA is not a multiple of TR. Each hrf is sampled every 2 seconds (the 1st hrf is sampled at the times indicated by the dark dots, the 2nd during the light dots). The "typical" hrf, has therefore been sampled at twice the original TR resolution (as shown by the first hrf whose samples are placed commensurate with their latency after the stimulus).*

Once again, imagine that the scanner and paradigm timings are not equal. Suppose that 3 adjacent slices of the brain are imaged, and that the stimulus is meant to coincide with acquisition of the 1st slice. At first this is the case; however, timing errors gradually shift this stimulus in time until it occurs during acquisition of the 2nd slice and so on. On one hand, this is only a minor problem since: a) SPM conducts slice timing correction to make it seem as though every slice were acquired at exactly the same instant following a stimulus, and b) it increases the sampling resolution of the hrf (oversampling).

However, a detailed experimental design creates its own oversampling, i.e. an experimenter carefully plans stimulus timing so that over the course of the experiment, each slice has had the same number of onsets. Unpredictable shifting of the stimulus times can undo the experimenter's desired oversampling routine.

4.4.3 Synchronizing the Paradigm and Scanner Computers

The timing errors were removed by having the MRI scanner, with accurate timing, dictate the paradigm timing. The Siemen's MRI scanner has the ability to emit a 10 μs optical signal, coinciding with the onset of each volume scanned (every TR). This is known as a trigger pulse. A circuit was created that converts this optical signal into an electrical signal (figure 4-14). Pre-existing downstream equipment lengthens the pulse to 500ms and sends it to a pushbutton response box that is operationally connected to Superlab on the paradigm computer. Superlab interprets this incoming signal as the pushing of button number 5. By using this triggering, timing deviations can accrue only over one TR (e.g. 2 seconds) and not over the entire paradigm (e.g. 7 minutes).

4.4.3.1 Triggering Applied to the Recreated Garavan Experiment

Having established trigger communication between the scanner and paradigm computers, the Superlab paradigm was rewritten to take advantage of these timing changes. Once again, the reader is reminded that the event-related experiment used in this thesis (recreation of Garavan 1999) has a 2 second repetition time, and that each stimulus (a letter of the alphabet) has a 500ms duration. The paradigm was first modified such that each letter could be terminated either once its pre-established duration expires, or by the trigger signal. This incorporates the trigger within the paradigm; however, in order for the triggering to be of benefit, an optimal stimulus duration must be determined. Remember that despite being programmed to last 500ms, the actual Superlab stimulus durations can be either less than or greater than 500ms. Suppose that the actual stimulus duration is less than 500ms. Five consecutive stimuli following a trigger might last for 493ms, 495ms, 495ms, 494ms and 23ms respectively. Note that the 5th letter was clipped by the next trigger signal at the 2-second mark and was far too brief. Clearly stimuli must not be less than 500ms (in actual time). Instead, all letters were specified to be greater than 500ms. The following durations might result if each letter was assigned a 504ms duration: 503ms, 505ms, 503ms, 489ms. Note that the final letter is terminated prematurely by the trigger signal. Such slight clipping is not noticeable. Experiment timing is now controlled, as each 4-letter block is restricted to the 2-second interval. As a result, any stimulus will at most typically be a few ms off and never on the order of seconds late.

4.4.3.2 Further Modifications – ASCII signals and a Constant Voltage Source

Two subsequent modifications to the trigger circuit were required in order to correct for timing errors that arose during initial tests: a change in the data transmission from the response box to Superlab, and the addition of a constant voltage source. During initial tests, periodically a letter would be clipped to an approximate 10ms duration. It was determined that if the subject being scanned pressed the pushbutton response for button 1 at almost exactly the same time as the trigger pulse occurred, Superlab interpreted this as two triggers. This behaviour was clarified using the HyperTerminal. The RB-620 response box emitted one byte of data (one alphabetical symbol) when a button was pressed, and another when it was released. Thus button 1 was ~□ and similarly button five was _□. If the two button signals were too close in time, a hybrid was formed, for example _^_ or _^~□, instead of the correct juxtapositions ~□_□ or _□~□. Near simultaneous button presses permitted the first button's onset signal to be sent; however, the following data was a mixture of that signal's termination byte and the next signal's onset byte. The two underscores of the former hybrid, _^_, were interpreted by Superlab as two triggers in rapid succession. This error was avoided by incorporating a Superlab software patch allowing for data transmission in the ASCII mode. Although the RB-620 was capable of operating in this mode, prior to the patch, Superlab was not.

The significance of ASCII mode is that unlike the alternate mode, one and only one character is transmitted for each button press. For example, a button 5 press is represented as a "5" instead of "_" and '□". Consequently, the user can no longer detect when two or more buttons are pressed simultaneously because a termination byte is no longer sent following a button release. Therefore, by limiting the representation of the button pressing action to a single byte, no overlap between the press and release of near simultaneous button signals is possible, removing with it the possibility of forming a hybrid two-trigger signal.

A second anomaly, early conclusion of the paradigm, was attributed to voltage problems. Initially, 9VDC batteries were used to power the circuit; however, it was found that the battery voltage drained very quickly, for example, dropping by about 0.5VDC over a matter of minutes. Once the input voltage fell too low, the optical receiver no longer had sufficient input power (it required a 4.75VDC minimum) and ceased working properly. Once the circuit stopped functioning, the temporal control of the triggering process was lost. Since none of the components were either damaged or overheating, the obvious solution was to replace the battery voltage source with a constant voltage source - a 120VAC to 9VDC adapter. By changing the voltage source type, functionality of the trigger circuit and accurate timing were restored.

Conversion to TTL

Manufacturer's suggested circuit

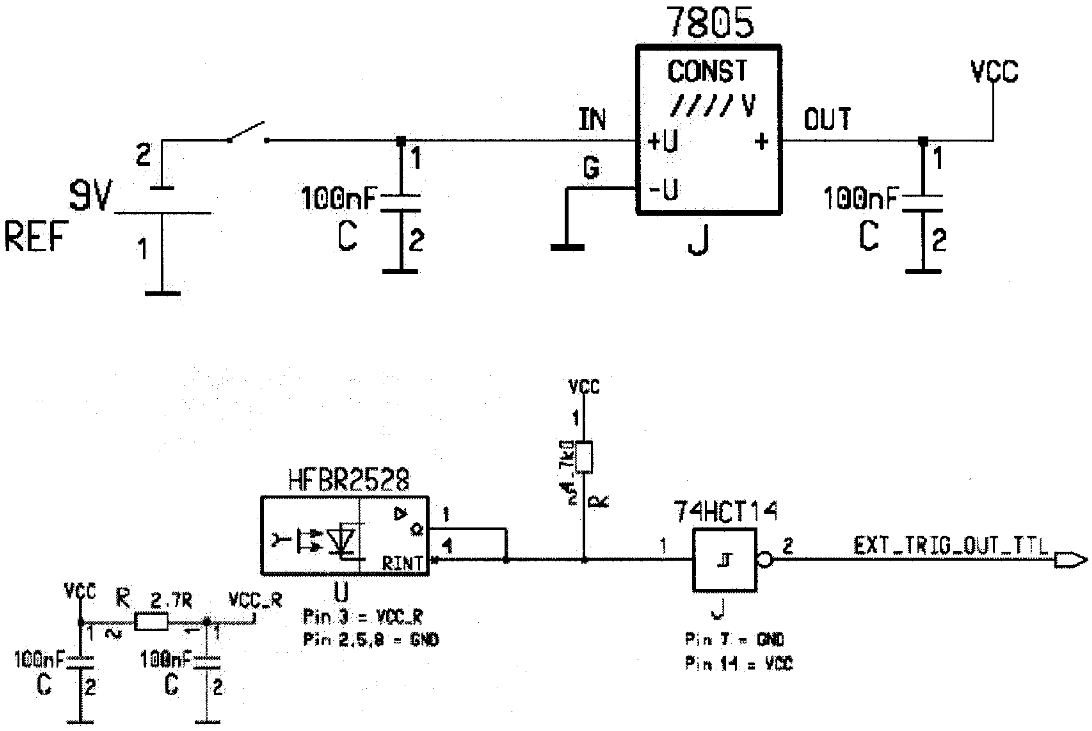

Figure 4-14. Circuitry to convert an optical signal into an electric one. The circuit itself is depicted in the bottom while its power supply (4.75 to 5.25V) is shown at the top.

4.5 Conclusion

The event-related design offers many advantages over the traditional epoch-based approach including, and most pertinent to the event-related study in this thesis (Chapter 7), allowing for post-hoc reclassification of event-types, oddball experiments and randomization of trials. The fundamental weakness in this approach is the much lower statistical strength compared to epoch designs. Finally, this chapter explored the creation of a circuit to properly control the timing of the event-related paradigm in Chapter 7. This is necessary to avoid negative effects such as the removal of true activations or the addition of false ones.

4.6 Endnotes

1. Bandettini and Cox 2000 reported that at optimal constant ISI (interstimulus interval), and with a stimulus duration of 2 seconds, efMRI functional contrast was 65% of that of epoch fMRI.

2. One of Duzel and Heinze's findings is described here. They showed that a change of sequence only produced a significant effect for new words and not for old words (i.e. the ERP was similar for old words whether preceded by an old word (no change) or a new word (change); however, for new words, the ERP was significantly greater if the preceding word was old (change) than if it was also new (no change). This shows that some stimuli may be affected by sequence (new words) while others are not (old words).

3. Within my recreation of the Garavan efMRI experiment how do I control for sequential dependencies?

   The two stimulus types Target (T) and Lure (L) always follow at least a few unimportant letters (I) and thus each is presented in a similar context. If one ignores the (I) letters, then the paradigm still ensures that (L)'s always follow (T)'s (same context) and due to the oddball nature of the paradigm and the subsequent rarity of the Lures, almost all (T)'s follow other (T)'s. Nevertheless one may argue that some sequential effects still exist for (T)'s. The final counterargument though is that the Parkinson's response to the (L)'s is of the most interest in the study thus even if the (T)'s are confounded slightly, it is not terribly important.

4.7 References

http://www.fil.ion.ucl.ac.uk/spm/course/notes02/

Bandettini, P.A., Cox, R.W. Event-Related fMRI Contrast When Using Constant Interstimulus Interval: Theory and Experiment. Magnetic Resonance in Medicine 43:540-8 (2000)

Duzel, E., Heinze, H.J. The effect of item sequence on brain activity during recognition memory. Cognitive Brain Research 12:115-127 (2002)

Frackowiak, R.S.J., Friston, K.J., Frith, C.D., Dolan, R.J. and Mazziotta, J.C. Chapter 18 Human Brain Function, Academic Press 1997

Frackowiak, R.S.J., Friston, K.J., Frith, C.D., Dolan, R.J. and Mazziotta, J.C. Chapter 19 Images of the Future: A Philosophical Coda. Human Brain Function, Academic Press 1997

Friston, K.J., Fletcher, P., Josephs, O., Holmes, A., Rugg, M.D., Turner, R. Event-Related fMRI: Characterizing Differential Responses. NeuroImage 7:30-40 (1998)

Garavan, H., Ross, T. J., Stein, E. A. Right hemispheric dominance of inhibitory control: An event-related functional MRI study. Proc. Natl. Acad. Sci. USA (1999) 96:8301-8306

Henson, R.N.A., Price, C.J., Rugg, M.D., Turner, R., Friston, K.J. Detecting Latency Differences in Event-Related BOLD Responses: Application to Words versus Nonwords and Initial versus Repeated Face Presentations. NeuroImage 15:83-97 (2002)

Josephs, O., Henson, R.N.A. Event-related functional magnetic resonance imaging: modelling, inference and optimization. Phil. Trans. R. Soc. Lond. B 354:1215-1228 (1999)

Josephs, O., Turner, R., Friston, K.J. Event-Related fMRI. Human Brain Mapping 5:243-248 (1997)

Samuel, M., Williams, S.C.R., Leigh, P.N., Simmons, A., Chakraborti, S., Andrew C.M., Friston, K.J., Goldstein, L.H., Brooks, D.J. Exploring the temporal nature of hemodynamic responses of cortical motor areas using functional MRI. Neurology 1998;51:1567-1575

Chapter 5

Statistical Parametric Mapping

5.1 Introduction

Statistical parametric mapping is the statistical approach used by the industry-standard, data processing package, SPM99. Since this package is the industry standard, it was used to pre-process and analyze the experimental data gathered in this thesis. The underlying mathematics and statistical theory inherent to this program are quite complicated; therefore, it is not the intent of this thesis to explain either the math involved, nor the underlying theory. Instead, an overview is presented, summarizing each of the analysis steps. This discussion is important since using SPM is not a trivial matter, despite it being a pre-packaged product. In order to make full use of this package, one must understand what each of the offered options does, in order to select the most appropriate parameters or modeling elements when a selection is offered.

This chapter begins with an overview of SPM99 operation. Subsequently, each step used in the pre-processing of the data is explained, including realignment, normalization and smoothing (figure 5-1). Next, the general linear model is introduced, which is the basis for SPM99 statistical analysis. The multiple comparisons problem is defined, and the different types of p-values used for reporting results are differentiated. Finally, the chapter examines the different approaches available for multi-subject or group analysis, and ends by detailing the process of anatomically labelling statistically significant clusters. The material presented herein was gathered from several sources, the principal two, should the reader want additional details, are the book Human Brain Function by Frackowiak et al. and the SPM99 online manual http://www.fil.ion.ucl.ac.uk/spm/course/manual/man.htm

5.2 Defining SPM

Statistical Parametric Mapping creates statistical image processes that test hypotheses concerning regional activation. The maps themselves are images (of the brain) whose voxel values are spread according to a known probability density function, usually Gaussian, under the null hypothesis. To generate these maps, each voxel is assessed using a standard one-variable statistical test. The statistical results are the SPM (statistical parametric map) voxel values. Deviations in SPM values deemed larger than due by chance are treated as indicative of regional activation.

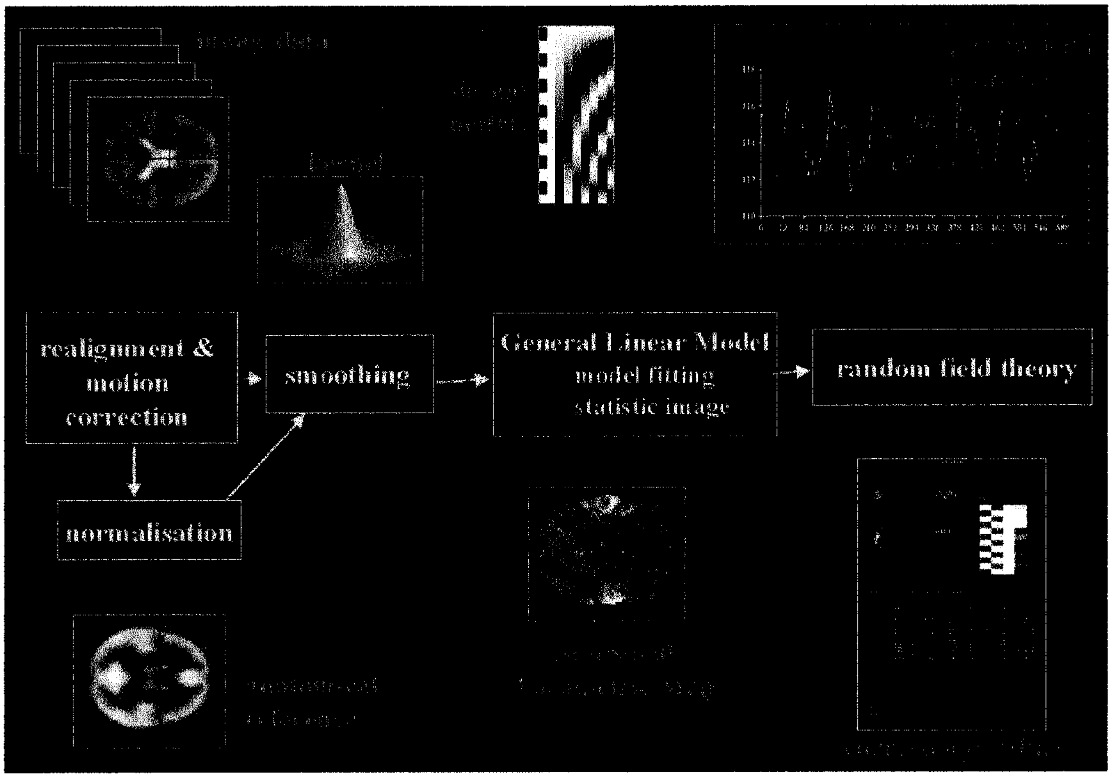

Figure 5-1. The different stages in the analysis of data using SPM99.
(http://www.fil.ion.ucl.ac.uk/spm/course/notes02/intro/img3.htm)

5.3 Overview

The mathematical model defined by the researcher to analyse the observed data is called the design matrix. It consists of columns of data which can be explanatory variables or confounds – examples of the former include factors such as whether on or off medication or paradigm task definition while the latter can include such things as subject motion parameters. The significance of a particular column in explaining the observed data is determined by using the general linear model and standard least squares. These contribution estimates are called parameter estimates. By specifying linear combinations of parameter estimates (called contrasts) one can test for specific regional effects. At each voxel the statistical significance of a contrast is determined by calculating its t-statistic – i.e. a statistic which in the null hypothesis has Student's t distribution. The SPM{t} map as it is now known, is converted into an SPM{Z} map; this allows use of distributional approximations of Gaussian field theory to characterize activation blobs in terms of maximum value and spatial extent. The final result is a p-value at each voxel specifying the "probability of obtaining a t-ratio as extreme or more extreme than the t-statistic on its evidence against the null hypothesis, if the null hypothesis is correct (Ramsey p.41)." The smaller the value, the more likely the hypothesis is incorrect. Thus if the hypothesis is no activation, the smaller the p-value the more likely that activation did occur in a given voxel.

5.4 Implementation: Pre-processing

5.4.1 Spatial Realignment and Normalization Overview

The purpose of the normalization and realignment steps is to remove artifactual variance from the voxel time-series data – variance induced by brain shape and movement-related causes respectively. SPM uses a voxel-based analysis consequently data must come from the same brain parcel - both over the course of the experiment and across subjects in multi-subject comparisons. If this is not the case artifactual variance results which can lead to false activations, corrupt true activations, etc.

5.4.2 Spatial Realignment

Realignment is a two-step procedure in which movement-related confounds are removed from the data. First, using a least squares analysis, movement is estimated between a given scan and the 1st scan acquired resulting in a 6 parameter rigid body affine transformation$_1$. Using this transformation the data are resampled using either trilinear, sinc or cubic spline interpolation.

A second step is required in fMRI to accommodate for effects remaining from the above linear affine model. These include spin excitation history (particularly if TR ~ T_1), movement between slice acquisition and interpolation artifact effects. Under the influence of these effects the current signal becomes a non-linear function of movement in previous scans. SPM represents this non-linear function as a 2nd order polynomial moving average-autoregression model then uses the observed data and estimated affine parameters to estimate the non-linear function's parameters. Once the signal is estimated it is subtracted from the original data.

5.4.3 Normalization

While spatial realignment removes movement variance from data, normalization removes subject-specific shape differences. Normalization warps the images of the brain, matching them to a standardized template$_2$. The purpose is two-fold: warped brains are suitable for inter-subject averaging since data from different subjects come from identical regions of the brain, and results can be reported using a common frame of reference amongst investigators.

5.4.4 Smoothing

Smoothing is an averaging process: smoothing creates a new value for each data point based on its original value and those of its neighbours. In SPM it is implemented as 3D convolution with a Gaussian kernel. The reasons for smoothing are as follows:

1) Smoothing increases signal to noise. This is explained by the matched filter theorem which states that the optimum signal to noise will be obtained if the filter size corresponds to the extent of the signal of interest. In fMRI this dictates choosing the FWHM of the Gaussian kernel (smoothing filter) to correspond to the spatial extent of the hemodynamic response (several mm)$_3$.

2) Smoothing molds the data such that they better fit the Gaussian field model – an essential requirement given that the theory of Gaussian fields is the basis of the regionally specific inference approach used by SPM.

3) Inter-subject averaging necessitates smoothing. Smoothing ensures that a large enough spatial scale is used such that functional projection onto anatomy is not confounded by individuals' microscopic brain structure or organization details. In other words, following normalization, microscopic anatomical differences still exist between subjects. In order to analyse activations common to subjects, and from the same voxel, a large enough scale must be used such that homologies exist.

The extent of smoothing used in each of the Parkinson's studies was determined through separate pilot studies. One of these is included for interest in Appendix E.

5.5 Implementation: Results

Having pre-processed that data in preparation for statistical analysis, subsequent work will examine each and every voxel for evidence contradicting the null hypothesis of no experimental effect. The process culminates with the generation of a generic brain in which each voxel is a statistical value against the null hypothesis.

5.5.1 The General Linear Model (GLM)

The general linear model applied to fMRI, equates the observed response to a linear combination of explanatory variables and a residual error. Mathematically it appears as follows:

$$y_{ij} = x_{i1}\beta_{1j} + x_{i2}\beta_{2j} + \ldots x_{ik}\beta_{kj} + e_{ij}. \quad (1)$$

where y_{ij} = the observed signal intensity of voxel j during the ith scan
e_{ij} = error term

x_{ik} = user-specified explanatory variable

β_{kj} = parameter estimates characterizing the weighting of an explanatory variable's effect in explaining variations in y

In matrix form this appears as

$$\begin{pmatrix} Y_1 \\ \cdot \\ \cdot \\ Y_j \end{pmatrix} = \begin{pmatrix} x_{11} \ldots x_{1L} \\ \cdot \\ \cdot \\ x_{j1} \ldots x_{jL} \end{pmatrix} \begin{pmatrix} \beta_1 \\ \cdot \\ \cdot \\ \beta_L \end{pmatrix} + \begin{pmatrix} \varepsilon_1 \\ \cdot \\ \cdot \\ \varepsilon_L \end{pmatrix}$$

or

$$Y = X\beta + e. \quad (2)$$

The X matrix is called the design matrix. Each row represents a different scan and columns consist of explanatory variables. Explanatory variables may be continuous or discrete, covariates (e.g. global CBF) or levels of a factor (e.g. subject), and effects of interest or confounds. Confounds are additional explanatory variables, not of interest, that may affect the contribution of interesting effects.

SPM creates design matrix images that depict the specified model (figure 5-2). The greyscale used assigns –1 to black, 0 to grey, 1 to white. Covariates are scaled and fall in the range of [0,1].

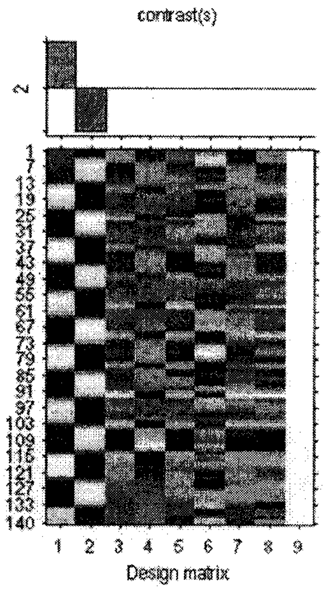

Figure 5-2. Design Matrix for the Scholz study (Chapter 7). Each row represents a separate scan or observation. The first two columns specify the stimulus presentation with column 1 representing the "on" pattern of finger tapping and toe wiggling over the experiment, while column 2 represents the "off" or resting pattern. The next 6 columns are confounds – depicting subject motion (3 translation, 3 rotation). The final column adds a constant term absent in equation (2). This is equivalent to the y-intercept (μ) in a single observation equation: $Y_j = \mu + x_{1j}\beta_1 + e_j$.

5.5.1.1 Contrasts

A user-specified vector of weights concerning differences in parameter estimates (a contrast vector) allows one to examine regionally specific effects such as locations in which an activation effect exists.

5.5.2 Choosing a Statistical Threshold – A Multiple Comparisons Problem

The statistical analysis process culminates with the creation of a statistic for each voxel. At a single voxel level one can impose a threshold on that value such that if the test statistic exceeds the threshold, then the null hypothesis is rejected. The situation changes however, when considering thousands of voxels as opposed to just one (the multiple comparisons problem). Supposing that the null hypothesis is correct– that no activation occurs between rest and active states – then the stats over the entire brain volume will follow a random normal distribution$_4$ (specifically referring to Z statistics$_5$). Thus even in the absence of true activation, one expects many voxels to "appear" active (known as false positives). For example, for a single slice image containing 16384 voxels (128^2), and with a specified threshold of $p<0.05$, simple random distribution will make some 819 voxels "appear" active. The multiple comparisons problem deals with setting an appropriate threshold such that the surviving voxels' z-scores are too high to have occurred by chance.

FMRI data is spatially correlated complicating the choice in statistical correction method. Bonferroni correction is deemed too conservative in that it assumes voxel independence and not spatial correlation. The spatial correlation in fMRI arises due to both the point spread function in imaging which incidentally captures some of the surrounding tissue signal within a voxel's data and the smoothing process that correlates the signal of neighbouring voxels.

The method used by SPM to select an appropriate threshold in the context of spatial correlation is Random Field Theory. In simplest terms, RFT has 3 stages: resel count, Euler characteristic appraisal and finally threshold evaluation to obtain a particular false positive rate.

A resel (resolution element) is a pixel group the size of the image smoothness FWHM. Thus if an image is smoothed to 8x8 pixels, a resel is 8x8 pixels. So that if before smoothing an image was 128*128, and smoothing was 8*8, then the number of resels = (128/8)*(128/8) = 256.

In simplest terms, the Euler Characteristic (EC) is the number of activation blobs image that survive a certain threshold. Thus if a threshold were chosen, and two voxel clusters in the image met this threshold, then EC = 2. The Characteristic need not be counted but rather can be estimated for a given z-score threshold using the resel count and information about the shape of the region studied. Furthermore, at high Z thresholds, this EC estimate turns out to be a good indicator of the likelihood of obtaining one or more blobs at that threshold. The implications will be shown in the following example. Suppose that for a Z threshold and resel count, the EC = 0.05. One may therefore say that the probability of obtaining 1 or more blobs meeting the threshold is 0.05. More importantly this also may be interpreted as a 0.05 or less probability that any blobs that survive the threshold have occurred by chance.

5.5.2.1 Uncorrected, Corrected and Small Volume Corrected (SVC) P-values

The choice of which p-value to use is predicated by the localization of the signal by previous findings. Uncorrected p-values (those not corrected for the multiple comparisons problem) are valid only when an *a priori* hypothesis isolates the effects to a precise voxel location. If such an anatomic restriction is not possible, i.e. the null hypothesis is instead that no effects exist <u>anywhere</u> in the brain, then a corrected p-value must be used.

If, rather than a pixel, one has an *a priori* hypothesis about a <u>region</u> of expected activation, then small volume correction is appropriate. Under these circumstances correcting for multiple comparisons across the entire brain is both too severe and unwarranted since you have limited your study to a particular portion of the brain.

5.5.3 Group Analysis

In SPM there are 2 general models used in the analysis of group data: fixed effects (FFX) and random effects (RFX). Model choice is predicated upon the statistical power of the data in a study, and the level of inference to which results will be extended.

5.5.3.1 Random Effects

RFX and FFX models account for different sources of variability thereby determining the sphere of influence. RFX acknowledges that subjects come from a larger population and hence allows for some variability in the observed subject effects. Alternately, random effects doesn't require that each and every subject activate a voxel, instead a sufficient number of subjects within a sample must activate it. In the implementation of RFX models, the restriction of 1 image per contrast per subject removes intra-subject variance leaving strictly inter-subject variance as the source of image-to-image variability thereby permitting a broad level of inference.

Using random effects, one can extend group observations and conclusions to the entire population from which subjects were sampled. However, the degrees of freedom, which relate to statistical power, are limited to the number of subjects in the study. Therefore the price for this level of inference is that this method also requires the most subjects in order for effects to reach significance. For example some SPM experts suggest at least 10-12 subjects per group[6] while others say that even 10 is insufficient[7].

5.5.3.2 Fixed Effects

Fixed Effects treats subject-specific effects "as measured" and fixed. It is basically making inferences concerning the outcome if the same subjects were scanned repeatedly.

Fixed Effects conclusions pertain only to the specific group of subjects/patients studied and cannot be extended to the population as a whole. It is akin to taking the average of voxel values within a group.

Another drawback is that fixed effects group analysis doesn't correctly estimate either the degrees of freedom (dofs) or the variance. Group analysis should only combine across-subject variance, yet with FFX it includes within-subject variance. Furthermore, the dofs are determined by the number of scans and thus outrageously large values like 700 are possible. As a practical note, this means that if random effects analysis does not yield statistically significant effects, one may turn to fixed effects provided that the inferences are limited accordingly. For example one could state that the results may not be true of brain functions in general or instead that a certain proportion of the subjects displayed a certain response (e.g. 7 of 10 patients activated a particular region). Alternately, one could apply a conjunction to the FFX model.

5.5.4 Anatomically Labelling Active Clusters

Once SPM99's statistical analysis has concluded, the active clusters are presented both pictorially as maximum intensity projections (MIPs) or "glass brains", and in tabular form (figure 5-3). The MIPs display the clusters' location within the standardised template brain with the exact coordinates listed in the ensuing table. SPM however, does not label these locations anatomically.

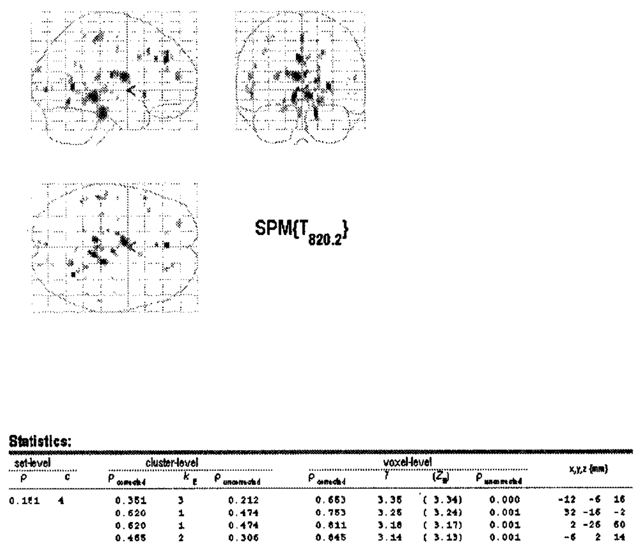

Statistics:

set-level		cluster-level			voxel-level				x,y,z {mm}
p	c	$p_{corrected}$	k_E	$p_{uncorrected}$	$p_{corrected}$	T	$(Z_\equiv)$	$p_{uncorrected}$	
0.181	4	0.351	3	0.212	0.663	3.35	(3.34)	0.000	-12 -6 16
		0.620	1	0.474	0.753	3.25	(3.24)	0.001	32 -16 -2
		0.620	1	0.474	0.611	3.18	(3.17)	0.001	2 -26 60
		0.465	2	0.306	0.645	3.14	(3.13)	0.001	-6 2 14

Figure 5-3 Output from Statistical Analysis Using SPM99

Applying anatomical labels is a several stage process wherein data is transferred from SPM into a separate program, the Talairach Daemon, for anatomical classification. This tedious series of steps, necessary for each contrast in each experiment, was minimized by a programming solution proposed within this thesis (see Appendix D).

5.6 Conclusion

This chapter has summarized the statistical analysis of SPM99 from data pre-processing through to MIP generation and anatomic labelling of clusters. With this background the reader is now prepared for Chapters 7 and 9 (detailing functional experiments at 1.5T and 4.7T respectively), which refer to the concepts and steps described in this chapter.

5.7 Endnotes

1. By using the spatial derivatives of the images, a 1st order Taylor approximation of the signal intensity change due to movement is calculated leading to estimation of the affine transformation.

2. SPM uses the International Brain Mapping Consortium 152 (ICBM152) template from the Montreal Neurological Institute. Software programs exist to convert coordinates from this to the atlas of Talairach and Tournoux if necessary.

3. An alternate explanation is that the spatial frequency of the noise is much higher than that of the hrf. The smoothing process is a filtering that quells the high frequency noise and amplifies the low frequency hrf signal.

4. Strictly speaking this is true only at high degrees of freedom

5. The above discussion applies principally to SPM 96 although generally to both SPM 96 and 99. The advancement of SPM 99 was to use t-stats in generating thresholds in the RFT approach. Using t-stats led to more accurate thresholds as Z-scores resulted in too many false positives at low dof.

6. Geraint Rees (n=10-12) Item #2770 (9 Feb 2000 11:11) - Re: Basics in group statistics (SPM email list)

7. Will Penny (at least 12 per group) Item #5875 (30 Mar 2001 13:36) - Re: Asking quistion

   Richard Perry (n>12) Item #5170 (10 Jan 2001 11:16) - Re: use of conjunctions - expert comments please

   Daniel Weissman (n>24) Item #12403 (29 May 2003 17:35) - Re: RFX with Multiple Conditions, Subjects, and Groups

   (all from SPM email list)

5.8 References

Frackowiak, R.S.J., Friston, K.J., Frith, C.D., Dolan, R.J., Mazziotta, J.C. Human Brain Function. San Diego: Academic Press, 1997.

Ramsey, F.L., Schafer, D.W. The Statistical Sleuth A Course in Methods of Data Analysis. Wadsworth Publishing Company 1997

http://www.fil.ion.ucl.ac.uk/spm/course/manual/spatial.htm

http://www.fil.ion.ucl.ac.uk/spm/course/manual/model.htm

http://www.fil.ion.ucl.ac.uk/spm/course/manual/man.htm

http://www.fil.ion.ucl.ac.uk/spm/papers/SPM-Chapter.pdf

http://www.mrc-cbu.cam.ac.uk/Imaging/

http://www.jiscmail.ac.uk/lists/spm.html (SPM Email Database)

Chapter 6

Parkinson's Disease

6.1 Introduction

This thesis investigates the behaviour of the basal ganglia (BG) in Parkinson's patients, using functional MRI. However, before discussing the experiments that were conducted, it is important to summarize the disease itself, so that the reader understands a) why the basal ganglia activation may be abnormal in Parkinson's' patients b) how the BG affect functional operation in cortical areas c) the symptoms of the disease which lead to abnormally large subject motion during functional scanning and which also impair patients' motor task performance and d) the morphology of the BG and where the constituent nuclei are located. The material presented here was summarized from the documents listed in the references section.

6.2 Overview

Parkinson's Disease (PD) is a chronic, progressive neurodegenerative disease. Most patients are between the ages of 50 and 65 and incidence increases with age. In Canada, about 80-100,000 people have Parkinson's. While not fatal, the disorder is life altering. Patients' symptoms include resting tremor, rigidity and slowness initiating movement. No cure has yet been discovered; therefore, current treatments simply attempt to control the symptoms.

The movement disorder originates from the death of nerve cells called neurons in the substantia nigra of the basal ganglia. These neurons produce a chemical messenger, the neurotransmitter dopamine, which allows for neural signals to be passed from neuron to neuron and from neurons to muscles. The degeneration of dopaminergic neurons creates a dopamine deficiency that disrupts chemical signalling in the brain and ultimately affects body movements. By the time of diagnosis, about 80% of these neurons have died.

6.3 Cause

Parkinson's patients are subdivided into two classes according to epidemiology. The term Parkinson's typically refers to the most common type - idiopathic or primary Parkinson's. The cause of the dopaminergic neuron death in the substantia nigra is unknown. Possible factors being researched include family medical history, environmental agents, and viruses. In the less common Secondary Parkinsonism, patients have Parkinson's symptoms but the cause is known - either trauma, infection, tumour, toxic chemicals, illegal drugs or certain medications.

6.4 Symptoms

The illness is characterized by the following symptoms:

6.4.1 Principal Symptoms

- Resting tremor of the hand, arm or leg
    - Not present during sleep and decreases with voluntary movements
    - Initially affects one side of the body but spreads to both over time

- Rigidity (muscle stiffness when at rest)
    - Hinders movement
    - Leads to muscle pain and fatigue
    - In facial muscles causes hypomimia (reduced facial expression)

- Bradykinesia
    - Slowness in movement and difficulty initiating or finishing a movement
    - Includes clumsiness in fine movements

- Postural Instability
    - Impaired balance reflexes make patients' gait and posture resemble inebriation
    - Limits movements, risk of falling

6.4.2 Some Secondary Symptoms

- Hypophonia (soft-voiced speaking)
- Micrographia (small, cramped handwriting)
- Depression (in reaction to disease or due to biochemical imbalance)
- Dysphagia (swallowing problems)
- Fatigue
- Even dementia (global deterioration in intellectual function or permanent impairment of mental functions and memory)

6.4.3 Symptom Severity Rating

The most common scale is the Hoehn and Yahr 5 stage scale which quantifies disease progression. Stage 1 is defined by slight unilateral tremor or rigidity, with or without bradykinesia. Stage 2 is moderate tremor or rigidity, bilaterally, as well as bradykinesia. Finally by Stage 5 a patient is restricted to a wheelchair or bed and has severe postural instability.

6.5 Treatments

There is no cure for Parkinson's disease. Treatments attempt to control the symptoms such as rigidity and resting tremor. Given that Parkinson's is caused by a dopamine deficiency, drug treatment of the disease focuses on restoring dopamine's action. The most common drug used is Levodopa. Levodopa is a precursor to dopamine that is converted into dopamine in the brain thus restoring its levels there. There are also other drug treatments including dopaminomimetics, which as the name suggests, behave like dopamine by directly stimulating dopamine receptors in the brain (figure 6-1).

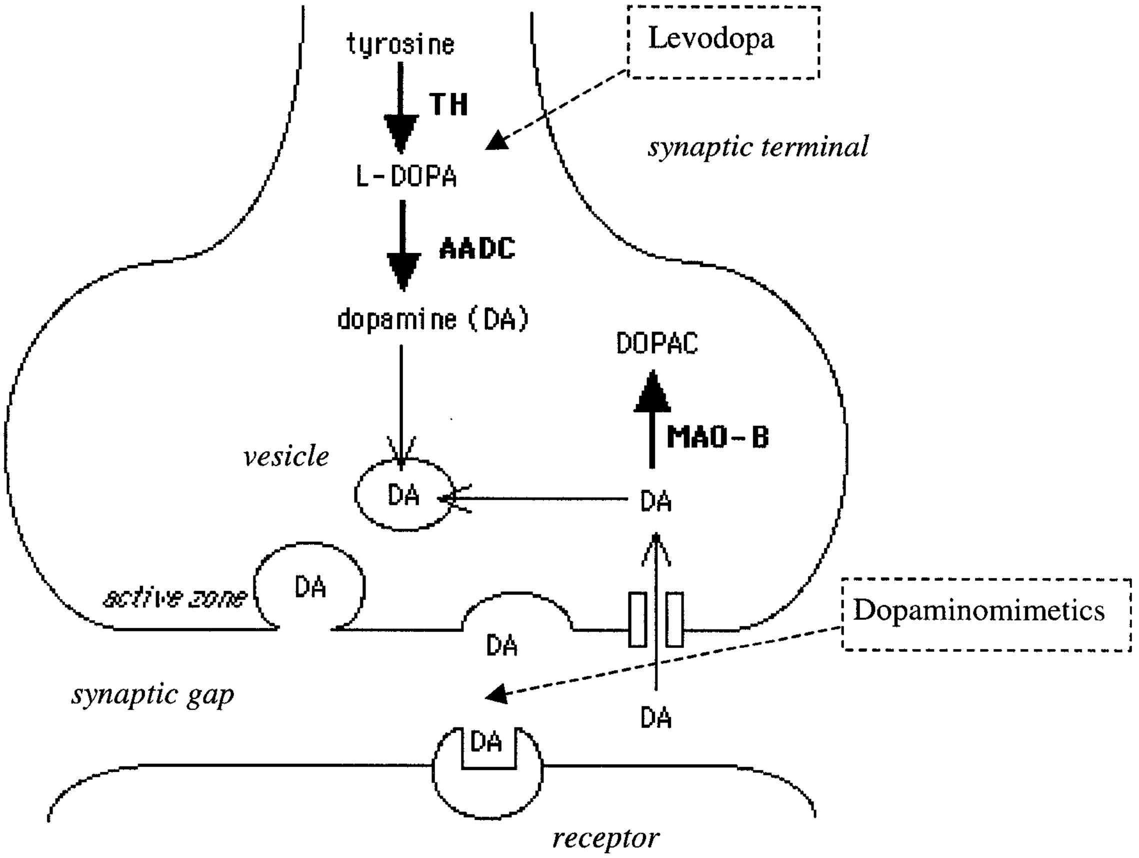

Figure 6-1 The dopamine cycle in synaptic transmission.

Dopamine is created in the following metabolic chain. Tyrosine, in combination with the action of the tyrosine hydroxilase (TH) enzyme is transformed into L-DOPA, which itself is changed into dopamine by the aromatic amino acid decarboxylase (AADC) enzyme. Dopamine is then collected into a vesicle and prepared for release for chemical synaptic transmission. After delivery into the synaptic gap, unused dopamine is re-absorbed back into the terminal. Two drug treatments are Levodopa and dopaminomimetics: Levodopa is added in place of L-DOPA to boost dopamine levels while dopaminomimetics act in place of dopamine to directly stimulate post-synaptic receptors (Reference 1).

6.6 Morphology

The basal ganglia consist of several interconnected nuclei: the globus pallidus - internal and external (GPi, Gpe), the subthalamic nucleus (STN), the substantia nigra – par compacta (SNc) and reticulata (SNr) and the striatum (caudate nucleus and putamen) (figures 6-2, 6-3). These nuclei connect to the cortex by direct and indirect pathways using a variety of neurotransmitters including GABA, substance P, dopamine etc.

image adapted from Nauta & Feirtag (1986)

STRIATUM & GLOBUS PALLIDUS

Figure 6-2. Sections of the basal ganglia (reference 6)
This image is a coronal slice of the brain showing the location of the striatum (dark) and the globus pallidus (GP) (light). The striatum consists of both the putamen (lower section) and the caudate nucleus (upper section). Likewise, the GP is divided into two segments: the globus pallidus external (nearest to the striatum) and the globus pallidus internal.

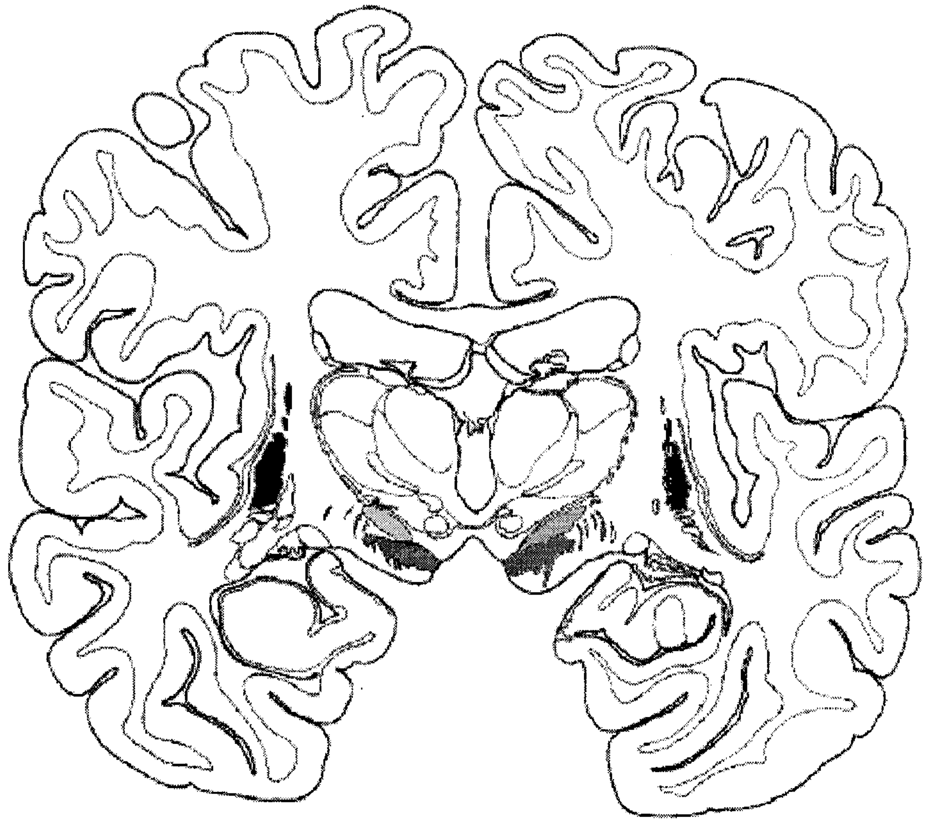

image adapted from Nauta & Feirtag (1986)

SUBTHALAMIC NUCLEUS & SUBSTANTIA NIGRA

Figure 6-3. Additional regions of the basal ganglia (reference 6)
This coronal slice shows the anatomical location of additional nuclei within the BG: the subthalamic nucleus (light gray) and the substantia nigra (mid gray). The putamen also appears in this slice (black).

Degeneration of dopaminergic neurons in the substantia nigra results in a dopamine deficiency. This leads to over-stimulation of the thalamus, subsequent under-stimulation of the frontal cortex, and ultimately the appearance of Parkinson's symptoms (figure 6-4).

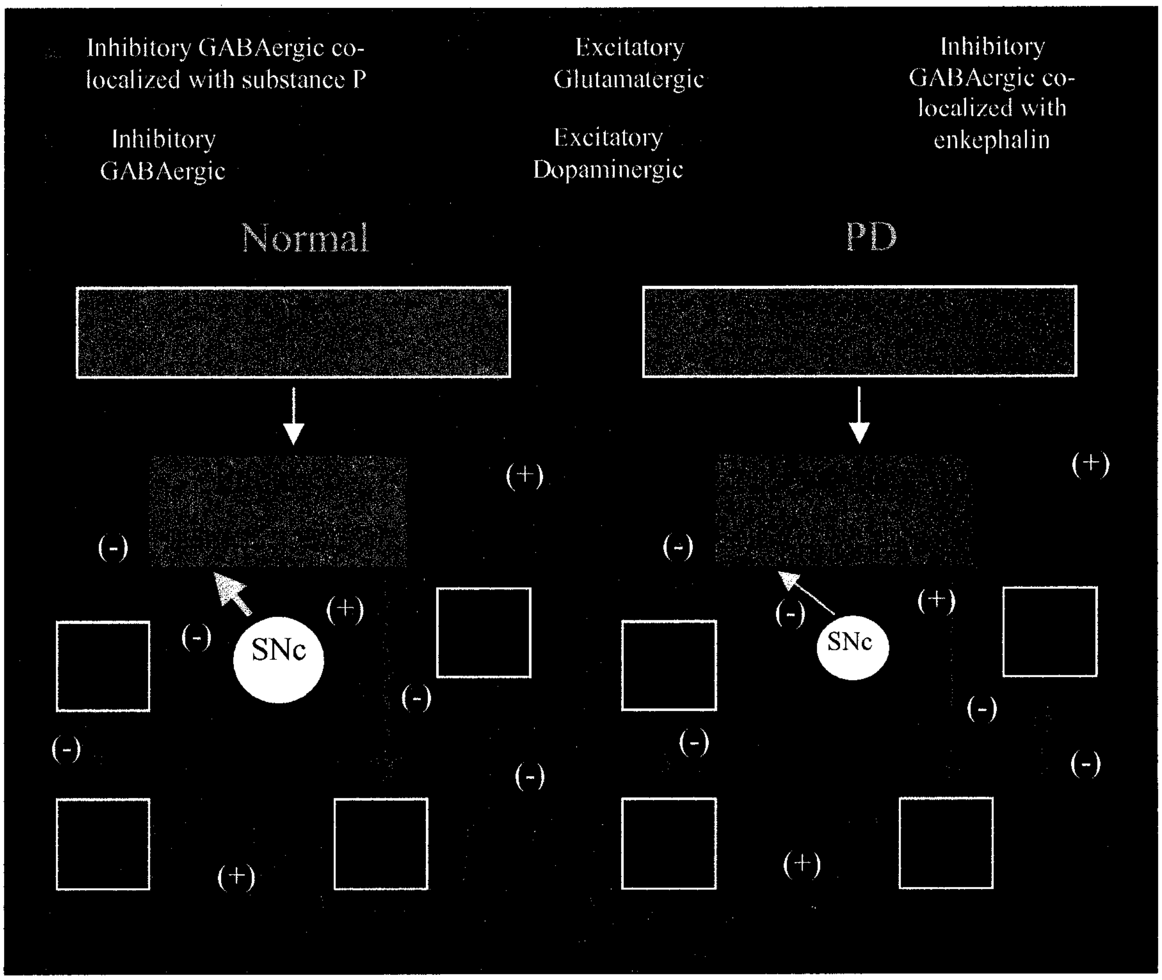

Figure 6-4. A comparison of the indirect and direct neural pathways in the Basal Ganglia between the Normal and Parkinsonian Brain (Alexander and Crutcher 1990). (The thickness of the arrows indicates the strength of the signal. Additionally, inhibitory signals are represented by warm colors and minuses while excitatory are green and have pluses)

6.6.1 Sample explanation – Comparison of the PD and Normal <u>Direct</u> Pathways

Within the substantia nigra pars compacta (SNc) of the PD brain, dopaminergic neurons have degenerated. As a result, the excitatory dopaminergic signal of the direct pathway to the putamen is weaker in the PD vs. the Normal brain. The PD putamen, being less excited, emits a weaker output signal – in this case a weaker inhibitory GABAergic co-localized with Substance P. Weaker PD inhibition on the GPi, allows for the PD GPi to emit more signal then normal, thus it sends out a stronger than normal inhibitory GABAergic signal to the thalamus (VL = ventral lateral thalamus). The over-inhibited thalamus in Parkinson's patients can only generate a weak output, in this case a weak excitation of the cortex. This results in Parkinson's symptoms.

6.7 Conclusion

Parkinson's symptoms arise from the degeneration of dopaminergic neurons in one nucleus of the basal ganglia – the substantia nigra. Since the basal ganglia send signals to the cortex, the resultant dopamine deficiency affects cortical operations, which leads to the appearance of symptoms such as resting tremor and bradykinesia. Bradykinesia may lead to slower motor responses during task execution compared to healthy controls, while resting tremor may cause significant patient head motion despite the use of physical restraints, leading to false activations.

While degeneration has been localized to the basal ganglia, their functional abnormality in Parkinson's disease has not been exhaustively investigated. Hence, it is of interest to examine the activation patterns of the other nuclei in the basal ganglia in Parkinson's patients in order to ascertain how they compensate for, or more generally, how they are affected by the dopamine deficiency.

6.8 References

1. http://tcw2.ppsw.rug.nl/~vdbosch/pd.html (The Dopamine Theory of Parkinson's Disease (a compilation of several authors' works)
2. Helping Parkinsonians. A Guide for the Health Care Team. The Parkinson Foundation of Canada 1996
3. Taking Charge: A Guide to Living with Parkinsonism. Calne, Susan, Baisely, Kerry, Coughlan Paula, Hurwitz, Trevor, Shaw, Carole, Traviss, Karol. 2001
4. An Introduction to Living Well with Parkinsonism: What You and Your Family Need to Know. Calne, Susan, Shaw, Carole 1999.
5. Alexander GE, Crutcher, MD. Functional architecture of basal ganglia circuits; neuronal substrates of parallel processing. Trends Neurosci 1990; 13: 266-71
6. http://anc.ed.ac.uk/~anaru/research/anatomy/

Chapter 7

Parkinson's Experiments

7.1 Introduction

This chapter is composed of two separate studies comparing functional activation of Parkinson's patients to healthy, age-matched control subjects: one epoch-based functional magnetic resonance (fMRI) experiment, and one event-related fMRI experiment. The goal of the experiments was to investigate both inhibition in Parkinson's patients, and whether or not their basal ganglia showed behavioural impairment. To accomplish this, two studies showing promising results, with inhibition and basal ganglia focuses respectively, were recreated. These are referred to below as the Garavan and Scholz studies - named after the work by Garavan 1999 and Scholz 2000. The following chapter outlines both recreated experiments in detail.

7.2 Garavan Study

7.2.1 Introduction

Parkinson's disease is characterized by the neurodegeneration of dopaminergic neurons within the substantia nigra par compacta of the basal ganglia. Parkinson's symptoms include slowness of and difficulty initiating movements, resting tremor, rigidity, postural instability etc. Together the first three symptoms suggest a fundamental impairment between response conceptualization and the motor output – concerning either movement initiation or movement inhibition. This study attempts to shed light on the nature of this impairment through the use of a response inhibition or Go/No-Go experiment.

There is good precedent for using a Go/No-Go task in the investigation of Parkinson's disease. Cunnington et al. (2001) showed shift in contingent negative variation (CNV) frontally and laterally ipsilateral to the side of greatest basal ganglia impairment in hemi-Parkinson's patients, during the movement preparation stage of a Go/No-Go task. In another study of response inhibition, variations in response probability yield abnormal force patterns in Parkinson's patients compared to controls (Franz and Miller 2002). Furthermore, patients displayed difficulty with inhibition; compared to controls, in No-Go trials they had both larger mean force suggesting incomplete inhibition and a longer period of force application suggesting force termination difficulties. Together these studies differentiate Parkinson's from control subjects, although behaviourally (through measurement of finger pressing force) in one instance, and at low spatial resolution and only during the preparation phase in the other. The next logical step is therefore to use functional magnetic resonance imaging (fMRI) in the study of Parkinsonian response inhibition.

To date, few studies have used fMRI to study functional activation in Parkinson's patients. Haslinger et al. (2001) analyzed the levodopa-induced, activation modifications in the Parkinsonian brain using event-related fMRI (efMRI). Subjects were studied before and after levodopa applications, when moving a joystick in a freely-selected direction in response to a random-interval audio cue. Mattay (2002) compared the modulatory effects of dopamine in Parkinson's patients during both a working memory and a motor task. Sabatini et al. (2000) used a complex right hand movement task to compare activity in dopamine-deplete Parkinson's subjects compared to controls. Rowe et al. (2002) investigated the effects of attention to action on effective connectivity between cortical areas during a sequential finger-tapping task. Given the scarcity of Parkinson's fMRI research, it is not surprising that no apparent attempt has yet been made to use fMRI in the study of response inhibition in Parkinson's patients.

Although fMRI has not been used to examine inhibition in Parkinson's patients, several fMRI studies have investigated inhibition in healthy controls leading to the existence of several different experimental designs. The response inhibition task in this study was designed such that Go response was more predominant than the No-Go response. Several investigators have debated the issue of Go prepotency: one side has argued that it is necessary in order to make the inhibition difficult and an actual suppression (Garavan 1999) while others suggest that prepotency lends itself to the oddball effect and thus activation interpreted as inhibition may in fact be due to activation associated with the processing of a rare or unusual stimulus (Liddle 2001). Proponents of the latter view have suggested that equal numbers of Go and No-Go stimuli be presented, with increased inhibition difficulty instead generated by some other means, for example, a heightened readiness could be created by using a count-down preceding each stimulus (Liddle 2001). It has also been pointed out that the working memory demands of Garavan task potentially stand to confound interpretation of inhibition activation (Liddle 2001). Balancing these opinions, it was decided to use a modification of the Garavan experiment wherein the ratio of the Go to No-Go stimulus was reduced, lessening the oddball effect, while still maintaining the Go predominance which seems a better method for eliciting a suppressed response as opposed to having "no response" simply being one of the response choices.

7.2.2 Materials and Methods

7.2.2.1 Subjects

Six Parkinson's patients (4 males, 2 females, mean age 65±8 years), off medication for ~12 hours, and seven age-matched controls (4 males, 3 females, mean age 56±5 years) participated in the study. Only mildly affected (Stage 1 and 2 Hoehn and Yahr) Parkinson's patients were included, as in the drug-deplete state, these patients are the most comfortable, have the least tremor (and resultant head motion), and are typically able to complete the task. All subjects were right-handed as ascertained through simple inquiry. To conduct the required movements, patients were instructed to use their less-affected hand[1] while controls used their right (dominant) hand. All subjects provided informed written consent concerning their participation in the experiment.

7.2.2.2 Imaging

Functional images were collected using a Siemens Sonata 1.5T scanner. A single-shot, multislice, motion-corrected (Prospective Acquisition CorrEction or PACE) EPI sequence captured 16 descending slices, each 7mm thick and separated by 1mm. Patient head movement effects were minimized in two ways: physical restraints were placed over the headphones to limit subject motion and the PACE sequence (Thesen 2000) prospectively corrected for motion by real-time adjustment of slice position and orientation. The repetition rate (TR) and echo time (TE) were 2000 and 50ms respectively. Images were 220x220mm FOV with 128x128 pixels, and were acquired using a 90° flip angle and 208kHz bandwidth (1628Hz/pixel). The experiment lasted 8 minutes and 32 seconds during which 256 volumes were collected. The first 8 volumes were omitted to accommodate for signal saturation effects.

7.2.2.3 Experimental Design

The Go/No-Go paradigm is best implemented by an event-related and not a block design experiment because it allows for random stimulus timing and ordering minimizing predictability, boredom and habituation and it allows post-hoc classification of responses in the event that the subject makes a mistake.

Subjects viewed single letters of the alphabet presented in rapid succession. An LCD projector shone the images onto a screen – observed by the subject through the use of a set of mirrors mounted onto the head coil. Each image consisted of a black letter (font size 255) on a white background and lasted 500ms. Subjects were instructed to press a hand-held button whenever the letters X or Y were observed and to ignore all other letters. An additional stipulation was that the X and Y must alternate. If either letter was repeated, despite being separated by non-X or Y letters, then its second occurrence was to be ignored (Figure 7-1). In this experiment the alternating X's and Y's act as Go stimuli or Targets, the repeated X and Y stimuli as No-Go stimuli or Lures, and all other letters are ignored and establish a baseline condition.

The paradigm began with a 12 second pause to allow for magnetic saturation effects while the subject viewed a fixation point. The experiment consisted of 1000 letters and lasted 8:32 minutes. 104 Targets and 24 Lures were presented yielding a ratio of Go: No-Go stimuli of about 4:1. The average interstimulus separation for targets was 4.3 seconds (8.6 letters) with a minimum separation of 2.5 seconds (5 letters). For lures, the average interstimulus distance was 40.6 seconds with a minimum separation of 9.5 seconds.

The stimuli were presented at staggered intervals to minimize subject anticipation and to allow for oversampling of the hemodynamic response function (Josephs et al. 1997). The combination of a 2 second whole-head acquisition time (TR = 2s) and a stimulus duration of 0.5 seconds, meant that a given stimulus coincided with the acquisition of slices within one of four slabs of the brain. The stimuli were presented in such an order that by the end of the experiment, each slab had "seen" the same number of Go or No-Go stimuli as the others. This ensured that within each slice, the hemodynamic response function (hrf) was sampled with a resolution of 0.5 seconds.

If the subject failed to respond within 1000 ms following the onset of the presentation of a Target stimulus, the response was classified as an error of omission. If the subject responded to a Lure stimulus, it was classified as an error of commission.

Subjects practiced the task under supervision in a waiting room prior to the scanning session. The practice session consisted of two runs, each 2 minutes long: the first consisted only of targets, with no lures, and acclimatized the subject to the rate of stimulus presentation without the added difficulty of the inhibited response, while the second was a sample of the actual sequence used, and required both subject response and inhibition. The practice session was extended, if necessary, until the subject was comfortable with the task and performed it error-free.

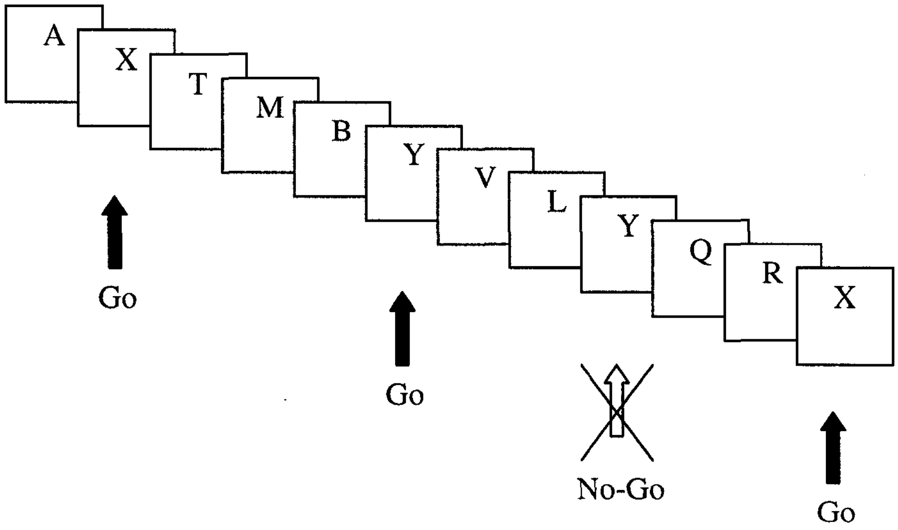

Figure 7-1. An example illustrating the paradigm used in the experiment. The subject must press a button upon seeing either an X or a Y (target) unless the previous target was the same letter, in which case the second incidence is ignored (lure). Notice that the Y's are considered to have occurred in succession despite the fact that other ignored letters (neither X nor Y) separate the two.

7.2.2.4 Data Analysis

The functional MRI data were pre-processed and analyzed using SPM99 software (Wellcome Department of Cognitive Neurology, London, UK). Images were realigned to the first volume collected. Because slices were collected in descending order, slice-timing correction was applied after realignment (Josephs and Henson 1999). Next, images were normalized to a common stereotactic space using the Montreal Neurological Institute Template, which is based on the Talairach and Tournoux system (Talairach and Tournoux 1988). Finally images were spatially smoothed with a 6mm full-width half-maximum isotropic Gaussian kernel (this was the optimal extent determined in a separate pilot study).

Stimulus classification was determined by the subjects' responses. Three types of responses were modeled: Go (subject correctly tapped after a Go stimulus), NoGo (subject correctly withheld response) and Error (either an error of commission in which the subject tapped during a NoGo, or an error of omission in which a tap was withheld following a Go stimulus).

The data were analyzed using event-related methods (Josephs 1997, Josephs and Henson 1999). With only a limited sample population size of about 7 subjects per group, and not the minimum 10-12 suggested for random effects analysis, the fixed effects model was deemed most appropriate to use. The design matrix included the following effects for each subject: three covariates outlining stimulus onsets, six motion regressors (3 rotational, 3 translational) characterizing subject movement during the scanning session and a global volume mean. Data were high-pass filtered to eliminate low frequency noise and temporally smoothed with an hrf function. Global scaling was included to account for whole brain intensity differences over time. A canonical hrf_2 + temporal derivative was used to model the response to the different stimulus types. T-tests were used to test specific hypotheses ($p<0.001$ uncorrected, with a minimum cluster size of 3 voxels).

7.2.3 Results

7.2.3.1 Behavioural Differences

The Parkinson's and control groups were compared according to the number of errors of omission (not pressing during a "Go"), the number of errors of commission (pressing during a "NoGo") and the reaction time (time from having first seen the stimulus, to the moment the button was pressed). Patients made significantly more errors of commission than control subjects (mean: 7 ± 4.8 errors (patients) vs. 2.7 ± 2.0 (control), two-sided p-value = 0.0546). However, there was no evidence of difference between the groups either in terms of the number of errors of omission (mean: 8.7 ± 2.9 (patients) vs. 10.6 ± 6.5 (control), two-sided p-value >0.5) or in reaction times (mean: 523.9 ± 39.3ms (patients) vs. 495.88 ± 47.7 ms (control), two-sided p-value = 0.2795).

7.2.3.2 Within-Group fMRI Results

The focus of the present work is response inhibition in Parkinson's patients and how it differs, if at all, from control subjects. In the context of this experiment, this means investigating responses to the NoGo stimulus. Tables 7-1 and 7-2 summarize the focal points (Talairach coordinates) of response inhibition activation in Controls and Parkinson's patients respectively.

Control subjects' most significant activation was found in the brainstem, specifically in the mid-brain and pons. Pronounced activation was also evident in the thalamus and limbic lobe, while to a lesser extent in the culmen and medial frontal gyrus.

Qualitatively, Parkinson's patients' shared some regions of activation with controls, namely the pons and culmen (although Parkinsonian culmen activation was more widespread). In contrast however, Parkinson's patients had prominent activation in the temporal and parietal lobes, particularly in the superior temporal and postcentral gyri. This group also activated the precentral gyrus and the paracentral lobule of the frontal lobe. Figures 7-2, 7-3a and b provide an example of single subject functional results.

Table 7-1. Active Clusters in Control Subjects during Response Inhibition (p<0.001, 3 voxel minimum cluster size)

Region	Side	Brodmann Area	Cluster Location		
			x	y	z
Midbrain	Right		14	-24	-16
			8	-35	-3
Thalamus	Left		-6	-3	13
			-14	-9	15
Pons	Left		-2	-30	-20
Anterior Lobe					
Culmen	Left		-10	-35	-7
Limbic Lobe					
Posterior Cingulate	Right	BA 30	18	-58	14
Parahippocampal Gyrus	Left	BA 35	-26	-22	-17
		BA 35	-18	-26	-14
Frontal Lobe					
Medial Frontal Gyrus	Left	BA 9	-2	40	27

Table 7-2. Active Clusters in Parkinson's Patients during Response Inhibition ($p<0.001$, 3 voxel minimum cluster size)

Region	Side	Brodmann Area	Cluster Location		
			x	y	z
Temporal Lobe					
Middle Temporal Gyrus	Left		-46	-3	-22
Superior Temporal Gyrus	Right	BA 41	50	-34	13
			55	4	0
	Left	BA 38	-51	9	-12
		BA 38	-50	19	-14
Parietal Lobe					
Postcentral Gyrus	Left	BA 40	-51	-26	16
		BA 40	-53	-20	18
Inferior Parietal Lobule	Left	BA 40	-61	-33	29
Anterior Lobe					
Culmen	Left		-8	-42	-21
			-30	-44	-25
	Right		6	-65	-10
Frontal Lobe					
Precentral Gyrus	Right	BA 44	59	16	7
Paracentral Lobule	Left	BA 6	-6	-32	61
Pons	Left		-18	-35	-30
	Right		10	-40	-27

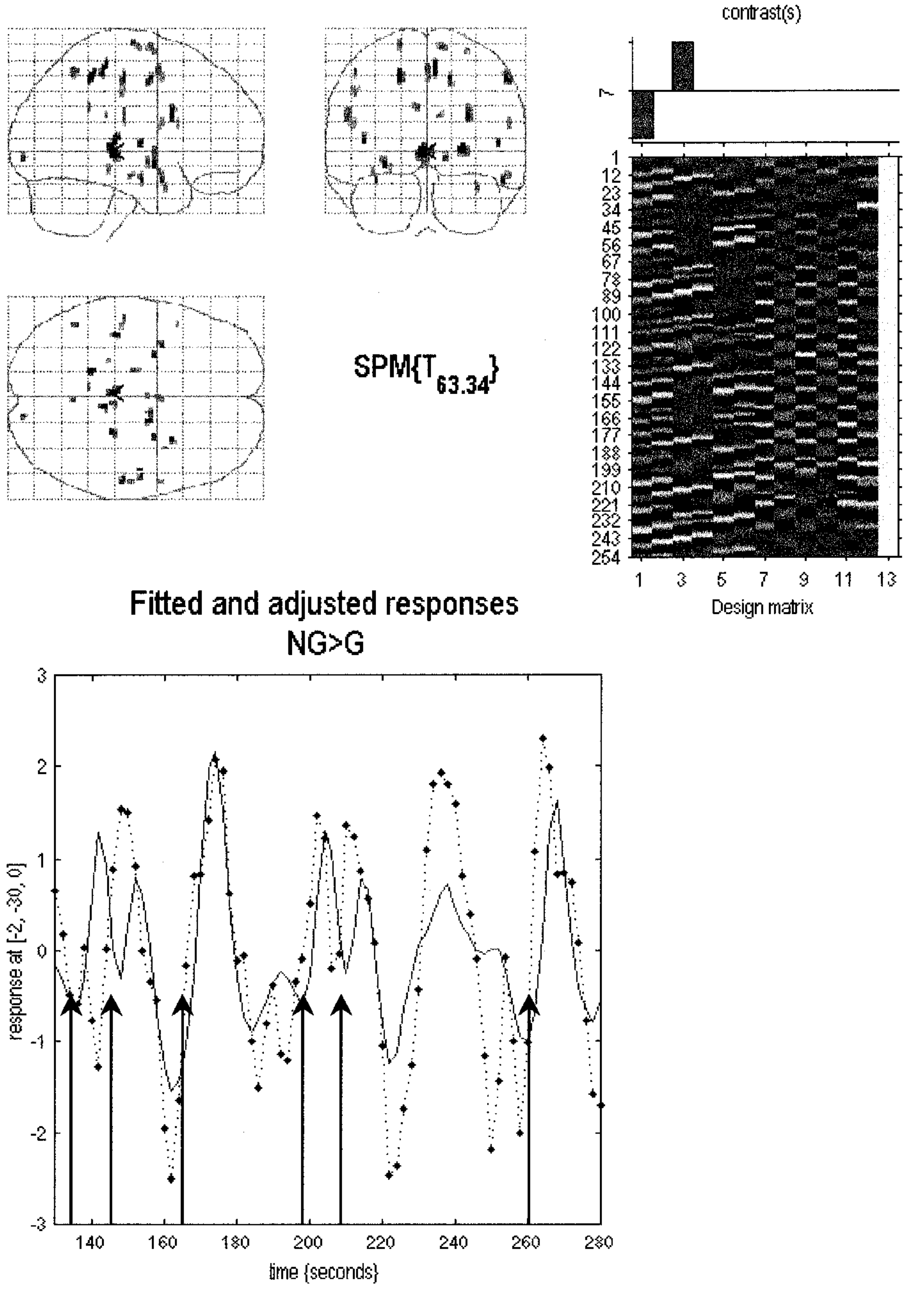

Figure 7-2. An example of single subject data. The results come from a single Parkinson's patient. The contrast tested for greater activation during response inhibition than during response. The top left shows the activation results displayed in the "glass brains". The top right shows the design matrix. On the bottom is a section from the timecourse3 of the most statistically significant voxel cluster (indicated by the red "<"). In this dataset, the subject correctly responded to inhibition stimuli presented at the following times (in seconds): 135.5, 145.5, 165.5, 198, 208 and 260.5 (arrows). An error of commission occurred at 228 seconds. Note that the peaks of the hrf correspond well to these onsets.

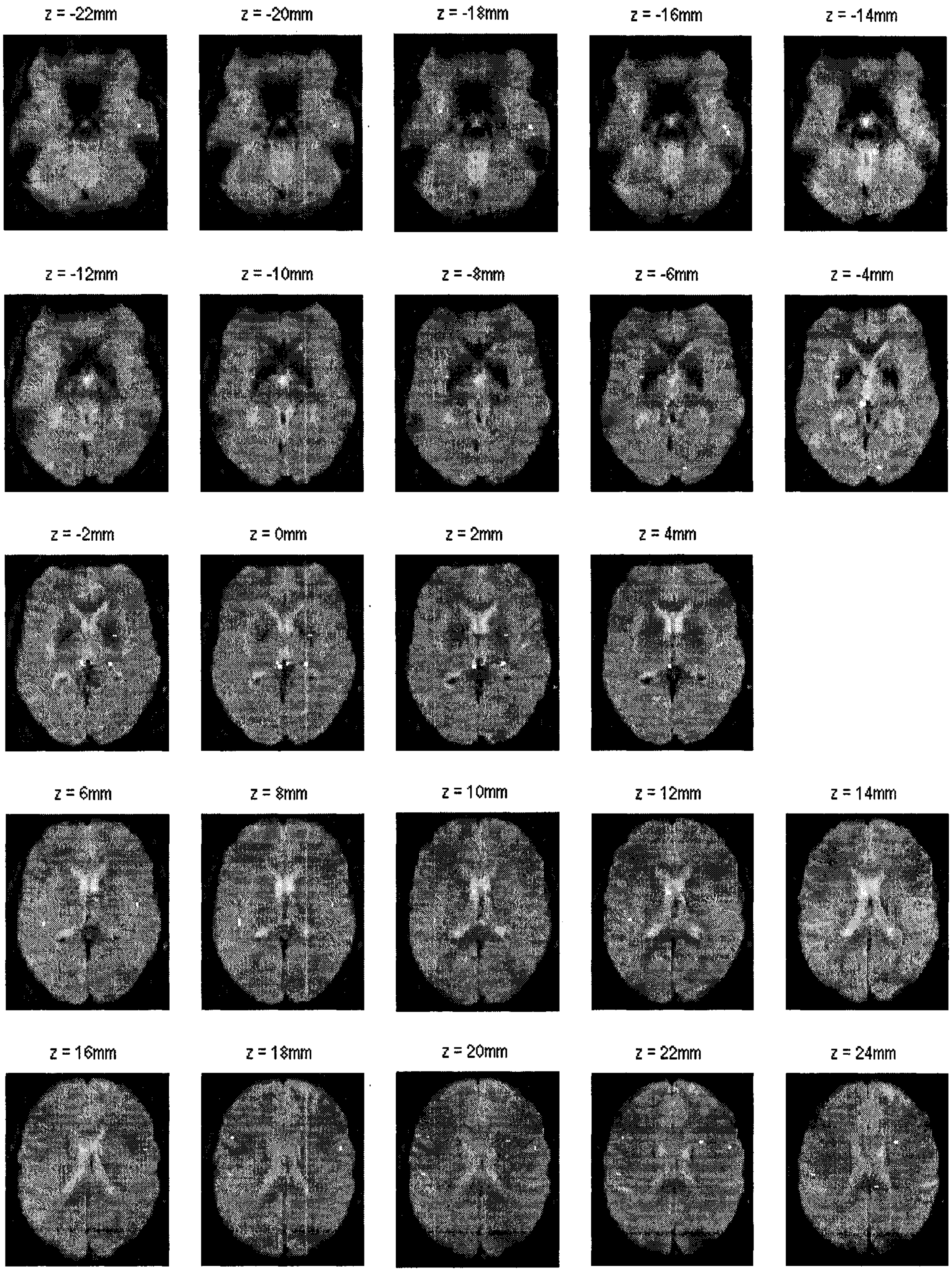

Figure 7-3a. Axial slices from the single subject functional data in Figure 7-2. Active spots are shown here in white and are not intensity-scaled according to statistical significance in order to be clearly seen. Slices are shown in ascending order, continued in Figure 7-3b.

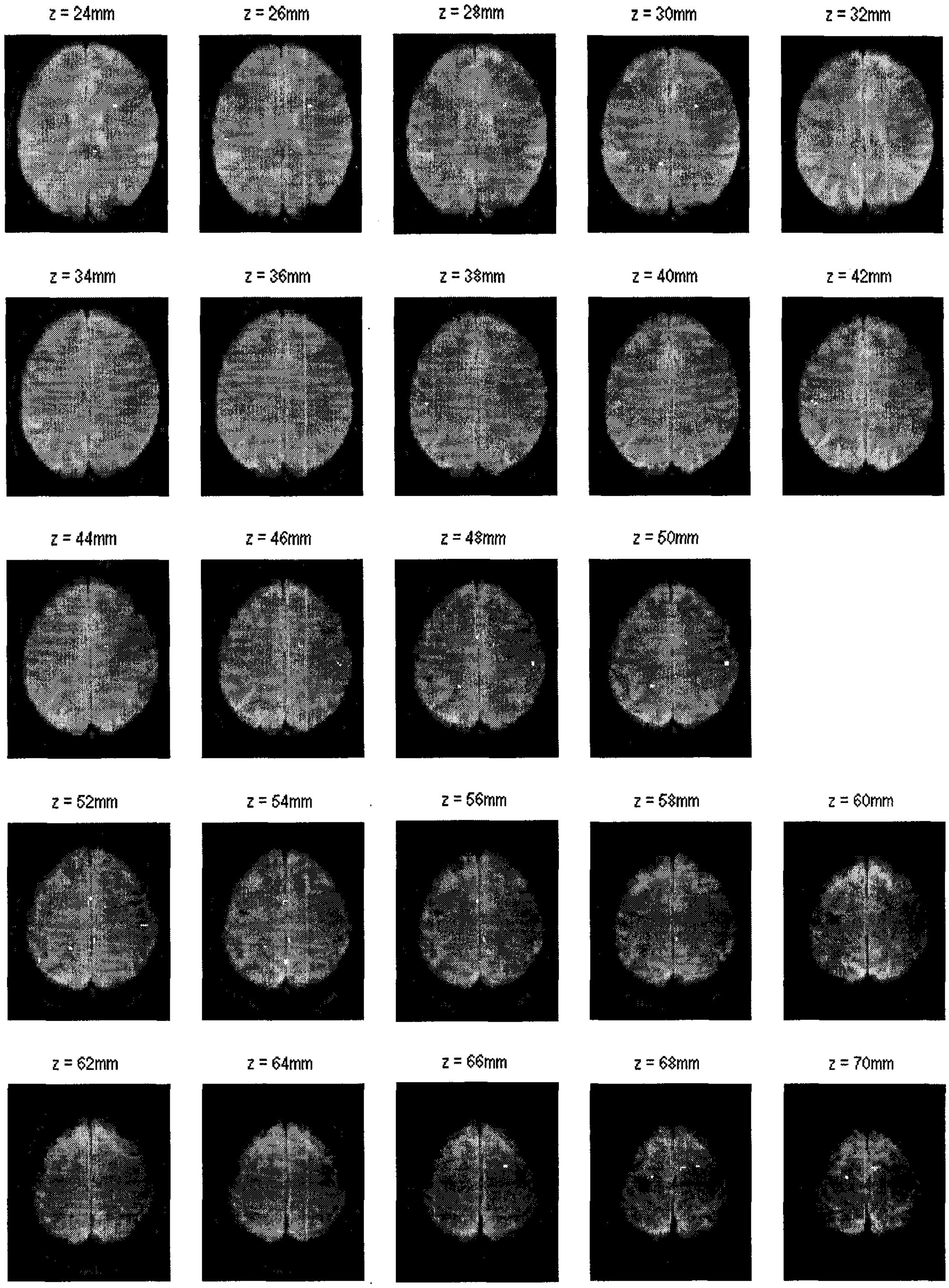

Figure 7-3b. Continuation of axial slices from the single subject functional data started in Figure 7-3a. Once again, slices are shown in ascending order.

7.2.3.3 Between-Group fMRI Comparisons

Four separate comparisons were made between the two groups. The first two statistically assessed whether or not there were areas more significantly activated during inhibition (implicitly compared to baseline) in one group compared to the other (Tables 7-3, 7-4, Figure 7-4). Interestingly, the two analyses showed that particular areas of the superior temporal gyrus and the pons were more active in patients than subjects, while neighbouring points in the same regions displayed the opposite behaviour. A similar finding occurred in the limbic lobe. The same results also emphasized the greater importance of the midbrain and thalamus in control inhibition, and culmen, declive, superior frontal gyrus and middle temporal gyrus in Parkinsonian inhibition.

Table 7-3. Clusters Displaying Greater Activation (or less deactivation) in Parkinson's Patients than in Controls during Response Inhibition ($p<0.001$, 3 voxel minimum cluster size)

Region	Side	Brodmann Area	Cluster Location		
			x	y	z
Temporal Lobe					
Middle Temporal Gyrus	Left		-46	-1	-20
Superior Temporal Gyrus	Left	BA 38	-50	11	-14
Anterior Lobe					
Nodule	Left		-2	-48	-31
Culmen	Left		-16	-42	-23
	Right		10	-48	-21
Frontal Lobe					
Superior Frontal Gyrus	Right		26	40	20
Pons	Right		14	-40	-28
			20	-35	-34
	Left		-18	-33	-32
Posterior Lobe					
Declive	Right		8	-57	-11
Limbic Lobe					
Cingulate Gyrus	Left	BA 32	-10	19	30
	Right		18	11	31
		BA 23	8	-36	26

Table 7-4. Clusters Displaying Greater Activation (or less deactivation) in Controls than in Parkinson's Patients during Response Inhibition ($p<0.001$, 3 voxel minimum cluster size)

Region	Side	Brodmann Area	Cluster Location		
			x	y	z
Midbrain	Left		-8	-31	-5
Pons	Right		14	-24	-19
Thalamus	Left		-8	-3	13
Temporal Lobe					
Superior Temporal Gyrus	Left	BA 22	-51	-40	9
		BA 13	-46	-44	22
Limbic Lobe					
Parahippocampal Gyrus	Left	BA 35	-18	-37	-8
		BA 35	-18	-26	-14

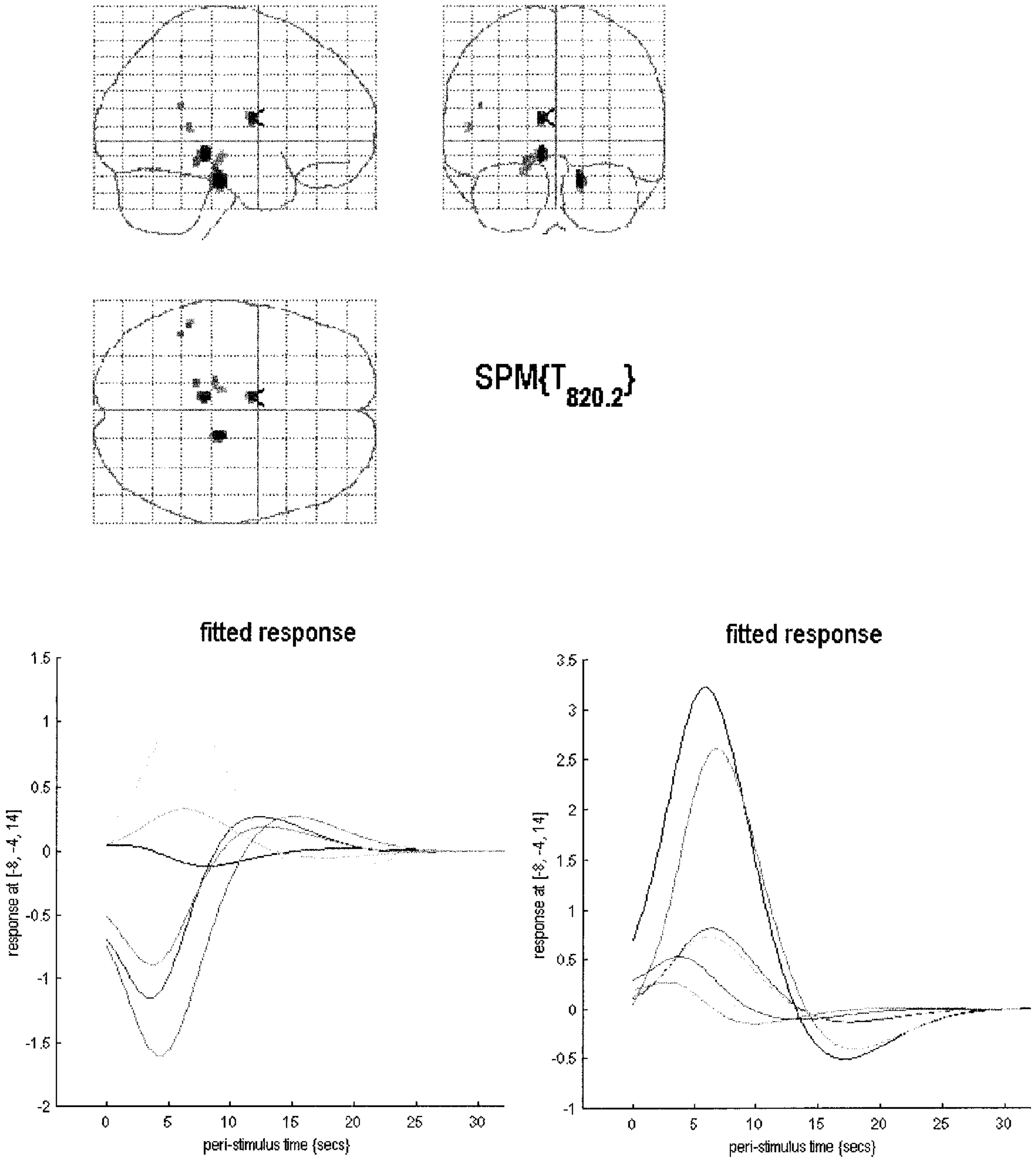

Figure 7-4. Areas of greater functional activation in control subjects than in Parkinson's patients during response inhibition. The top diagram shows the functional activation itself. The bottom timecourses show the "typical" hemodynamic response, at the highlighted voxel ("<"), from each Parkinson's patient (left) and from each control subject (right) following a NoGo stimulus. Note that most controls show a positive hrf, and hence activated this voxel, while 3 of 6 Parkinson's patients not only didn't activate this voxel during response inhibition, they deactivated it.

A second comparison was made that was an interaction of the factors group by task (Tables 7-5, 7-6). Here regions were sought that were not only more active in one group than in the other, but more active during inhibition than during response. The above comparisons examined a main effect of response inhibition, comparing it to an implicit baseline. The new comparison further contrasts inhibition with response. For example, a Parkinsonian region equally active during both response and response inhibition, but inactive in controls, might be identified by first comparison (preceding paragraph), but not in the present comparison. This task by group interaction accentuated regional behavioural variability within the temporal frontal and parietal lobes: patients preferentially activated the superior temporal and postcentral gyri, and controls, the middle temporal, supramarginal, superior parietal and medial frontal gyri.

Table 7-5. Clusters Displaying Greater Activation (or less deactivation) in Parkinson's Patients than in Controls during Response Inhibition compared to during Response ($p<0.001$, 3 voxel minimum cluster size)

Region	Side	Brodmann Area	Cluster Location		
			x	y	z
Temporal Lobe					
Superior Temporal Gyrus	Left	BA 38	-50	11	-14
		BA 38	-36	5	-9
Anterior Lobe					
Culmen	Left		-16	-42	-23
Frontal Lobe					
SubGyral	Right		32	22	19
Limbic Lobe					
Cingulate Gyrus	Left	BA 32	-14	21	28
Parietal Lobe					
Postcentral Gyrus	Right	BA 40	44	-27	46

Table 7-6. Clusters Displaying Greater Activation (or less deactivation) in Controls than in Parkinson's Patients during Response Inhibition compared to during Response ($p<0.001$, 3 voxel minimum cluster size)

Region	Side	Brodmann Area	Cluster Location		
			x	y	z
Temporal Lobe					
Middle Temporal Gyrus	Left	BA 22	-57	-48	4
Parietal Lobe					
Supramarginal Gyrus	Right	BA 40	40	-47	34
Superior Parietal Lobule	Right	BA 7	38	-62	51
Frontal Lobe					
Medial Frontal Gyrus	Right	BA 9	18	43	14

7.2.4 Discussion

The behavioural data support previous observations that Parkinson's patients have greater difficulty with response inhibition than age-matched healthy subjects. This was evident from the statistically significant greater number of errors of commission in patients (i.e. tapping during NoGo stimuli), and also suggested by the reaction time data.

Several authors have reported poor performance in Parkinson's patients when conducting cognitive tasks requiring the frontal lobe, including planning, skill learning, habit learning and attentional set-shifting (summarized by Dagher et al. 2001). This is in agreement with the present findings of a greater number of errors of commission in patients when conducting a Go /NoGo task that may contain some of these mental processes.

7.2.4.1 Comparison of Present Findings with those of Garavan

Given that the present experiment is a recreation of a study conducted by Garavan (1999), it is logical to begin by comparing their respective findings (Garavan's results are reprinted in Table 7-7 for convenience). It should be noted that the subject base in the latter study was 14 healthy controls, mean age 32 years. Healthy subjects in the two studies share only one region in common - the medial frontal gyrus. Whether or not Parkinson's patients should be compared with healthy controls is the focus of this paper, nonetheless, both patients and Garavan's controls activate the inferior parietal lobe and the fusiform gyrus. Furthermore the right hemispheric dominance of response inhibition, observed by Garavan was supported neither by the present results nor by an earlier pilot study.

There are several potential reasons for these discrepancies. Garavan presented a total of 1000 letters including 150 targets and 25 lures. Here, the prepotency of the inhibition was lessened in accord with the arguments of Liddle 2001 (see introduction) to 104 targets and 24 lures. However, Garavan's controls produced an average 1.9 ± 1 errors of commission compared to 7 ± 4.8 (PD) and 2.7 ± 2.0 (Control) in this study, creating approximately 23 lures (Garavan controls) versus 12 (PD) and 19 (controls). With so few valid stimuli, especially for the patients, there were not enough observations to warrant statistically significant conclusions. Furthermore, with fewer observations there is a greater chance of observing aberrant behaviour unrepresentative of the typical population response. The present shortcomings could be avoided by additional pre-scanning practice (clearly the amount provided was insufficient) and by increasing the number of lures (with the detriment of increasingly long hence tiresome and boring sessions). In addition, statistical significance may be attainable with more subjects – perhaps with 14 subjects per group to be comparable with the original Garavan work. One must also consider the age difference between each experiment's subjects (mean age of 32 (Garavan control) vs. 60 (PD) and 52 (Control) years). This difference alone, whether through reduced mental acuity, failing eyesight, etc., might lead to greater demands on attention to task, more rapid attention loss, and more rapid fatigue, explaining both the greater number of errors and perhaps the differences in functional activation. Finally, different statistical packages were used in each experiment. SPM, used here, is the standard package used in functional imaging. Validation of the approach used by Garavan requires statistical expertise. Without such, one may still speculate that a lack of equality between the two techniques influenced the respective observations.

Table 7-7 Reprint of the Observations from Garavan 1999.

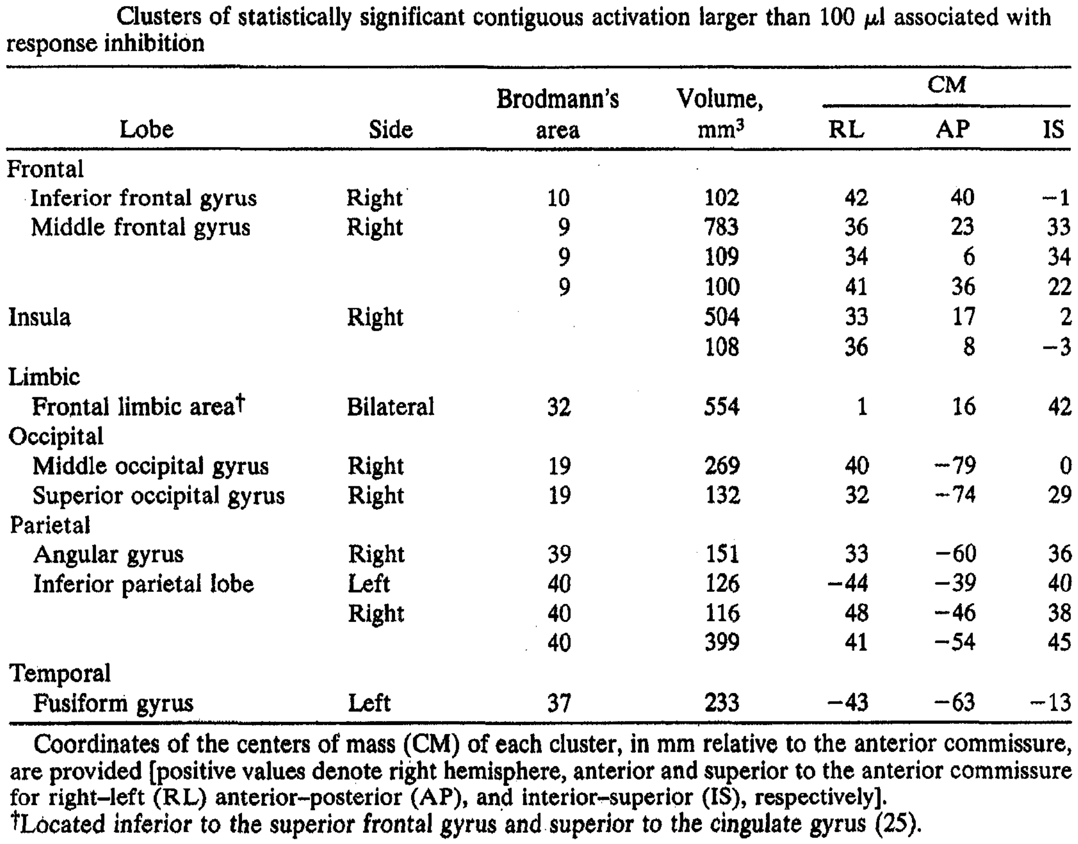

Clusters of statistically significant contiguous activation larger than 100 μl associated with response inhibition

				CM		
Lobe	Side	Brodmann's area	Volume, mm^3	RL	AP	IS
Frontal						
Inferior frontal gyrus	Right	10	102	42	40	−1
Middle frontal gyrus	Right	9	783	36	23	33
		9	109	34	6	34
		9	100	41	36	22
Insula	Right		504	33	17	2
			108	36	8	−3
Limbic						
Frontal limbic area†	Bilateral	32	554	1	16	42
Occipital						
Middle occipital gyrus	Right	19	269	40	−79	0
Superior occipital gyrus	Right	19	132	32	−74	29
Parietal						
Angular gyrus	Right	39	151	33	−60	36
Inferior parietal lobe	Left	40	126	−44	−39	40
	Right	40	116	48	−46	38
		40	399	41	−54	45
Temporal						
Fusiform gyrus	Left	37	233	−43	−63	−13

Coordinates of the centers of mass (CM) of each cluster, in mm relative to the anterior commissure, are provided [positive values denote right hemisphere, anterior and superior to the anterior commissure for right–left (RL) anterior–posterior (AP), and interior–superior (IS), respectively].

†Located inferior to the superior frontal gyrus and superior to the cingulate gyrus (25).

7.2.4.2 Functional Anatomy of Prominent Activations

The extensive network of interconnections within the brain, coupled with the broad physical coverage of many neuroanatomical regions, makes characterizing the function of a particular region both difficult, and to an extent, speculative. The discussion below postulates explanations for the observed activation using established functional anatomical knowledge relevant to the nature of the present task.

The thalamus is a grouping of many nuclei that act as information relays to other areas of the brain. Since the activity was not localized to a specific nucleus, evidence of thalamic hyperactivity in controls is impossible to interpret.

The pons and midbrain contain motor programs for rapid eye movements or saccades. In particular, the pons houses neural circuitry for horizontal movements and the midbrain, vertical movements. Given the demand of this task to focus on rapidly changing letters of the alphabet, it is easy to understand why these areas were activated. On the other hand, it is difficult to explain why such activity would be greater in one subject population over another (Tables 7-4, 7-5). This peculiarity is moderated by the fact that both groups showed preferential activation in different focal points of these same regions. Finally, since neither any pons nor midbrain activation is evident in the group by task interaction (Tables 7-5, 7-6), this suggests that both areas are also used in both the Go and NoGo response - as expected since both require rapid eye movements.

The anterior and posterior lobes are sections of the cerebellum, which is generally thought to control planning and coordination of movement (Nolte). The anterior lobe is involved in coordinating limb movements, while the posterior coordinates voluntary movements. An immediately obvious conclusion is that these areas coordinate or plan the appropriate Go or NoGo response, specifically whether or not to press the button. However, although both subject groups activated the culmen, Parkinson's patients clearly activated it to a greater extent. Similarly, declive activity was only apparent in a comparison of Parkinson's patients versus control subjects. Therefore another possibility is that this activation may reflect tremor-related movement as reported by Deiber et al (1993). This could also be evidence of functional compensation in Parkinson's patients: increased use the cerebellar-parietal premotor loop in preference to the dysfunctional corticostriatal loop (Rascol 1997, Sabatini 2000, Samuel 1997).

The limbic system, comprised of the limbic lobe and linked structures, participates in emotional response, drive-related behaviour, and perhaps most pertinent in the present context, memory (Nolte). Memory-related activation is logical given the strong working memory component of this task; the subject had to remember the previous target letter (X or Y) since this determined their response to the next X or Y observed. Both groups activated the limbic lobe, although patients tended to more significantly activate the cingulate gyrus, and subjects the parahippocampal gyrus. The reasons for this difference are unclear. However, it should also be noted that in both groups, the activation was mostly eliminated with the additional constraint that the inhibition activation be greater than the response activation (Tables 7-5. 7-6). In other words the activation was common to both tasks, as would be the case if activation were memory-related. Finally, the only justification of an emotional response comes from the fact that Parkinson's disease can include symptoms of depression. However, there was no evidence to suggest that this was true of the patients in this study.

The hippocampus and adjacent areas have been associated with declarative memory (memory of things that are recognizable, such as objects, smells, etc.) (Squire1996). In this context, greater parahippocampal activation in controls might reflect better retention of previous target stimuli (whether an X or a Y). This might explain the greater number of errors of commission in Parkinson's patients.

The temporal lobe has a wide variety of functions, and its lateral surface consists of the superior, middle and inferior temporal gyri. The middle temporal gyrus controls complex aspects of learning and memory (Nolte) both of which are required in the present task. Superior temporal gyrus activation was a consistent finding across subjects and is particularly difficult to explain. The superior temporal gyrus includes the auditory association area and the primary auditory cortex. Therefore it is most commonly associated with the perception of complex auditory information such as speech and rhythm, and auditory memory (http://www.hucmlrc.howard.edu/neuroanat/Lectures/limbsys.htm) and could be triggered by background acoustic scanner noise. However, comparisons inherently compare either inhibition to baseline or to response. Scanner noise and resultant activation should be common to all three and should therefore cancel out in the comparisons. Next, consider that most superior temporal gyrus activation occurs in Brodmann area 38. This area has been associated with numerous functions including anxiety, verbal memory, delayed response working memory, motor learning and face and object visual recognition (http://www.trincoll.edu/~dlloyd/brodmann.html). Several of these roles are plausible in the present context.

Several studies have reported prefrontal and parietal activation, including the medial frontal gyrus and the superior and inferior parietal lobules, during response inhibition tasks (Garavan 1999; Liddle 2001). Most studies however, have assigned the role of response inhibition to the lateral prefrontal areas (Liddle 2001; Konishi 1998; etc.), whereas the prefrontal areas activated here are mostly medial. This can be accounted for in the following manner. Liddle demonstrated exclusively medial activity in the prefrontal region in a comparison of inhibition to baseline. It wasn't until he compared inhibition to response, that the strong lateralization of inhibition-related activity was made evident. In the present study, most contrasts compared inhibition to baseline (tables 7-1 to 7-4). Those that did compare inhibition to response (tables 7-5, 7-6), also compared across subject types - in other words they tested for areas displaying greater activation between subject groups, between inhibition and response conditions. If the lateral prefrontal regions are unaffected in Parkinson's disease, this contrast would show no difference because both groups would show equivalent lateral prefrontal activity.

7.2.5 Garavan Experiment Conclusion

It is difficult to draw conclusions from the following data, given the paucity of recorded inhibition responses, especially for the Parkinson's patients. The insufficient number of observations may have skewed the results, reflected by the difference in the findings of this re-creation and those of the original Garavan study. Nevertheless, many of the observed activation differences between the two subject groups can be rationalized, suggesting that although statistically weak, they are credible. The fact that some of the observed activity may reflect an oddball response cannot be discounted. Likewise, analysis of the functional activation has demonstrated a strong working memory component of the present task that cannot easily be distinguished from true response suppression behaviour. The present study could therefore be improved by using an equal probability test (perhaps based on Konishi 1998) to avoid oddball and working memory effects.

Response inhibition appears to be mediated by a network of areas including both ventral and dorsal frontal areas (Garavan 1999; Liddle 2001). The present study suggests a difference in the circuitry used by both Parkinson's patients and control subjects during response inhibition, and confirms previous findings of inhibition abnormality in Parkinson's patients (Franz 2002). Differential functional activation of Parkinson's patients compared to control subjects during response inhibition, may ultimately offer insight into the nature of symptoms characterizing this disorder, such as resting tremor.

7.3 Scholz Study

7.3.1 Introduction

Parkinson's disease is characterized pathologically by the degeneration of dopaminergic neurons in the substantia nigra. While several studies have examined the downstream cortical effects of the dysfunctional basal ganglia (BG) –thalamo-cortical loop resulting from this loss of nigral neurons, few have focused on the BG itself - perhaps because of its particularly weak BOLD signal (Scholz 2000) or the difficulty evoking consistent activation (Scholz 2000). Pre-existing evidence obtained with PET suggests an abnormality of basal ganglia function in Parkinson's disease (Dagher 2001; Playford 1992, Rowe 2002; Owen 1998; Jahanshahi 1995), but few Parkinson's studies to date have exploited the superior temporal and spatial resolution offered by fMRI. The present study compares BG functional activation in Parkinson's patients with that of age-matched controls using fMRI in conjunction with a motor activation paradigm known to elicit BG activation in healthy controls (Scholz 2000).

7.3.2 Materials and Methods

7.3.2.1 Subjects

Six Parkinson's patients (5 males 1 female mean age 59±11 years), off medication for ~12 hours, and seven age-matched controls (4 males, 3 females, mean age 56±5 years) participated in the study. Only mildly affected (Stage 1 and 2 Hoehn and Yahr) Parkinson's patients were included, as in the drug-deplete state, these patients are the most comfortable, have the least tremor (and resultant head motion), and are typically able to complete the task. All subjects were right handed, ascertained through simple inquiry. Subjects provided informed written consent concerning their participation in the experiment.

7.3.2.2 Experimental Design

The paradigm consisted of 14 alternating epochs of rest and unilateral movement, each 30 seconds long. The movement consisted of finger-tapping alternating with toe-wiggling (figure 7-5). Subjects were instructed to alternate between tapping their index finger against their thumb, 4 times over two seconds, (i.e. 2Hz frequency) and wiggling their big toe, also 4 times over 2 seconds. An external pacing tone played every 2 seconds notified the subject when to switch from toe-wiggle to finger tap and vice versa, and helped the subject pace movements at the desired 2 Hz frequency. The experiment was conducted twice for each subject, once using each side of the body. To minimize the effects of practice on task performance, half of the subjects conducted the left experiment first, the others the right one first.

Training prior to the imaging session ensured both a consistent amplitude and correct pace of motions across subjects. When the subject was in the magnet itself, neither factor was externally recorded and was instead monitored by the researcher throughout the experiment.

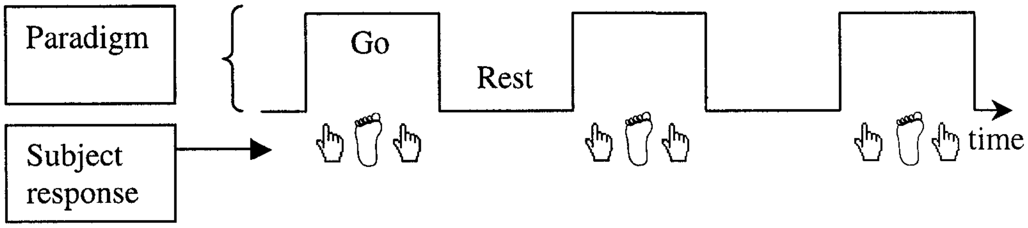

Figure 7-5. A simplified overview of the finger-tapping, toe wiggling paradigm used in the Scholz study.

7.3.2.3 Imaging

The study was conducted using a Siemens Sonata 1.5T clinical scanner. One hundred and forty volumes were collected in each unilateral movement session using a single-shot, multislice, motion-corrected (PACE) EPI sequence. Each volume consisted of twenty-four 4mm slices, with 1mm inter-slice spacing. The echo time and repetition time were 50 and 3000ms respectively. The FOV was 22x22 cm with 128 data points sampled in each of the phase encoding and readout directions. Finally, a 90° flip angle was used along with a bandwidth of 1628 Hz/Pixel. The first two images were discarded to allow for spin saturation effects. In addition, to accommodate for the delay in the hemodynamic response, the first image in each epoch was excluded from analysis.

Patient head movements were minimized in two ways, by physical restraints placed over the headphones and through real-time adjustment of slice position and orientation using the PACE sequence (Thesen 2000).

7.3.2.4 Data Analysis

The functional MRI data were pre-processed and analyzed using SPM99 software (Wellcome Department of Cognitive Neurology, London, UK). Images were realigned to the first volume collected and normalized to a common stereotactic space approximating that of Talairach and Tournoux (Talairach and Tournoux 1988). Images were spatially smoothed with a 4mm full-width half-maximum isotropic Gaussian kernel (see Appendix E).

Because of the limited sample population size and the focus on the basal ganglia, the most appropriate group analysis method is the fixed effects approach. Random effects is the most desirable approach to use, in that inferences may be extended to the population from which subjects were sampled. However, to achieve this level of inference, a large number of subjects are required, in order for effects to reach significance. The present study recruited 6 Parkinson's and 7 control subjects, yet most SPM experts agree that at the very least 10-12 subjects per group are required. Thus, the present study simply did not have enough subjects to use random effects analysis.

By focusing the study on the behaviour of the basal ganglia, a second alternative, conjunction analysis, was eliminated. Conjunction analysis tests whether each and every subject displayed a particular effect. Thus the implications are stronger than fixed effects, which is more demonstrative of an average effect across subjects. The basal ganglia however, do not activate consistently across subjects (Scholz 2000). Therefore, using conjunction analysis was not feasible either.

Each subject was entered as a separate session into a single design matrix. The subject response was modeled as a boxcar convolved with the hemodynamic response function, and global scaling was included. Six motion (3 rotation and 3 translation) regressors characterizing subject movement during the scanning session were included in the model, for each subject, as nuisance covariates. The data were both high pass filtered to eliminate low frequency noise, and temporally smoothed with a hemodynamic response function[4].

7.3.2.5 Region of Interest Analysis

The region of interest within the basal ganglia was identified using MRIcro (Rorden) in conjunction with the Automated Anatomical Labelling map (Tzourio-Mazoyer et al.). It consisted of the pallidum, caudate nucleus and putamen (figure 7-6).

7.3.3 Results

The average absolute displacement of any scan from the reference position, in the x, y and z directions was: 0.18±0.21mm vs. 0.48±0.63mm, 1.24±0.70mm vs. 1.34±0.82mm, and 0.22±0.20mm vs. 0.72±0.86mm, for controls versus patients respectively.

Both movement paradigms (left or right movements) were analyzed using 4 different contrasts: two characterizing within-group behaviour, and two more depicting between-group differences (summarized in Table 7-8).

7.3.3.1 Within-Group Basal Ganglia Activity

For the left finger-tapping/toe wiggling, neither Parkinson's patients nor control subjects showed evidence of any suprathreshold activation (that is, activation surpassing the small volume corrected ($p = 0.05$) threshold). During right finger-tapping/toe-wiggling however, Parkinson's patients significantly activated both the right caudate body and the right putamen.

7.3.3.2 Between-Group Basal Ganglia Activity

Inter-group comparisons were also performed for both unilateral tasks.
Clear differences in basal ganglia activation were observed between the two subject groups. Control subjects activated the basal ganglia to a greater degree in both the left and right movement sessions – the right caudate body during left movements (figure 7-7) and the right caudate tail, right medial globus pallidus, and left putamen during right movements (figure 7-8). In contrast, Parkinson's patients did not show any significantly greater basal ganglia activity than controls during either right or left movements.

Table 7-8. Significantly Active Basal Ganglia Clusters (Small Volume Corrected, $p = 0.05$)

Task	Contrast	Region	x	y	z	T-statistic
Left Movements						
	PD Left vs. Rest	*No Suprathreshold Clusters*				
	Control Left vs. Rest	*No Suprathreshold Clusters*				
	PD > Control Left vs. Rest	*No Suprathreshold Clusters*				
	Control > PD Left vs. Rest	R Caudate Body (looks like head – very anterior)	12	14	16	4.40
Right Movements						
	PD Right vs. Rest	R Caudate Body (looks like head – very anterior)	14	12	16	6.22
		R Putamen (anterior)	18	2	5	4.74
	Control Right vs. Rest	*No Suprathreshold Clusters*				
	PD > Control Right vs. Rest	*No Suprathreshold Clusters*				
	Control > PD Right vs. Rest	R Caudate Tail	32	-24	-4	6.37
		R Medial Globus Pallidus	8	2	-2	5.33
		L Putamen *(anterior)*	-22	4	9	4.88

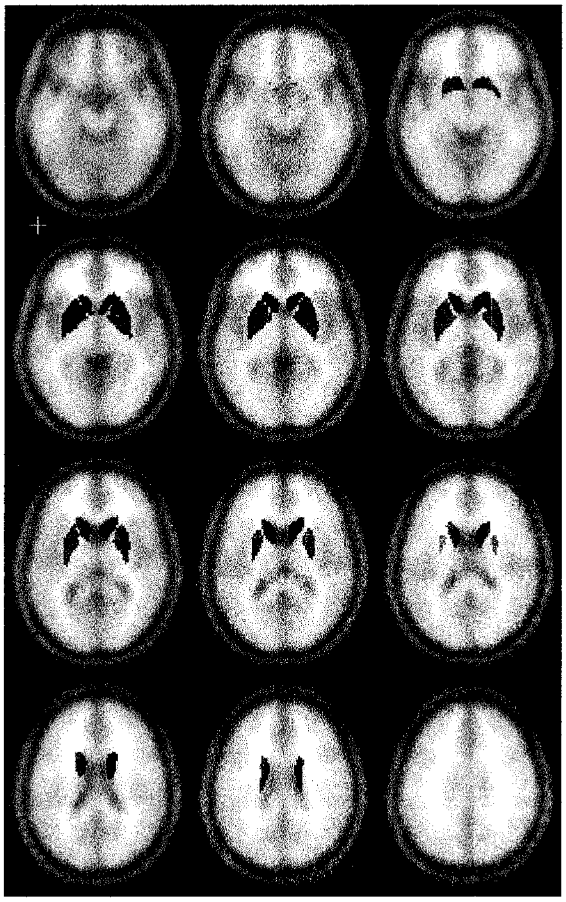

Figure 7-6. Montreal Neurological Institute (MNI) T_1 template axial slices of the brain in ascending order from left to right, top to bottom. The basal ganglia region of interest (ROI) used for the small volume correction is shown superimposed in red (created in MRIcro using the AAL template). This ROI consists of the caudate nucleus, pallidum and putamen.

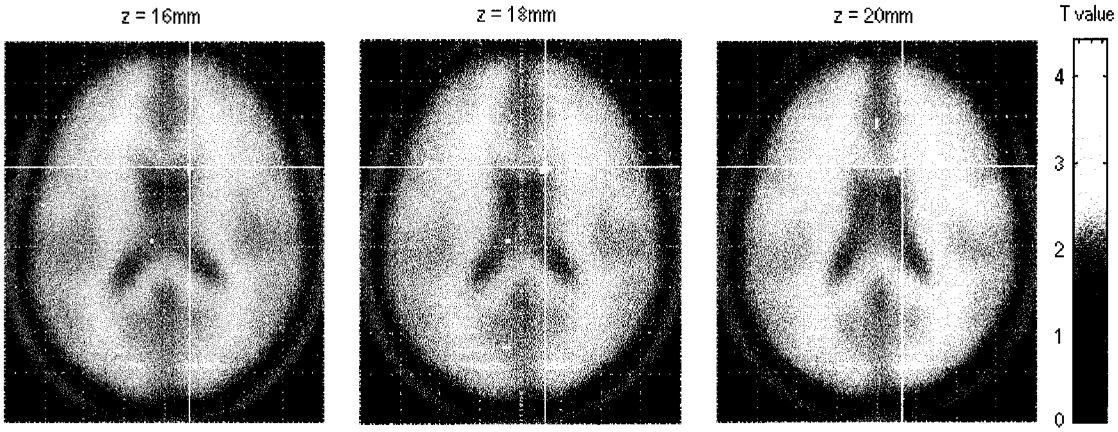

Figure 7-7. Left movement Scholz results. The right caudate body was identified as being significantly more active in control subjects than in Parkinson's patients during left movements. The activation is superimposed on the SPM T_1 template.

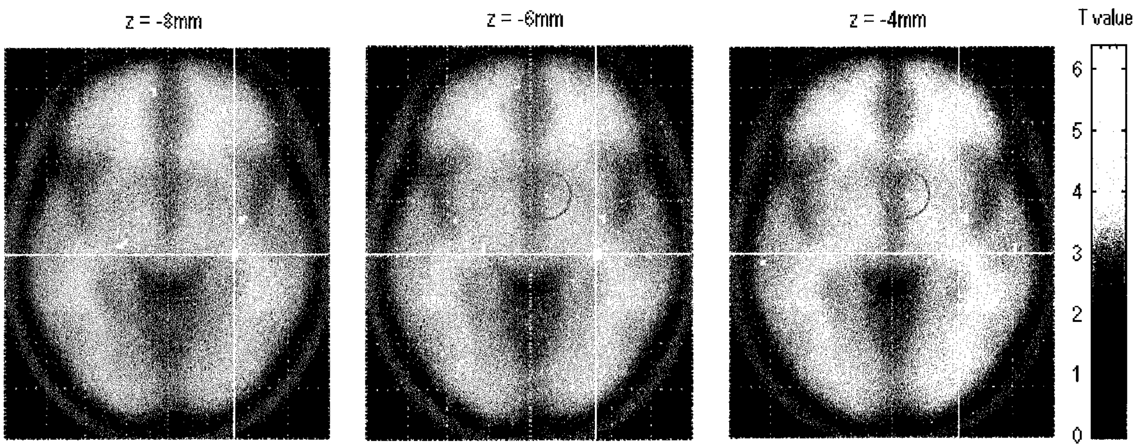

Figure 7-8. Right movement Scholz results. The right caudate tail (cross-hairs), the right medial GP (circle) and the L Putamen (not shown) were significantly more active in control subjects than in Parkinson's patients during right movements. Once again, the activation is superimposed on the SPM T_1 template.

7.3.4 Discussion

Since the purpose of this study was to compare basal ganglia activation between patients and healthy controls, the within-group findings will not be discussed in great detail. While it is tempting to form conclusions based upon observed within-group activation differences, such conclusions are qualitative. The accurate statistical approach to compare across groups, requires between-group contrasts. The interesting finding from the within-group results is the presence of right BG activation in Parkinson's patients during right movements. This suggests that although the Parkinsonian basal ganglia appears to be impaired (see subsequent discussion), several nuclei retain some of their functionality.

The basal ganglia have projections to several cortical areas and therefore have been associated with a wide variety of functions both motor and cognitive (Nolte). The putamen receives signals from the motor and somatosensory cortices, and sends them through the globus pallidus (GP) to the motor, premotor and supplementary motor areas, and therefore is generally linked with motor functions. The caudate nucleus (CN) on the other hand, receives signals from cortical association areas and sends them through the GP, predominantly to prefrontal regions. Therefore this area has a greater role in cognitive than motor functions. The observed functional activation will be explored by investigating each region, the GP, the putamen and the CN separately.

There are several explanations justifying the greater GP activation in controls than in patients observed during the right movement task. Output signals exit the BG through the internal globus pallidus (GPi) and substantia nigra reticulata. While most connections from the GPi are ipsilateral, some bilaterality does exist (Nolte). On this basis, the R medial GP activity reported here, may simply be an extension of either the R caudate or L putamen activity also observed. However, regional cerebral blood flow increases in the

GPi of controls, with concurrent decreases in Parkinson's patients, has been reported during a planning (Tower of London) task and during spatial working memory (Owen 1998). Investigators attributed this to a reduction in BG output due to striatal dopamine deficiency in Parkinson's patients.

Several studies have demonstrated activation of the anterior region of the putamen during movement tasks. In the context of finger movement sequences, it has been implicated in new learning (bilateral activation), improving performance (right side) and selecting movements (left side) (Jueptner 1998). In addition, the anterior putamen (bilaterally) seems preferentially activated during externally paced but not self-paced movements, suggesting a role in mapping sensory input to the motor response (Menon, V. 1998). This is supported by neuroanatomical information showing temporal, frontal (non-motor) and parietal connections to the anterior striatum (caudate nucleus and putamen) (Parent 1995). Furthermore, a cortical network involving the striatum is active in cognitive tasks such as habit learning and spatial working memory (Callicott 1999; Poldrack 1999), while the striatum and the prefrontal cortex may control temporal ordering of sequences (Beiser and Houk, 1998).

In studies with Parkinson's patients, the contralateral putamen is active in controls but not in patients during movement selection (Playford 1992). Comparisons across the two groups have also shown relative right putamen hypoactivity in patients during right-handed sequential finger tapping (Rowe), and relative L putamen hypoactivity in patients during self-initiated "when to do" movements (Jahanshahi 1995). These data are supported by previous findings highlighting decreased metabolism and dopamine deficiency in the Parkinsonian putamen (Brooks 1997, Brooks 1990) or the use of alternate cerebelloparietal circuitry in preference to the dysfunctional BG-thalamo-cortical loop (Playford 1992).

As mentioned earlier, while the putamen has a role relating to motor functions, the caudate nucleus has a more cognitive role. Sometimes in combination with the anterior putamen, caudate nucleus activation has been demonstrated during new learning (bilaterally) and improving performance (right side), with attention redirected towards an overlearned task (right) (Jeuptner 1998) and bilaterally during externally-paced and not self-paced movements (Menon V. 1998).

In accordance with the present findings, the caudate nucleus of Parkinson's patients appears to be dysfunctional. Greater activation in the right caudate nucleus (R CN) of healthy controls compared to Parkinson's patients was demonstrated during spatial working memory tasks (Owen 1998) and R CN blood flow correlated with task complexity in controls but not in patients during a planning (Tower of London) task (Dagher 2001).

Of the plausible explanations, the R CN activation in the present study most likely results from either attention to an overlearned task or the mapping of sensory input (namely the pacing tone) to motor response (the movement pace and switching action). However, as indicated above, the striatum is also involved in event timing and habit learning. Both roles are plausible in the context of the present experiment.

The left anterior putamen activation is in agreement with the findings of Scholz (2000) during an identical task, and has many possible sources including sensory to motor mapping and selection of timing (self-initiated pacing of 4 movements between pacing tones in agreement with Jahanshahi 1995/Playford 1992) or movements (Jeuptner 1998).

The variability in the precise location of BG activation in left versus right movements, such as R caudate head (left task) vs. R caudate tail (right task) and globus pallidus and putamen activation only during the right task, is difficult to explain. To remove the confounding effects of practice on performance, half of the participants conducted the left task first, the others the right task first. The division was maintained within groups as well. Therefore the variability cannot be attributed to an interaction of new learning vs. overlearned repetition effects with task type.

It is possible however, that this inconsistency could stem from the imbalance in symptoms of the hemi-Parkinson's patients. None of the patients were in the advanced stages of the disorder, therefore their symptoms are significantly worse on one side of the body. This had obvious ramifications on task performance. On the more affected side, some patients were unable to provide either the correct amplitude or pace of tapping/wiggling. Some were unable to provide any such motion and instead were asked to nevertheless think that they were moving their toes and fingers. It is also possible that movements involving the more affected side may have demanded greater effort and or attention to the task. Differences in task execution among patients due to asymmetric symptoms may explain why different BG regions were highlighted in the right and left comparisons.

7.3.5 Scholz Experiment Conclusion

The present study confirms previous findings of impaired activation within the basal ganglia of Parkinson's patients studied when off medication for 12 hours. The observed caudate nucleus and putamen activation may result from attention to the overlearned task, sensory to motor mapping and/or the inherent movement selection of the switching process. Given that task performance was similar in both subject groups perhaps Parkinson's patients recruit alternate functional circuitry in preference to the dysfunctional basal ganglia-thalamo-cortical system.

7.4 Conclusion

The two experiments conducted above, using Parkinson's patients and the 1.5T MRI scanner, found evidence suggesting that Parkinson's patients use a different cortical network to process inhibition stimuli than controls. A separate finding was that the basal ganglia in these patients seems functionally impaired during a motor switching task. This chapter concludes the study of Parkinson's disease within this thesis. The next chapter discusses the echo-planar imaging sequence, which was used in both the previous studies and is relevant to the second project in this thesis: the feasibility of fMRI at 4.7T.

7.5 Endnotes

1. By using the less-affected hand, Parkinson's patients are less likely to experience tremor-related false button presses and are more likely to be able to respond within the required 1 sec time window.

2. The term canonical refers to conforming to orthodox or well-established patterns. In the context of SPM, the canonical hemodynamic response function is a model of the "typical" hemodynamic response.

3. Both fitted and adjusted data are adjusted for user-specified confounds (contrasts given a "0" weighting) and both have been globally normalized. The difference is that the adjusted values contain any residual errors, i.e., if

   $Y = Xb + e$

   where $X =$ $[X0\ X1]$ and $X1$ = effects of interest and $X0$ confounds
   $b =$ $[b0\ b1]$
   then

   $Y\_fitted = X1b1$ (red line)

   $Y\_adjusted = Y\_fitted + e$ (blue line)

4. Temporal smoothing.

   Data is correlated temporally because the hemodynamic response function lasts much longer than the repetition time. Therefore, subsequent data samples in time, from the same voxel, are related to each other. SPM however, remains unaware of this temporal autocorrelation; therefore, if no correction is made, statistical results are larger than they should be. Although we know that autocorrelation exists, we do not know the exact form (since it would vary across subjects for example). Therefore an autocorrelation is imposed that has either a Gaussian or hrf form. This autocorrelation may also be interpreted as a temporal low pass filter that attenuates high frequency noise.

7.6 References

http://ric.uthscsa.edu/projects/talairachdaemon.html

http://www.fil.ion.ucl.ac.uk/spm/ (SPM99)

Beiser, D.G., Houk, J.C. Model of cortical-basal ganglionic processing: encoding the serial order of sensory events. J Neurophysiol 79:3168-88 (1998)

Brooks, D.J. Advances in imaging Parkinson's disease [Review]. Curr Opin Neurol 10:327-31 (1997)

Brooks, D.J., Ibanez, V., Sawle, G.V., Quinn, N., Lees, A.J., Mathias, C.J., et al. Differing patterns of striatal 18F-dopa uptake in Parkinson's disease, multiple system atrophy, and progressive supranuclear palsy Ann Neurol 28:549-55 1990

Callicott J.H., Mattay, V.S., Bertolino, A., Finn, K., Coppola, R., Frank, J.A., et al. Physiological characteristics of capacity constraints in working memory as revealed by functional MRI. Cereb Cortex 9:20-26 (1999)

Cunnington, R., Lalouschek, W., Dirnberger, G., Walla, P., Lindinger, G., Asenbaum, S., Brucke, T., Lang, W. A medial to lateral shift in pre-movement cortical activity in hemi-Parkinson's disease. Clincal Neurophysiology 112:608-618 (2001)

Dagher, A., Owen, A., Boecker, H., Brooks, D.J. The role of the striatum and hippocampus in planning – A PET activation study in Parkinson's disease. Brain 124:1020-1032 (2001).

Deiber, M.P., Pollak, P., Passingham, R., Landais, P., Gervason, C., Cinotti, L. Thalamic stimulation and suppression of Parkinsonian tremor: evidence of a cerebellar deactivation using positron emission tomography. Brain 116:267-79 (1993)

Franz, E.A., Miller, J. Effects of response readiness on reaction time and force output in people with Parkinson's disease. Brain 125: 1733-1750 (2002)

Garavan, H., Ross, T. J., Stein, E. A. Right hemispheric dominance of inhibitory control: An event-related functional MRI study. Proc. Natl. Acad. Sci. USA (1999) 96:8301-8306

Haslinger, B., Erhard, P., Kampfe, N., Boecker, H., Rummeny, E., Schwaiger, M., Conrad, B., Ceballos-Baumann A.O. Event-related functional magnetic resonance imaging in Parkinson's disease before and after levodopa. Brain (2001) 124:558-570.

Jahanshahi, M., Jenkins, I.H., Brown, R.G., Marsden, D., Passingham, R.E., Brooks, D.J. Self-initiated versus externally, triggered movements. I. An investigation using measurement of regional cerebral bllod flow with PET and movement-related potentials in normal and Parkinson's disease subjects. Brain 118:913-933 (1995)

Josephs, O., Turner, R., Friston, K. Event-Related fMRI. Human Brain Mapping 5:243-248 (1997)

Josephs, O., Henson, R.N.A. Event-related functional magnetic resonance imaging: modeling, inference and optimization. Phil. Trans. R. Soc. Lond. B 354:1215-1228 (1999)

Jueptner, M., Weiller, C. A review of differences between basal ganglia and cerebellar control of movements as revealed by functional imaging studies. Brain 121:1437-1449 (1998)

Konishi, S., Nakajima, K., Uchida, I., Sekihara, K., Yasushi, M. No-go dominant brain activity in human inferior prefrontal cortex revealed by functional magnetic resonance imaging. European Journal of Neuroscience 10(3):1029 (1998)

Liddle, P.F., Kiehl, K.A., Smith, A.M. Event-Related fMRI Study of Response Inhibition. Human Brain Mapping 12:100-109 (2001)

Mattay, V.S., Tesitore, A., Callicott, J.H., Bertolino, A., Goldberg, T., Chase, T.N., Hyde, T.M., Weinberger, D.R. Dopaminergic Modulation of Cortical Function in Patients with Parkinson's Disease. Ann Neurol 2002;51:156-164
Menon, V., Glover, G.H., Pfefferbaum, A. Differential activation of dorsal vassal ganglia during externally and self paced sequences of arm movements. NeuroReport 9:1567-1573 (1998)

Menon V, R.T. Anagnoson, Glover, G.H., Pfefferbaum, A. Basal ganglia involvement in memory-guided movement sequencing. NeuroReport 11:3641-3645 (2000).

Nolte, J. The Human Brain. An Introduction to Its Functional Anatomy. 5th Edition copyright 2002 by Mosby Inc.

Owen, A.M., Doyon, J., Dagher, A., Sadikot, A., Evans, A.C. Abnormal basal ganglia outflow in Parkinson's disease identified with PET. Implications for higher cortical functions. Brain 121:949-965 (1998)

Parent A., Hazrati, L.N. Brain Res Brain Res Rev 20:1-127 (1995*)*

Playford, E.D., Jenkins, I.H., Passignham, R.E., Nutt, J., Frackowiak, R.S.J., Brooks, D.J. Impaired Mesial Frontal and Putamen Activation in Parkinson's Disease: A Positron Emission Tomography Study. Annal of Neurology 32(2):151-161 (1992)

Poldrack, R.A., Prabhakaran, V., Seger, C.A., Gabrieli, J.D. Striatal activation during acquisition of a cognitive skill. Neuropsychology 13: 564-74 (1999)

Rascol, O., Sabatini, U., Fabre, N., Brefel, C., Loubinoux, I., Celsis, P., Senard, J.M., Montastruc, J.L., Chollet, F. The ipsilateral cerebellar hemisphere is overactive during hand movements in akinetic Parkinsonian patients. Brain 120:103-110 (1997)

Rorden, C., Brett, M. (2000). Stereotaxic display of brain lesions. Behavioural Neurology, 12, 191-200.

Rowe, J., Stephan, K.E., Friston, K., Frackowiak, R., Lees, A., Passingham, R. Attention to action in Parkinson's disease. Impaired effection connectivity among frontal cortical regions. Brain 125:276-289 (2002)

Sabatini, U., Boulanouar, K., Fabre, N., Martin, F., Carel, C., Colonnese, C., Bozzao, L., Berry, I., Montastruc, J.L., Chollet, F., Rascol, O. Cortical motor reorganization in akinetic patients with Parkinson's disease – A functional MRI study. Brain (2000) 123:394-403

Samuel, M., Ceballos-Baumann, O., Blin, J., Uema, T., Boecker, H., Passingham, R.E., Brooks, D.J. Evidence for lateral premotor and parietal overactivity in Parkinson's disease during sequential and bimanual movements - a PET study. Brain 120:963-976 (1997)

Scholz, V.H., Flaherty, A.W., Kraft, E., Keltner, J.R., Kwong, K.K., Chen, Y.I., Rosen, B.R., Jenkins, B.G. Laterality, somatotopy and reproducibility of the basal ganglia and motor cortex during motor tasks. Brain Research 879 (2000) 204-215

Squire, L.R., Zola-Morgan, S. Structure and function of declarative and nondeclarative memory systems. [Review]. Proc Natl Acad Sci USA 93:13515-22 (1996)

Tzourio-Mazoyer N et al. Automated anatomical labelling of activations in spm using a macroscopic anatomical parcellation of the MNI MRI single subject brain. Neuroimage 2002; 15: 273-289.

Thesen, S., Heid, O., Mueller, E., Schad, L.R. Prospective Acquisition Correction for Head Motion With Image-Based Tracking for Real-Time fMRI. Magnetic Resonance in Medicine 44:457-465 (2000)

Talairach, P., Tournoux, J. 1988. A Stereotactic Coplanar Atlas of the Human Brain. Stuttgart, Thieme.

Chapter 8

Echo-Planar Imaging

8.1 Introduction

Most functional magnetic resonance imaging studies use the echo-planar imaging sequence. This chapter looks at both the advantages offered and the drawbacks to using this fast-imaging technique. The chapter begins by discussing the necessity of fast imaging. Next, the EPI sequence is described, both in general and in terms of some of the different variations that are possible. Finally, the chapter looks at some of the negative effects that EPI is susceptible to, including ghosting, distortions and acoustic noise.

8.2 The necessity of "fast" imaging techniques

Almost all functional magnetic resonance imaging utilizes fast-imaging techniques such as echo-planar imaging (EPI). There are several reasons for this choice. As mentioned in Chapter 4, long epoch durations, and long paradigms themselves, can lead to boredom, habituation and fatigue. By acquiring images quickly, one minimizes the impact of these confounds on subject performance.

Long experiments also lead to restlessness. Spatial resolution is typically about 1-2mm, thus functional imaging is particularly sensitive to subject head motion - prevalent despite the use of head restraints. The longer an experiment, the more likely gross movement will occur, whether accidental, due to patient discomfort, etc.

Any functional imaging sequence must sample the hemodynamic response across the entire brain as synchronously as possible. Because the hemodynamic response typically peaks at 4-6 seconds after neuronal activation and dies out after about 10sec, and given the additional constraint that good resolution whole head imaging requires 20-30 slices, a fast acquisition technique is essential.

Despite the obvious advantages of fast imaging techniques, BOLD imaging is still possible using slower methods such as the gradient echo technique. For example, both gradient echo EPI (GE-EPI), and gradient echo imaging are sensitive to T_2* BOLD effects. In addition, the penalty of the high temporal resolution afforded by EPI, is an increased vulnerability to magnetic inhomogeneity effects (Section 8.2). In rare circumstances, gradient echo imaging may be a suitable alternative to GE-EPI – say if the magnetic field inhomogeneity is particularly poor, even after shimming$_2$, and only a few slices and not the whole brain are to be imaged.

8.3 The Basics of Echo-Planar Imaging

8.3.1 Comparing EPI and GE sequences

In sections 1.3.1 and 1.4.2 conventional single echo imaging techniques were described wherein one echo was formed, or equivalently one line of k-space data acquired, for each r.f. pulse. In gradient echo sequences, this is accomplished by gradient reversal. In single shot EPI (ssEPI), all of the data necessary to form an image (<u>all</u> of the lines in k-space) are collected after a single r.f. pulse, by forming repeated gradient echoes using back-to-back gradients of alternating polarities (figures 8-1, 2-18, 2-19, 2-20).

8.3.2 Diversity of EPI Sequences

There are many variations of EPI sequences including multishot vs. single-shot, different k-space trajectories, and spin-echo vs. gradient echo EPI. Each approach has its own advantages; however, within the context of this thesis, only the final comparison will be explored – spin echo vs. gradient echo EPI.

8.3.2.1. Spin Echo vs. Gradient Echo EPI

The difference between SE and GE EPI sequences is the addition of a 180° (or π) refocusing pulse within the SE technique (see figures 8-1, 8-2). The characteristics of the two sequences reflect the differences between spin-echo and gradient echo images (discussed in section 1.3.1). To recap, SE refocuses static inhomogeneities, or T_2' effects producing T_2 contrast while GE is sensitive to these inhomogeneities, doesn't refocus them, and therefore its images display a T_2* contrast.

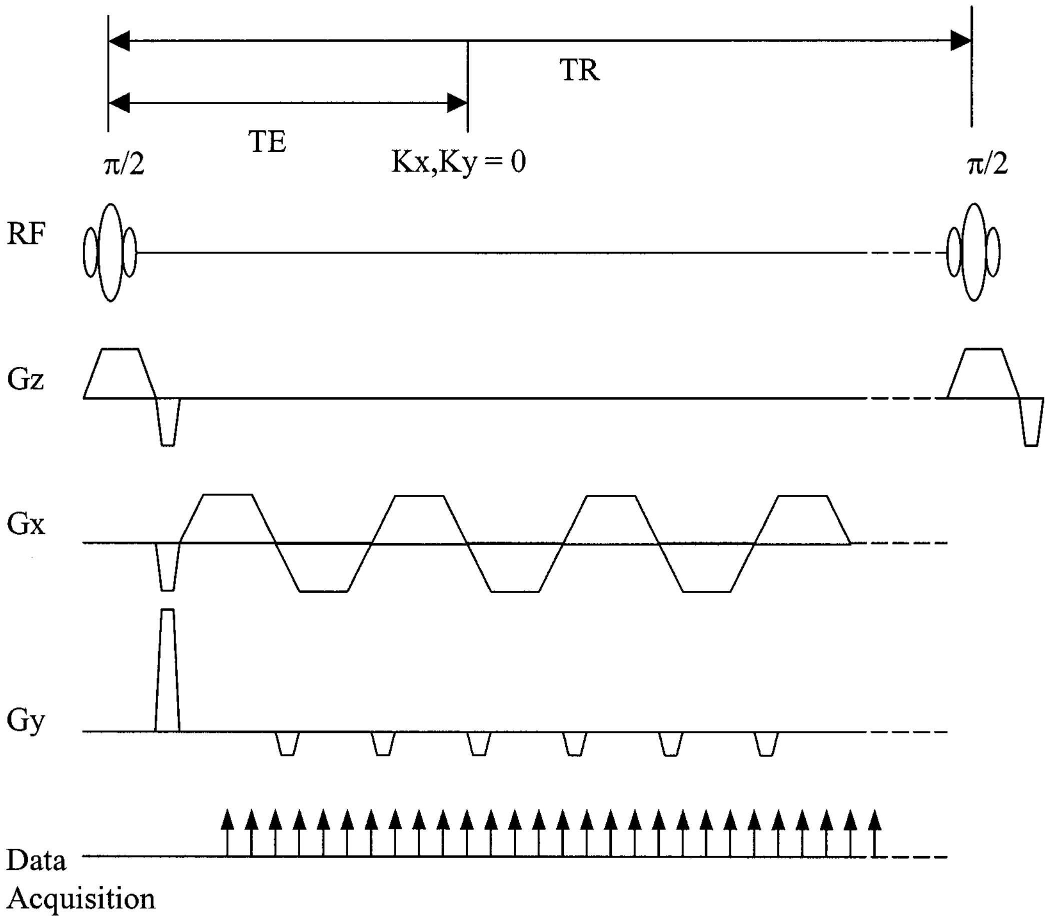

Figure 8-1. Pulse Sequence for Gradient-Echo EPI (GE-EPI).

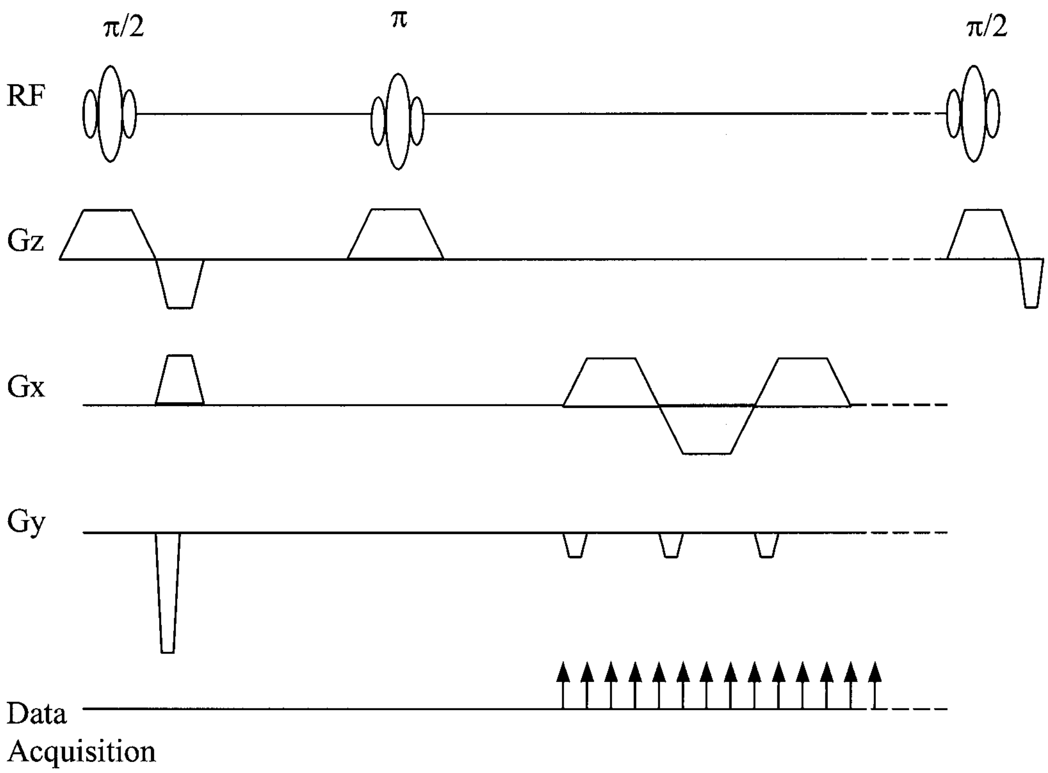

Figure 8-2. Pulse Sequence for Spin-Echo EPI (SE-EPI).

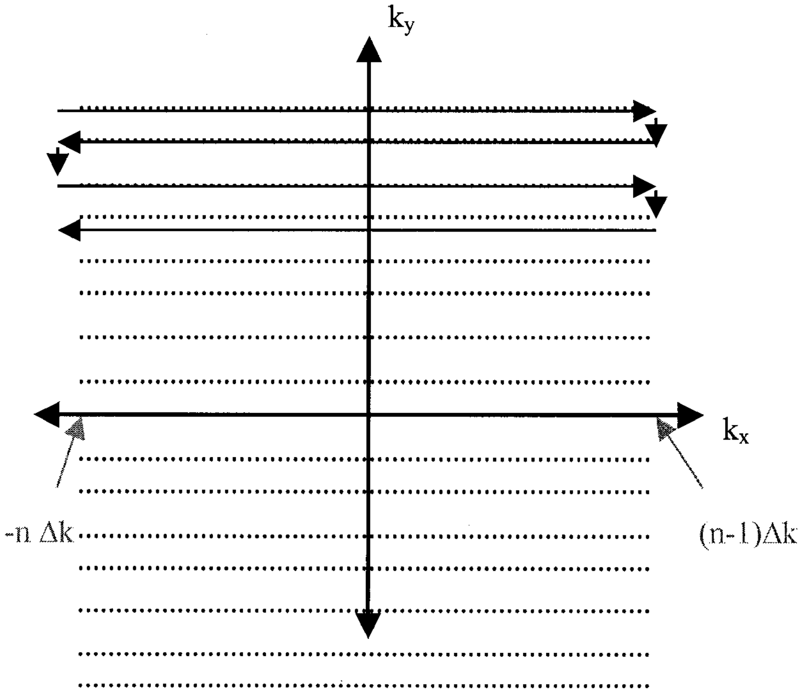

Figure 8-3. K-space trajectory corresponding to the EPI sequences of both figures 8-1 and 8-2.

8.3.3 Temporal Data Reversal

The alternating gradient polarities, illustrated as alternating direction traversal of k-space, require that the data from every 2nd line in k-space be temporally reversed. Suppose that in accordance with figure 8-3, the data are sampled in 2n equally spaced (Δk) steps. Under a positive readout gradient, the top line is sampled in the order of -n Δk to (n-1)Δk. The adjacent line, a product of a negative polarity gradient, first samples (n-1)Δk and proceeds to -n Δk, i.e., in the reverse order! (figure 8-4) The final data however, must cover k-space from left to right. Consequently, prior to image reconstruction, every alternate line must be temporally reversed.

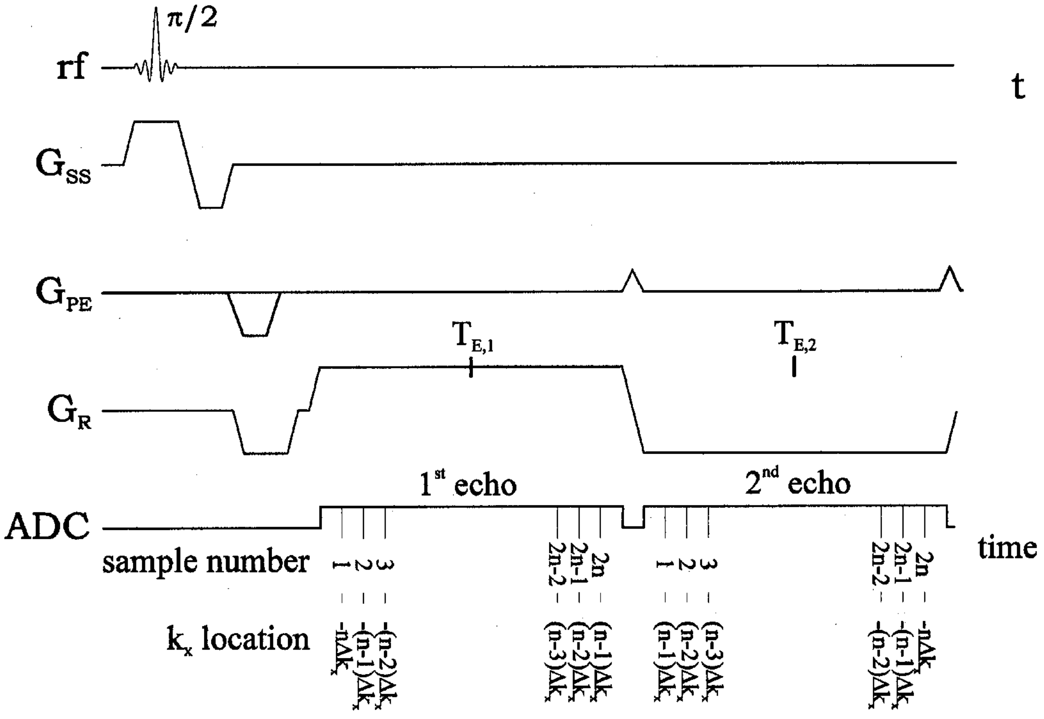

Figure 8-4. The initial portion of a gradient-echo echo planar imaging sequence, illustrating that alternating echoes collect k-space data in a temporally reversed manner (Magnetic Resonance Imaging p.521)

8.3.4 EPI Image Contrast

The contrast of a GE-EPI image is given by

$$\rho(r) = \rho_0(r)\exp(-T_{E,k=0} / T_2^*(r))[1-\exp(-TR / T_1(r))] \qquad (1)$$

where ρ_0 = spin density
$T_{E,k=0}$ = the effective echo time$_1$.

8.3.5 Tradeoffs involved in Parameter Selection

In magnetic resonance imaging, selecting parameter values is not a trivial process and instead requires careful weighting of the advantages and disadvantages afforded by a particular set of values. The tradeoffs are evident through several mathematical equations describing phenomena such as the minimum sampling bandwidth and the signal to noise ratio and are also influenced by the limitations of the imaging hardware such as the maximum gradient amplitudes. This section introduces the decision making process involved in choosing parameter values for a particular experiment. Some of the relevant equations to consider are:

$$BW_{sampling} = 1/\Delta t \geq \gamma G FOV \qquad (2) \qquad \text{(Frequency sampling)}$$

where G = readout gradient amplitude
FOV = field of view

$$SNR \sim M_0 B_T \Delta x \Delta y \Delta z (N_{phase} N_{freq} N_{av} / BW_{sampling})^{1/2} \qquad (3)$$

where M_0 = available magnetization and is determined by the spin density and also by the energy difference between the parallel and antiparallel spin states (which in turn determines the relative proportion of parallel to antiparallel spins)
B_T = the reception quality of the reception coil. Alternatively, by reciprocity this can be thought of as the transverse field amplitude created by the receive coil, per unit current.
$\Delta x \Delta y \Delta z$ = the voxel volume
N_{phase}, N_{freq} = the number of points sampled in the phase and readout (frequency encoding) directions respectively.
N_{av} = the number of averages used to generate an image

and (1) above, which describes image contrast.

To illustrate the process of choosing parameters, suppose that the issue at hand was how large to make the frequency encoding bandwidth. Suppose that the BW was set by default to equal γG_{max}FOV, with FOV = 200mm to cover the entire head. What would happen if one was to reduce the BW? By Eqn (2) the Nyquist criterion would not be met, resulting in aliasing unless γG_{max}FOV was reduced. Since the whole head must be imaged, FOV cannot change, and instead G must be reduced from G_{max}. This is fine; however, the reduction in BW is reciprocated as an increase in Δt. Increasing Δt, increases the length of the echo train and consequently enlarges both the echo time and the minimum TR. A longer TR increases the overall scan time while, by Eqn (1), changes to both TE and TR alter the image contrast. Finally, by Eqn (3), this change in BW has increased the SNR. Thus, in this particular example, it was shown that reducing the bandwidth increased SNR but at the cost of an increased scan time, and a slightly altered contrast. Furthermore, as shown in Figure 8-5 and discussed below, decreasing the bandwidth, increases the images' susceptibility to geometric distortion effects.

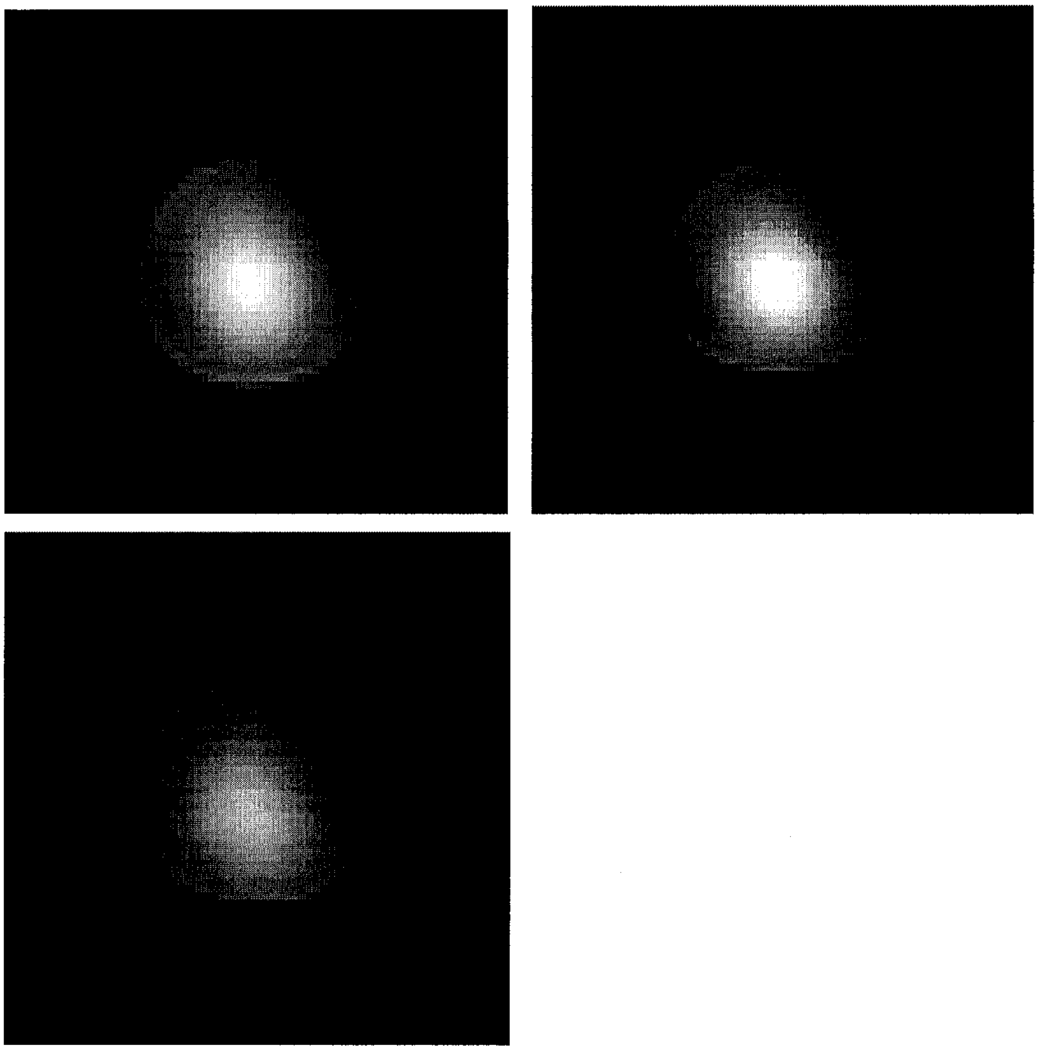

Figure 8-5. The effects of changing image bandwidth while maintaining a constant FOV. The images were acquired consecutively in an identical magnetic environment. They were collected at 125kHz, 80kHz and 50kHz and had corresponding echo times of 22.8ms, 31.1ms and 46.8ms (in the order top right, top left and then bottom). Note both the increase in geometric distortion and the slight change in image contrast that results as the BW is decreased.

8.4 Distortions and Ghosting

This section is meant only to act as an overview concerning distortions in EPI imaging. Therefore only the most common distortions, and only some of their causes are explained below. For more details see Magnetic Resonance Imaging – Physical Principles and Sequence Design or Echo-Planar Imaging Theory, Technique and Application. (cited in section 8.8).

8.4.1 Nyquist Ghosting - Introduction

Two characteristics of EPI, the alternating polarity gradients necessitating time reversal, and the long readout time following a single r.f. pulse, make it uniquely susceptible to certain image artifacts. In the presence of magnetic inhomogeneities, the time reversal brings about variations in the raw or k-space data from one line to the next. This zig-zag variation in k-space generates a low intensity duplicate of the image, shifted by half the field of view, known as an Nyquist ghost (figure 8-6).

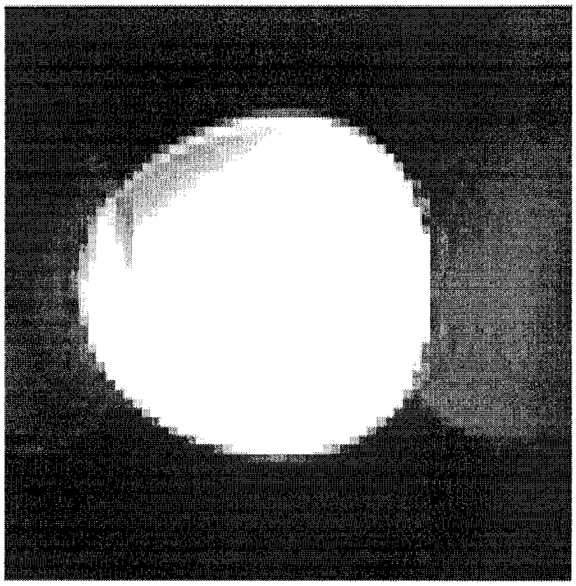

Figure 8-6. This is a cross-section of a cylindrical fluid-filled container in a non-uniform (not yet shimmed) magnetic field. The image shows two effects: Nyquist ghosting and geometric distortion (discussed below).

8.4.2 Causes of Nyquist Ghosting

8.4.2.1 Phase Errors

Imagine that an undesirable global field gradient, G', exists along the readout (RO) axis ($G'<0$). Practically this could arise from 1-D eddy currents or local inhomogeneities. This gradient causes a shift in k-space given by

$$\Delta k_{shift,q} = (-1)^q \gamma G' T_{E,q} \qquad (4)$$

where q indicates the q^{th} echo

$T_{E,q}$ = the echo time of the q^{th} echo.

Note that the shift is in opposite directions for even and odd echoes (figure 8-7, 8-8). This is because although G' is constant, all of the odd data must be temporally reversed

(8.3.3), thereby reversing the direction of this shift as well. This Δk shift is manifested as a linear phase shift if the image is reconstructed 1 dimensionally (with no phase encode (PE) gradient).

This shift may be removed either by phase subtraction or by the addition of a counteracting gradient G'' = -G'. The former is carried out by mapping the phase modulation using a navigator scan (i.e. a prescan without phase encoding). However, if the gradient is spatially variable$_3$ or localized, then the correction will not be entirely successful. If no correction is attempted, this oscillating phase results in Nyquist ghosting in the final image

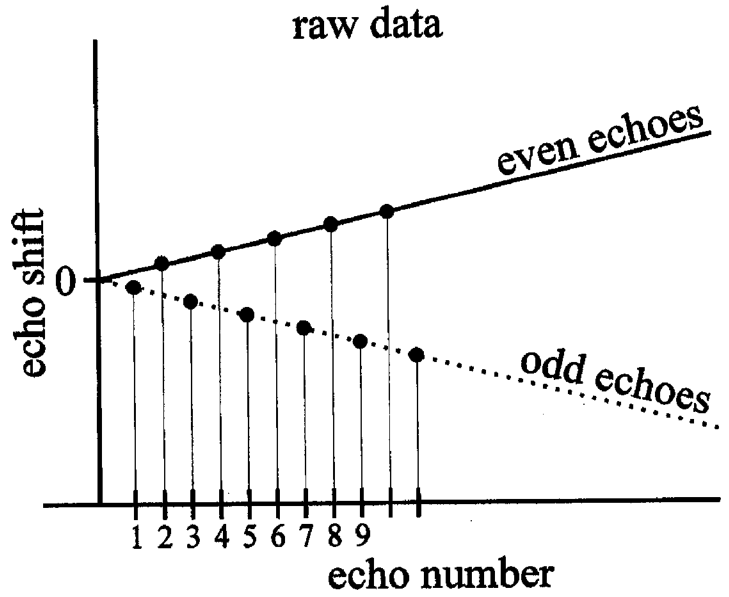

Figure 8-7. The phase oscillations (from even to odd echoes) caused by a gradient-induced shift in k-space (Magnetic Resonance Imaging p.547).

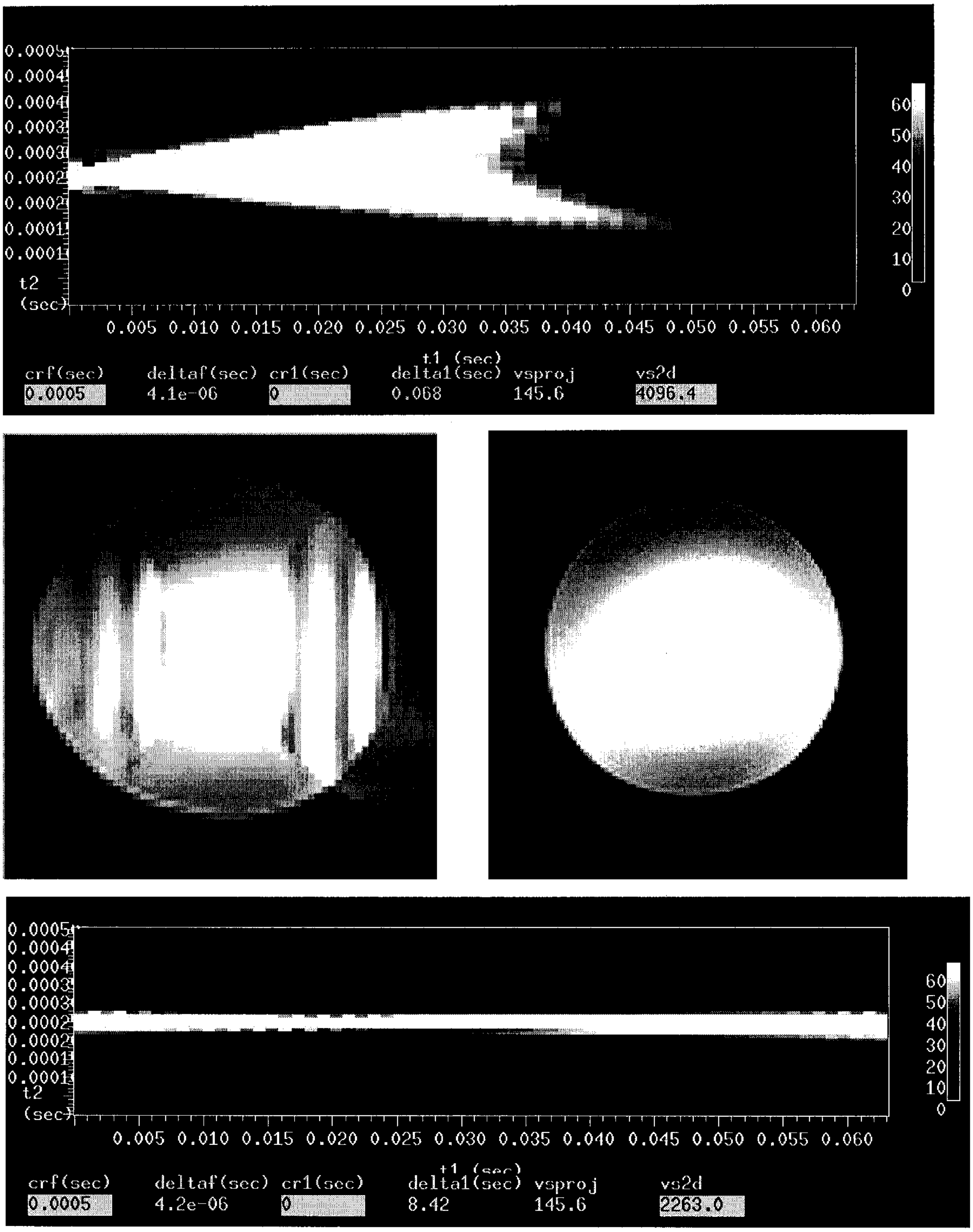

crf(sec)	deltaf(sec)	cr1(sec)	delta1(sec)	vsproj	vs2d
0.0005	4.1e-06	0	0.068	145.6	4096.4
0.0005	4.2e-06	0	8.42	145.6	2263.0

Figure 8-8. Raw EPI data in the absence of a phase encoding gradient - before shimming and uncorrected (top) and corrected by both extensive shimming and the addition of a compensatory gradient (bottom). The types of images that result from such magnetic environments are shown in the middle (middle left corresponds to the top image's environment, and middle right to that of the bottom image). Note both the geometric distortion and the ghosting artifact in the image resulting from the unshimmed environment without the compensatory gradient.

8.4.2.2 Eddy Currents

Recall Faraday's Law of induction, namely,

$$emf = -d\Phi / dt \qquad (5)$$

where Φ = the magnetic flux through a coil, which in turn is given by

$$\Phi = \int_{\text{coil area}} \mathbf{B} \bullet \mathbf{ds}. \qquad (6)$$

By Lenz's law, the current induced in a coil, generates a magnetic field opposing that which created it.

In the context of EPI, rapidly switching gradients induce so-called eddy currents in nearby conductors including the r.f. coils and electromagnetic and thermal shielding. Mathematically, this can be seen by combining Eqns (5) and (6),

$$emf = -\int_{\text{coil area}} \mathbf{dB/dt} \bullet \mathbf{ds} \qquad (7)$$

Eddy currents produce fields that oppose the gradient fields, therefore they both reduce the perceived gradient amplitude and introduce a delay between the application of the voltage driving a gradient and the appearance of the resultant gradient magnetic field as seen by the sample. The amplitude reduction is easy to compensate for. The delay, however, cannot be corrected so easily.

In the event that a time delay is created between the current driving a coil, and its subsequent gradient waveform, each echo will refocus late. Reversal of alternate echoes shifts every 2nd line in k-space such that they refocus early (figure 8-9). This k-space modulation induces ghosting.

The solution is to shift the analog to digital converter raster in time to match the new, delayed gradient field waveform, i.e., to capture the echoes in the absence of any delay. However, the ghosting can only be completely removed if the same temporal shift occurs across the image (which typically requires a match in symmetry between the coil and eddy currents), otherwise regional ghosts will persist.

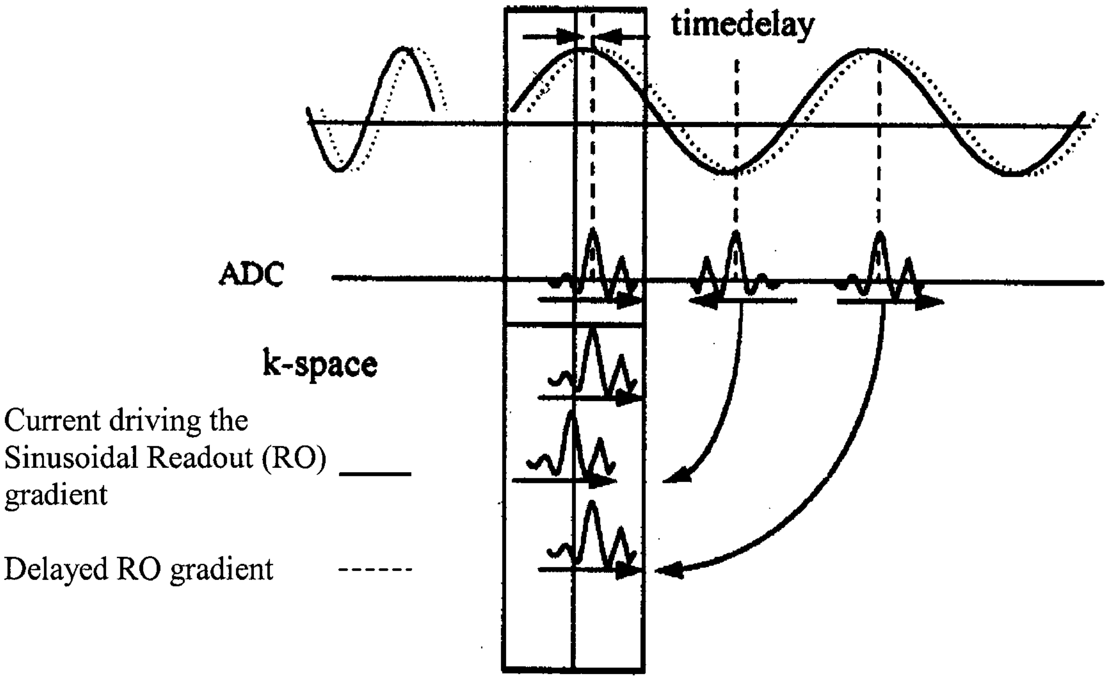

Figure 8-9. A delay between the gradient field and the ADC (analog to digital conversion) timing leading to Nyquist ghosts. Time reversal changes this delay from a lag to a lead for alternate echoes, creating a zigzag across k-space (Schmitt, F. Chapter 6).

8.4.3 Low Bandwidth Distortions

The normalized EPI free induction decay (figure 8-10) is characterized by

$S(t) = \int \rho(r)\exp(i\varphi)\exp(-t/T_2^*)d^3r$ (8) (Schmitt, F. Chapter 6)

where ρ = spin density
φ encompasses off-resonance effects. That is,

$\varphi = (\delta\omega + \gamma\Delta B_0)t + \gamma r\int G(t')dt'$ (9)

where $\delta\omega$ = chemical shift effects (see below)
ΔB_0 = field inhomogeneities
$\gamma r\int G(t')dt'$ = encoding gradients.

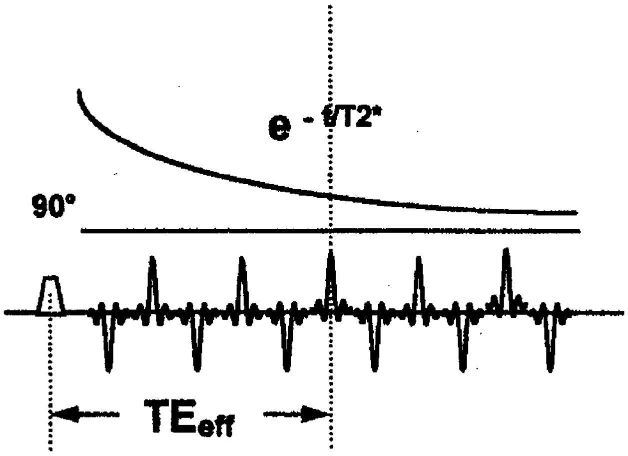

Figure 8-10 The free induction decay (FID) from a GE-EPI pulse sequence.

By introducing the substitution,

$k = \gamma\int G(t')dt' = \gamma Gt$ (for constant amplitude gradients) (10)

and accounting for a finite sampling window, Eqn (8) may be expanded for the 1 dimensional case (x axis only) as

$S'(k(t)) = \mathrm{rect}(t/T) \int \rho(x)\exp(ikx) \exp(ikd) \exp(-k/(\gamma G T_2^*))x\exp(-t/T_2^*)dx$ (11)

where $d = (\delta\omega)/(\gamma G) + \Delta B_0/G$
$\mathrm{rect}(t/T) = 1$ for $0<t<T$ and otherwise $= 0$.

In order to proceed further, two identities of the Fourier transform are required, namely that:

$F(gh) = F(g) \otimes F(h)$ (12)

$F(g(k)\exp(ikx_0)) = g'(x-x_0)$ if $F(g(k)) = g'(x)$. (13)

Finally, if T_2 is constant across space, then Eqn (11) may be solved as

$F(S'(k)) = \rho(x-d) \otimes PSF(x)_4$. (14)

This has serious implications. It states that the recorded signal is the actual spin density, displaced by "d" pixels (from off-resonance effects), and convolved with the point spread function5.

Before examining individual distortion effects, two additional definitions are required:

$$bw_{RO} = 1/T_{RO} \qquad (15)$$
$$bw_{PE} = 1/T_{acq} \qquad (16)$$

where bw = the pixel bandwidth (in the RO or PE directions)
T_{RO} = the readout or acquisition time (time to acquire a single k_x line)
T_{acq} = the total acquisition time (time to acquire a single k_y line)

It is important to note that $b_{RO} >> b_{PE}$. For example, if T_{RO} = 0.6ms and T_{acq} = 128 lines * 0.6ms = 76.8ms, the resulting pixel bandwidths are 1667 and 13 Hz respectively. This is important because as it turns out, a low bandwidth increases the susceptibility to certain distortions - accordingly these effects will occur only in the PE direction!

8.4.3.1 Chemical Shift Effects

Earlier it was mentioned that all nuclei belonging to a chemical species have the same resonance frequency. This isn't entirely true. In fact, within a species, each nucleus has a frequency determined by its molecular environment.

Each nucleus is surrounded by an electron cloud. In the presence of a magnetic field, the electrons circulate such that by Lenz's Law, they induce a magnetic field opposing the applied one. The extent of this shielding is mediated by the local chemical surroundings (i.e. local bonds) such that

$$B_{local} = B_0(1-\sigma) \qquad (17)$$

where σ = shielding constant

In proton imaging, the consequence of this chemical shift is that fat and water protons resonate at slightly different frequencies. This can lead to distortions in which the fat signal appears spatially shifted.

Mathematically, the frequency shift, $\delta\omega$, is specified by

$$\delta\omega = \gamma\sigma B_0 \qquad (18)$$

and results in an image shift

$$d_{cs} = \delta\omega / \gamma G = \sigma B_0 / G \qquad (19)$$

which in units of pixels is

$$d_{csp} = \delta\omega / bw = \gamma\sigma B_0 / bw. \qquad (20)$$

Note that Eqns (19) and (20) predict that the largest displacement will occur in the direction of the smallest gradient or smallest pixel bandwidth (the PE direction). For example, at 1.5T the fat-water frequency difference is 210Hz. Using the bandwidths calculated above, this leads to a shift of 0.13 pixels in the readout direction, but 16.1 pixels in the phase encode direction.

Chemical shift artifacts (from fat) can be avoided by using fat suppression pulse sequences.

8.4.3.2 Geometric Distortions

Geometric distortions are caused by magnetic field inhomogeneities. Excellent shimming is therefore critical in minimizing image distortion. Possible sources of inhomogeneities include imperfections in the main magnetic field even after shimming, and magnetic susceptibility effects. Recapping section 3.2, magnetic susceptibility describes the response of a substance to an applied magnetic field. That is,

$$B = (1 + \chi)\mu_0 H \qquad (21)$$

where μ_0 = magnetic constant (the permeability of space)
H = the magnetic field strength
B = the magnetic flux density
χ = magnetic susceptibility parameter.

A susceptibility-based magnetic field difference is established at the physical intersection of two different materials,

$$\Delta B_0 = (\chi_1 - \chi_2)B_0. \qquad (22)$$

Whereas chemical shift occurs uniformly in space, susceptibility differences are highly localized. Hence, as opposed to causing global image shifts, they stretch or compress parts of an image (figure 8-5). The regional displacement due to these effects is

$$d = \Delta B_0 / G = \gamma \Delta B_0 / bw. \qquad (23)$$

There are several implications from the above equations. Equation (23) illustrates that the distortion is greatest along the axis with the smallest pixel bandwidth or gradient amplitude - the PE direction. Equation (22) cites the effect's dependence on magnetic field strength; accordingly, geometric distortion will be much more severe at 4.7T than at 1.5T.

Tied to the stretch or compression is a corresponding intensity change. The local pixel intensity corresponds to the volume from which a signal arises. Therefore, a voxel stretch, for example, results in a larger than normal pixel area to signal source ratio or a lower signal than normal.

Many researchers have proposed solutions to susceptibility distortions. These include thinner slices, multishot techniques, and careful slice position to avoid regions of different susceptibility.

8.5 Acoustic Noise

EPI sequences are particularly noisy, resulting from rapid gradient polarity reversals inherent to this fast imaging technique. The 1.5T clinical scanner provides a safe level of acoustic noise, provided that both earplugs and headphones are used as hearing protection; however, little was known about the acoustic noise of the 4.7T system. Therefore, an experiment was carried out to quantify the intrinsic acoustic noise of the 4.7 and 1.5 Tesla systems during scanning conditions. A software solution (Varian Programming Language) was implemented for the 4.7T system, to slow the gradient switching and thereby reduce the acoustic noise.

8.5.1 Methods

It has been shown that sound levels are greater outside the magnet than in the bore itself. (Mechefske et al. 2002). Therefore, the noise measurements were recorded using an acoustic meter placed about 1 meter in front of the centre of the bore. All tests used the body gradient coils of the respective magnets. All EPI scans were single shot. To reduce the acoustic noise, the rise time of the EPI sequence was elongated through the introduction of a multiplicative scaling factor (trise_mult) into the software code governing the EPI sequence (figure 8-11). This made the EPI train only minimally longer – to such an extent that with the parameters listed below, the total acquisition time remained unchanged after the rise time was scaled. This approach has been shown successful by others; in particular, Zhou and Ma (2000) found that selective gradient derating, namely selective gradient amplitude and rise time adjustment, reduced the sound level by 4-6 dB using FSE (fast spin echo) at 1.5T.

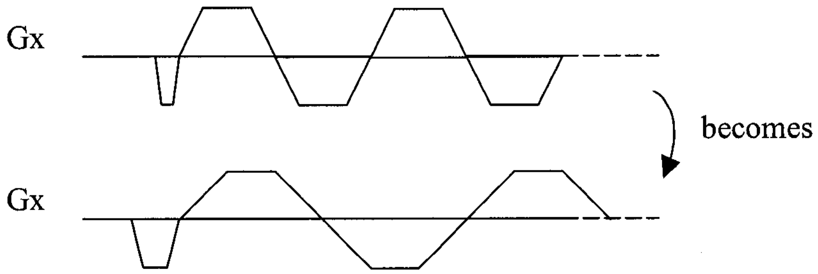

Figure 8-11 Elongating the rise time of the alternating polarity gradient in the readout direction.

8.5.2 Observations/Results

Table 8-1 summarizes the magnets' gradients' properties. Table 8-2 summarizes the parameters particular to each acoustic test (augmented parameters are listed in bold). Table 8-3 outlines the effectiveness of drawing out the gradient rise time in reducing acoustic noise.

Table 8-1. Max Gradient Strength and Rise Times for the 1.5T and 4.7T Systems

Gradient Coil	Max Amplitude (mT/m)	Rise Time (μs)	Slew rate (mT/m/ms)
Head (4.7)	55	280	196
Body (4.7)	35	240	145
Body (1.5)	40	200	200

Table 8-2. Acoustic Tests and Results

Test #	Magnet	Parameters	Acoustic Reading (dB) (Body Gradient)	Acoustic Reading (dB) (Head Gradient)
1	4.7	EPI, 64x64, TR=2sec, 200x200 mm FOV, 125kHz BW, 1 slice x 5averages, 2mm slices, axial	109	
2	4.7	EPI, 64x64, TR=2sec, 200x200 mm FOV, 125kHz BW, **25 slices** x 5averages, 2mm slices, axial	115	
3	4.7	EPI, **128x128, TR=2.25sec**, 200x200 mm FOV, 125kHz BW, **10 slices** x 5averages, 2mm slices, axial	124	119
4	4.7	EPI, 128x128, TR=2sec, **240x240 mm FOV, 200kHz BW,** 1 slice x 5averages, 2mm slices, axial	128	124
5	4.7	**Gradient Echo**, 256x256, TR=10msec, TE=5ms, 200x200 mm FOV, 100kHz BW, 1 slice, 4mm slices. 2000μs, 20° RF, axial	115	116
6	**1.5**	Diffusion Tensor (128x128)	120	
*	4.0 London	EPI, 64x64, 240x240 mm FOV, 199kHz BW,10slices/sec	117	

*Results from Mechefske et al. 2002 (Kingston/London ON) included for comparison (from Sonata body gradient set, no liner)

Table 8-3. Reduction in Acoustic Noise Achieved According to the Rise Time Elongation (by the scaling factor Trise_mult)

Test #	Previous Noise with Head Gradient (dB)	Trise_mult	New Acoustic Noise (dB)
3	≈ 123	4	112
4	≈ 127	2	120

Prevailing standards dictate that:

1) Ears should not be exposed to more than 90dB for 8 hours. (see for example http://www.hse.gov.uk/pubns/indg298.htm)

2) E-A-R foam earplugs are rated to 29 dB. If worn properly one could then tolerate 119dB without concern. The combination of earplugs and headphones do not add algebraically. The following works http://www.aearo.com/html/industrial/earlog13.htm and http://www.tkontheweb.com/support/Dual%20Hearing%20Protection.pdf suggest that dual protection may add 5-10 dB or 10 to 15 dB. Assuming 10dB extra, this would suggest that a maximum of 90dB+29dB+10dB= 129dB should be acceptable.

8.5.3 Acoustic Experiment Conclusion

Using the 4.7T whole body gradient coil, even the maximum acoustic noise (128dB) is within the safety standards, provided that dual hearing protection is used. Scaling the gradient rise times was successful in further reducing the level of noise.

8.6 Conclusion

This chapter has examined the echo-planar imaging sequence. This sequence was used in the functional studies with Parkinson's patients, because as a fast imaging method it allows for short experiment durations, thereby minimizing boredom, habituation and fatigue, as well as the likelihood or prevalence of gross subject motion and yet it samples the entire brain both as synchronously as possible, and in a reasonable amount of time. However, at higher field strengths, effects such as geometric distortion become much greater to the extent that the advantages of using EPI may be outweighed by the poor image quality (Chapter 9).

8.7 Endnotes

1. $T_{E,k=0}$ or TE_{eff} is the time during which the centre line in k-space is acquired. Many different k-space traversals exist including bottom up, top down, and centre out, which influence TE_{eff} accordingly. Since the majority of the image signal lies in the centre of k-space, the k-space path, by dictating TE_{eff} , ultimately determines the extent of the T_2* contrast weighting.

2. Shim coils are a series of independent coils used to correct magnetic field inhomogeneity. The coils are designed to produce auxiliary fields that cancel the components of the main magnetic field causing the inhomogeneity. Shimming itself is the process of determining the correct level of current to apply to each of the shim coils, in order to achieve optimal magnetic field homogeneity.

3. For example, if the offset gradient along the RO direction varies in the y-direction, then in the navigator echo image (no PE gradient), for each x point, you'd be averaging the phase along the entire y-dimension. Therefore, the single value for phase correction, calculated from the one line of data with no phase encoding, will not be able to remove all of the ghosting.

4. $PSF(x) = [\mathrm{sinc}(\gamma GTx/2\pi) \otimes (1/((1/ (\gamma GxT_2^*)^2 + x^2))]$ for GE-EPI.

5. The PSF is mathematically the outcome of imaging a point and characterizes the quality of an imaging sequence.

8.8 References

Frackowiak, R.S.J., Friston, K.J., Frith, C.D., Dolan, R.J. and Mazziotta, J.C. Human Brain Function. San Diego: Academic Press, 1997.

Haacke, E.M., Brown, R.W., Thompson, M.R., Venkatesan, R., Magnetic Resonance Imaging – Physical Principles and Sequence Design. New York: John Wiley & Sons, Inc., 1999.

Mechefske, C.K., Geris, R., Gati, J.S., Rutt, B.K. Acoustic Noise Reduction in a 4 T MRI scanner. Magnetic Resonance Materials in Physics, Biology and Medicine 13 (2002) 172-176.

Schmitt, F., Stehling, M.K., Turner, R. Echo-Planar Imaging Theory, Technique and Application. Berlin: Springer, 1998.

Zhou Y, Ma, J. Acoustic Noise Reduction in MRI by Selective Gradient Derating. International Society for Magnetic Resonance in Medicine Annual Conference 2000. p.2009

Chapter 9

Functional Imaging at 4.7T

9.1 Introduction

The effects of field strength on BOLD imaging were discussed in Section 3.4, wherein it was shown that higher fields offer greater signal-to-noise, greater functional contrast-to-noise and greater localization to the precise source of neural activity. This chapter investigates the feasibility of functional imaging at 4.7T, by demonstrating simple motor activation at this field strength and comparing it to that at 1.5T.

To recap material introduced in Section 8.2, fast imaging techniques such as EPI are the most appropriate for fMRI studies because they are least susceptible to both attentional shifts such as boredom and subject motion artifacts, while providing the best temporal resolution of the hemodynamic response function and permitting whole head imaging. Chapter 8 however, also highlighted the weaknesses of EPI including its vulnerability to magnetic field inhomogeneities, particularly in the phase encode direction – a phenomenon that single echo sequences such as gradient echo are largely immune to (discussed below).

9.2 Comparing single echo and multi-echo techniques' susceptibility to chemical shift and distortion effects.

9.2.1 Theory

In conventional single-echo imaging sequences, data for each line in the k_y or phase encode direction is sampled at the same time, TE, after an r.f. pulse. In comparison, in single-shot EPI (ssEPI) sequences (a multi-echo approach), all of the k_y lines are sampled sequentially in time following a single r.f. pulse (therefore the phase encode gradient is said to have the properties of a readout gradient).

Consider now the chemical shift or geometric distortions mentioned earlier in sections 8.3.3.1 and 8.3.3.2. Chemical environment, or localized inhomogeneities cause a frequency shift given by $\gamma\sigma B_0$, or $\gamma\Delta B_0$, respectively. In conventional single-echo techniques, the presence of a gradient-like inhomogeneity, G_y', in the phase encode direction, causes a phase shift

$$\varphi_{PE} = -\gamma G_y' y TE. \qquad (1)$$

This phase shift is the same for each line in the k_y direction, hence, this does not lead to an image shift or distortion.

Frequency encoding directions however, are susceptible to these resonant frequency-altering phenomena whether the sequence is single-echo or multi-echo. In this direction, successive data points are acquired sequentially in time, therefore each k_x point develops an increasing phase given, for example, by

$$\varphi_{RO}(t) = -2\pi\gamma(G_x x + G_x' x)t \qquad (2)$$

where G_x' = a static inhomogeneity-induced gradient in the readout direction
G_x = the spatial encoding gradient in the readout direction.

This point-to-point change in phase results in a distortion along this direction.

In ssEPI, both the readout and phase encode gradients act like frequency encoding gradients. Furthermore, as seen in equations 13 and 16 (Chapter 8), the extent of the shift/distortion is proportional to 1/bw; therefore, the effect is significantly worse in the phase encode direction than in the readout direction. Considering all this, gradient echo (GE) images are clearly more robust in the presence of inhomogeneities than ssEPI (figure 9-1).

9.2.2 Observations at 4.7T

In order to investigate the actual differences in image quality at 4.7T between the single-echo and multi-echo techniques, sample images were collected both of a fluid-filled phantom (per 1000g H_2O distilled, 1.25g $NiSO_4 \times 6H_2O$ + 5g NaCl) and in vivo, using both gradient-echo and ssEPI techniques. The data are shown in Figures 9-1 and 9-2.

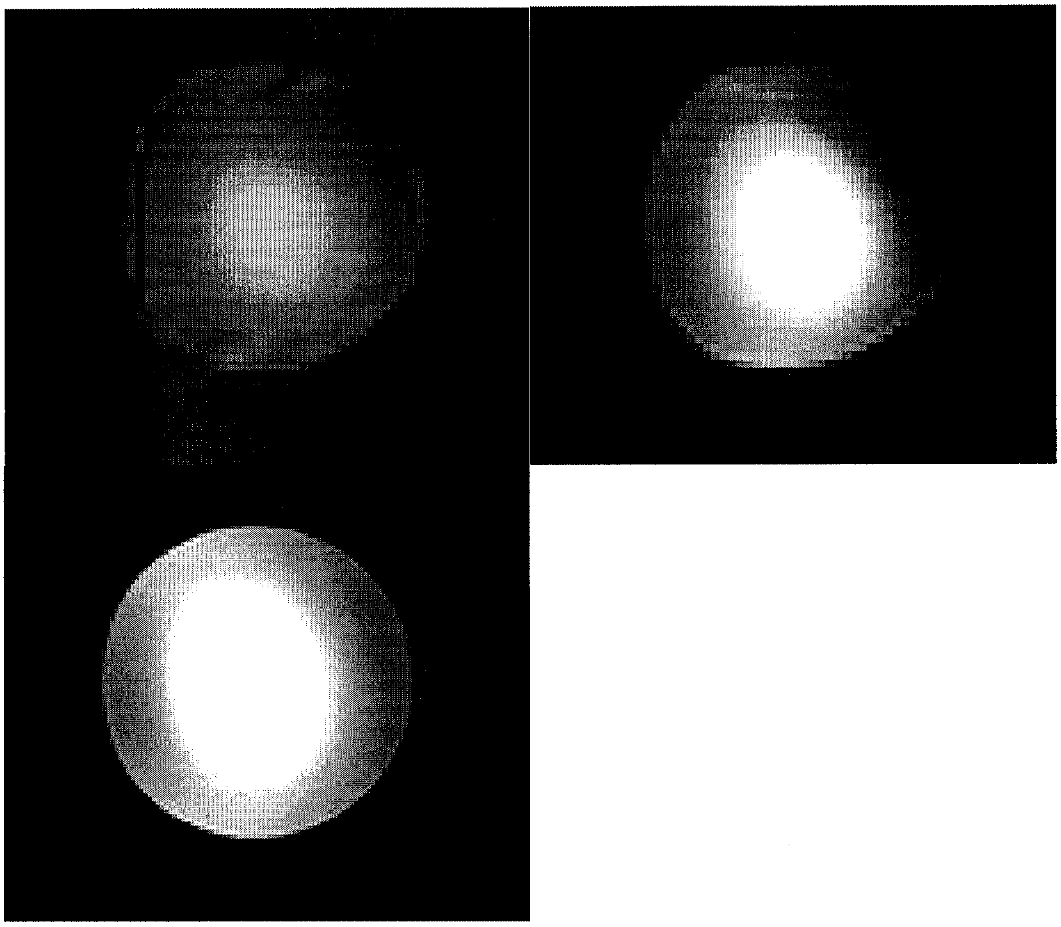

Figure 9-1. Comparing GE-EPI, SE-EPI and GE images of the same slice at 4.7T.

The images were acquired one after another, from the same phantom after manual shimming across this slice only. The images come from the following sequences: single shot, linear k-space, gradient-echo EPI (top left), single shot, linear k-space, spin-echo EPI (top right), and gradient-echo (bottom left). They are all displayed at the same intensities, and all have the same resolution and field of view (64^2 and 200x200mm respectively). Both EPI images were acquired at TR = 1000ms, and BW = 125kHz. Notice that while the spin-echo EPI technique, which refocuses static inhomogeneities (or T2' effects), clears up some of the more severe distortions of the GE-EPI sequence, it nevertheless still shows both ghosting and geometric distortion. Under the same conditions, the GE image is much better.

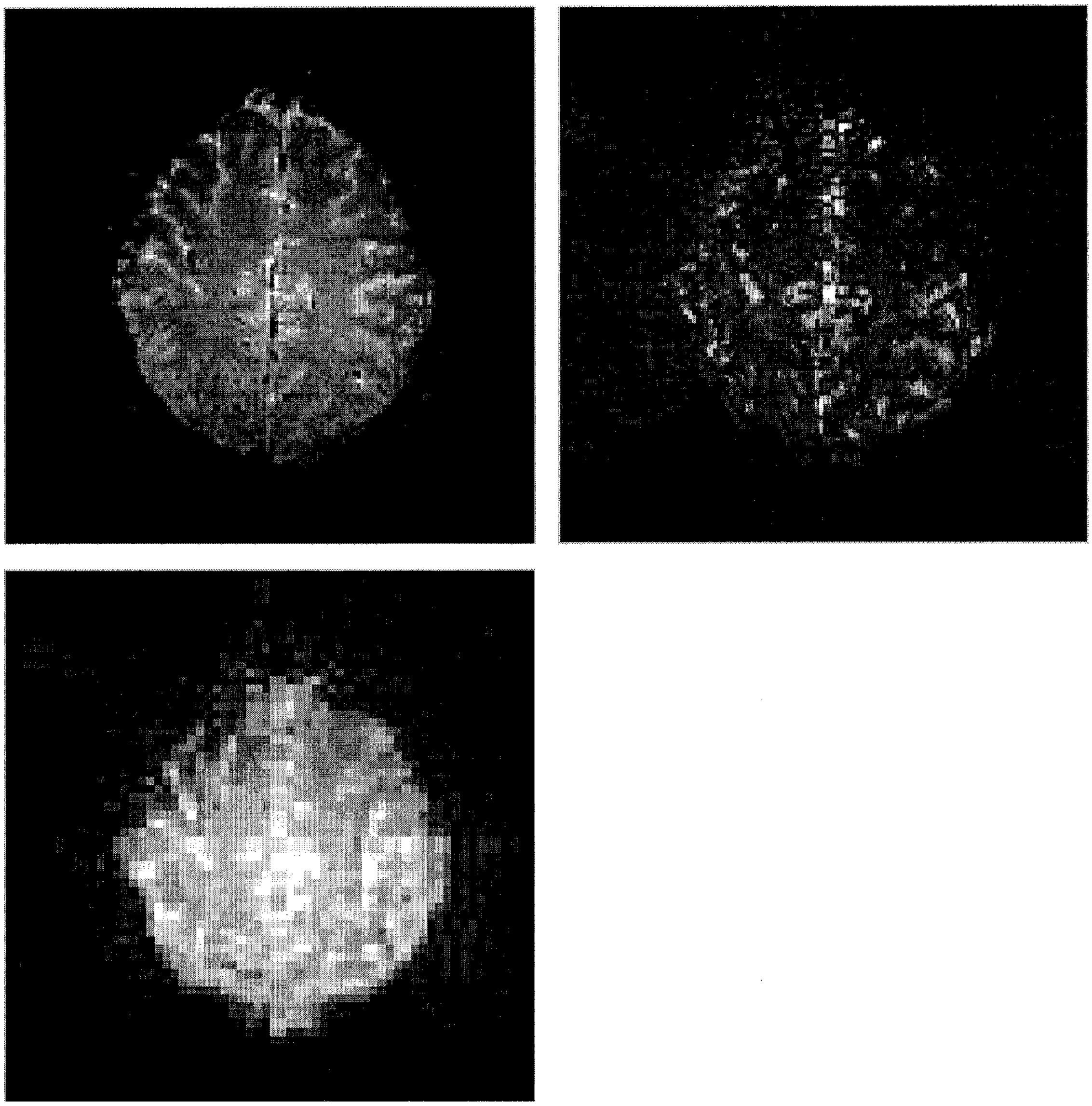

Figure 9-2. A comparison of gradient echo and echo planar in vivo images. The image on the top left is a gradient echo image (TE = 26ms, 128^2 resolution). The top right and bottom images are both gradient echo EPI images taken at 128^2 resolution and 70.8ms TE (top) vs. 64^2 resolution and 28.4ms TE (bottom) respectively. All images correspond to exactly the same slice, and were acquired in identical magnetic environments.

9.2.3 Discussion

The EPI images of the phantom and of the brain contain significant geometric distortions. These distortions are attributed primarily to the poor magnetic field homogeneity despite shimming prior to image acquisition. Shimming was extensively tested for this thesis, and it was ultimately concluded that the built-in Varian shimming program, FASTMAP, was unreliable and not suitable for shimming. It was found that manual shimming on the slice of interest itself offered better results.

Although future functional imaging research at 4.7T at the U of A will undoubtedly involve the use of EPI sequences, at the present time the magnetic field is not sufficiently uniform for this imaging modality. Images such as those seen in Figure 9-1 are the norm, and have too many distortions to be of use. Investigation of the benefits offered by functional imaging at high field, is therefore assigned to gradient echo imaging. This is a suitable choice since single-slice gradient echo imaging maintains T_2* BOLD sensitivity, and has an acceptable temporal resolution.

9.3 Comparing Functional Images from 1.5 versus 4.7 Tesla

9.3.1 Methods

9.3.1.1 Paradigm

Two healthy male subjects were scanned at both 1.5T and at 4.7T while conducting a simple motor paradigm. The paradigm consisted of 8 alternating epochs of rest and movement, each 30 seconds long. Auditory commands informed the subjects when to switch tasks. The subjects conducted right-handed, self-paced, large amplitude finger tapping during the movement condition and rested during the baseline condition. Amplitude and pace were not monitored; instead the participants were asked to perform the movements in the same manner during both scanning sessions.

9.3.1.2 Imaging Parameters

Single slice, 5mm thick gradient echo images were collected at each field strength. The position and orientation of the single slice were determined in a pilot study that is outlined below. Echo times close to the optimal (TE $\approx T_2$*) were chosen: 59 and 26 ms for the 1.5 and 4.7T magnets respectively (Gati 1997). Images were 128x128 with a 200mm FOV. Bandwidth and repetition times were 119kHz (1.5T) versus 49kHz (4.7T) and 79ms (1.5T) versus 48ms (4.7T). Inflow effects were minimized by using a low flip angle (~20°) and by adding a delay between images (1 second at 1.5T and 8 seconds_1 at 4.7T). Finally, extensive manual shimming was performed on the exact slice to be imaged, prior to data collection.

The slice position and orientation were established in a single subject, finger tapping, pilot study at 1.5T. Eight slices were scanned in the orientation shown in Figure 9-3, using gradient echo EPI with the following parameters: 5mm thickness with 1mm interslice gap, 220mm FOV, 60ms TE, TR = 2 sec, 2602 Hz/pixel, and medium smoothing. The session included seven tapping and seven rest epochs, each 30 seconds long, during which 210 volumes of data were collected. Built-in Siemens statistical software was used to analyze the data in real-time (approximately). Slices 3-6 all elicited good motor cortex activation (figure 9-4). For the high vs. low field experiments, the slice position was therefore chosen parallel to the posterior angle of the corpus callosum, and centred vertically between the corpus callosum and the top of the head (approximately slice 4 from the bottom in figure 9-4).

9.3.1.3 Statistical Pre-processing and Modeling

Fewer statistical pre-processing steps were required in the present experiment, because the analysis was conducted on a single subject and not on a group basis. This restriction removed the need to reorient each subject's head to a particular orientation, and to normalize data to a common stereotactic space. The functional images were realigned to the first volume collected, and spatially smoothed with a 4mm FWHM isotropic Gaussian kernel. The paradigm was modeled as an unconvolved boxcar. Three motion regressors (x and y translation, and yaw) characterizing each subject's movements during the scanning session were included as nuisance covariates. Images were globally scaled but were not filtered using a high-pass filter since this requires precise definition of the interscan times (TR).

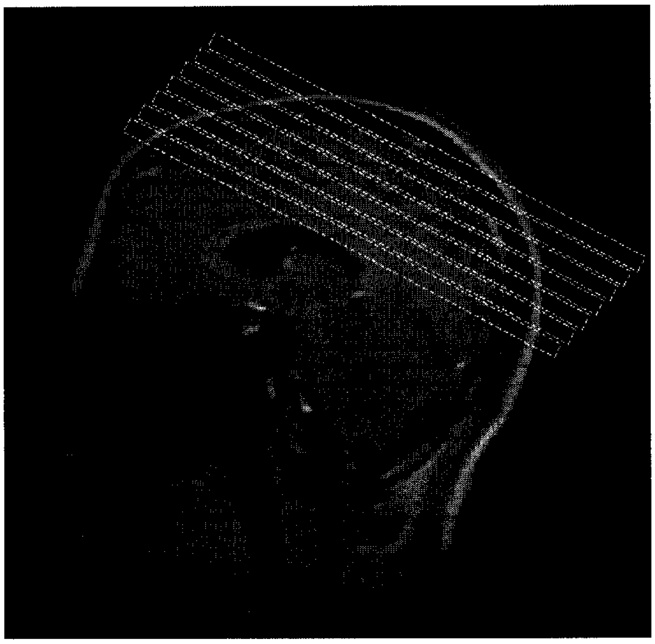

Figure 9-3. Sagittal view of the subject's head illustrating the orientation of the slices used in the 1.5T pilot study. The base slice was positioned tangentially to the corpus callosum. This internal reference allows for consistent slice positioning at the two fields.

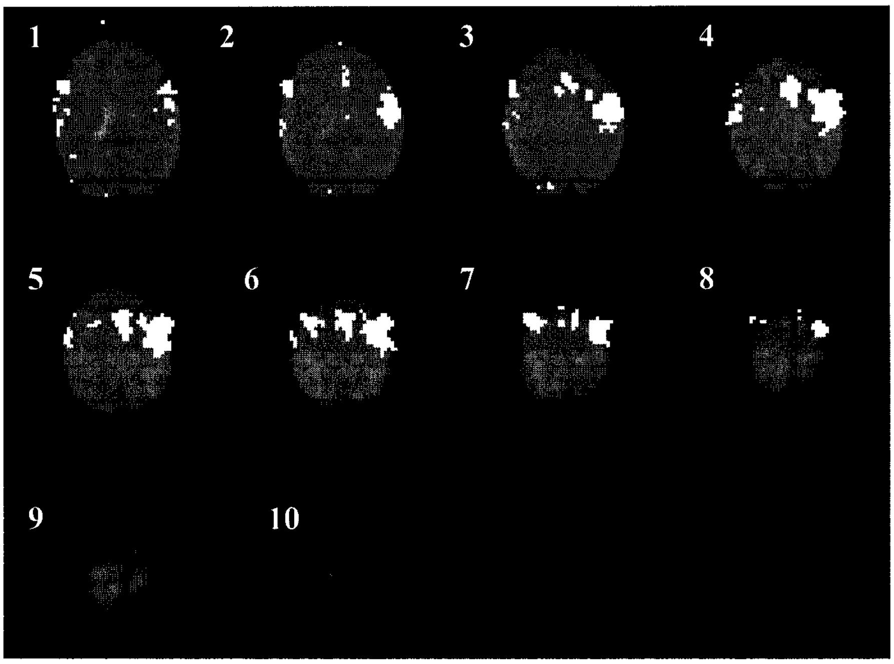

Figure 9-4. Motor Cortex activation found in the 1.5T EPI pilot study.
The slices correspond to those shown in figure 9-3. The slices are axial-oblique and radiological (i.e. the left side of the brain in the image is the patient's right side of the brain). The base slice is denoted slice 1 and the top slice 10. Of these, slices 3-6 show significant activation.

9.3.2 Results

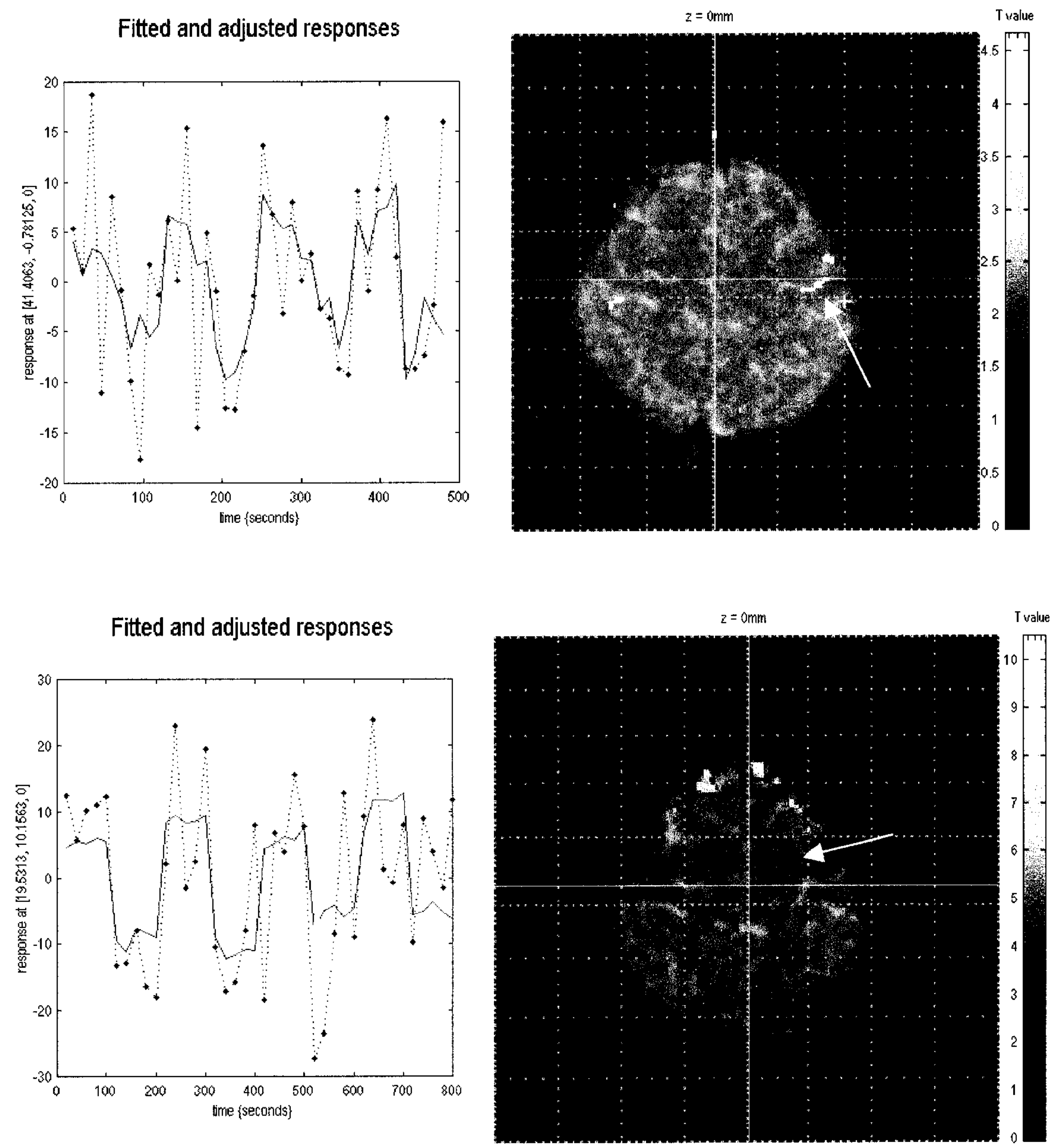

Figure 9-5. Finger tapping-induced activation at 1.5T (top) and 4.7T (bottom) for the first subject. The timecourse of an active voxel (localized by the arrow) is shown on the left. This is the voxel's signal intensity over time, normalized by the mean image voxel intensity. The two timecourses were selected from analogous regions of the brain. Note the difference in the scale of the y-axis on the two graphs.

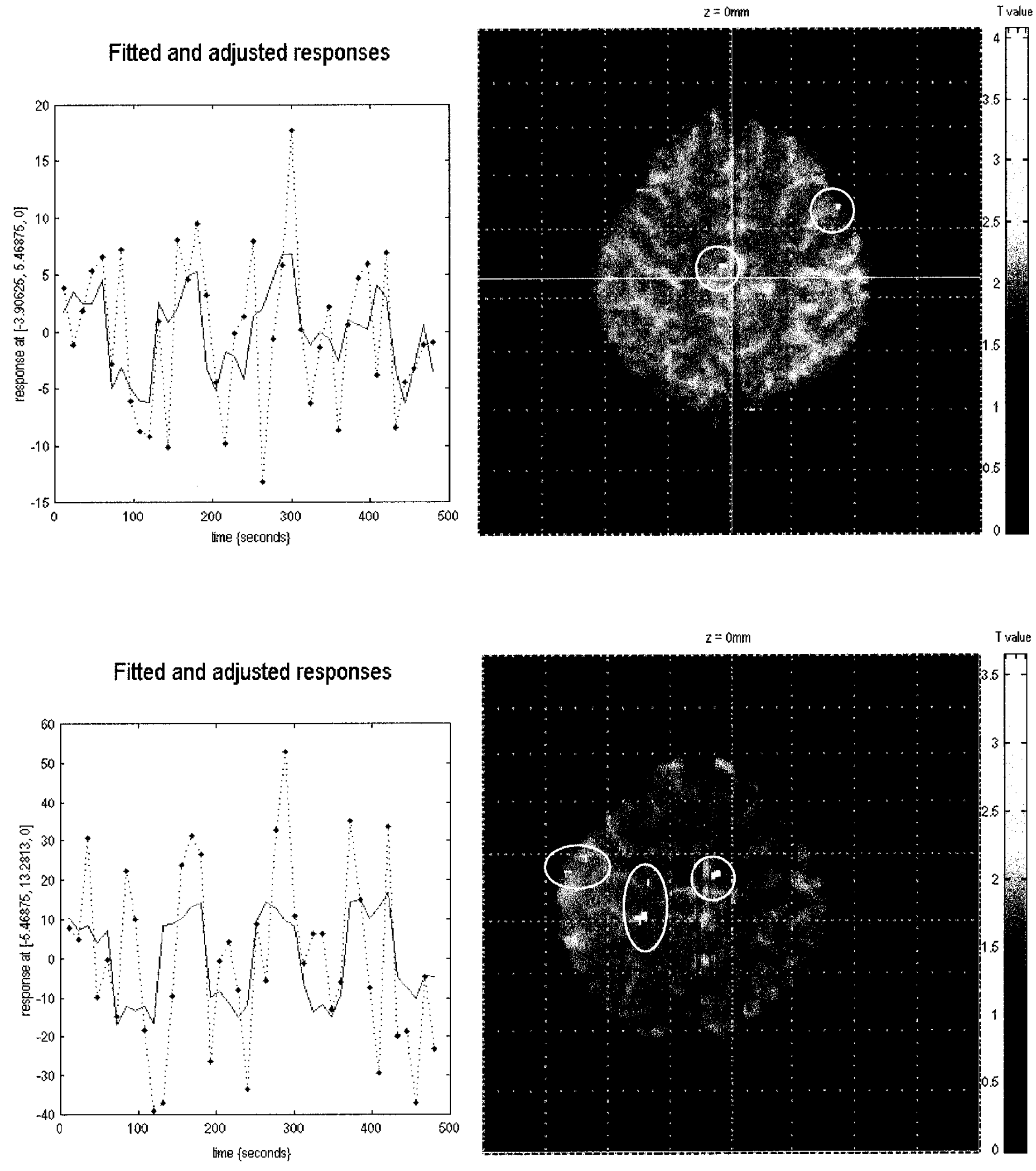

Figure 9-6. Finger tapping-induced activation at 1.5T (top) and 4.7T (bottom) for a second subject. The activation was quite sparse in this subject reflecting the fact that brain activation patterns are unique to each individual. The statistically significant voxels are circled. The timecourses are taken from the active voxel located in the centre of the brain.

9.3.3 Discussion

The strengths of conducting functional MRI studies at higher fields are clearly evident from Figures 9-5 and 9-6. Qualitatively, compared to 1.5T, at 4.7T the activation is more widespread, and one would expect less localized to draining veins, although this was not explicitly tested in the present experiment. This increased activation cannot be attributed to head motion (false activation), since the data were modeled to remove this component of signal variance. In addition, the respective timecourses, reflecting the percent whole brain signal change$_2$ of the most statistically significant single voxel within the activated region of interest, clearly demonstrate the increased sensitivity to the BOLD effect at higher field strengths. The percent BOLD signal change at 4.7T was twice that of 1.5T on average, with some voxels showing even 4 times as great a response.

9.4 Conclusion

There are several reasons to conduct functional magnetic resonance imaging studies at 4.7T including greater signal-to-noise, greater functional contrast-to-noise and increased specificity. Although the magnetic field homogeneity was insufficient for EPI sequences, gradient echo sequences were able to capture robust activation during a finger-tapping task. Despite the longer acquisition time, the gradient echo results were not degraded by subject motion. These data suggest that functional imaging at 4.7T is not only feasible, but highly advantageous even when using gradient echo imaging.

9.5 Endnotes

1. The 4.7T system is not inherently capable of executing multiple consecutive measurements in a batch process, instead each scan must be individually executed by the user. It took the computer about 8 seconds to reconstruct the previous image and to process the next acquisition command. This delay had no negative effects (interscan movement was comparable to that at 1.5T), nevertheless, subsequent to this experiment a macro was programmed to allow for multiple consecutive single slice measurements, for any similar future studies.

2. The percent signal change is found by dividing the voxel signal intensity, by the mean intensity of all of the voxels in the brain over the entire session, and multiplying the result by 100.

9.6 References

Gati, J.S., Menon, R.S., Ugurbil, K., Rutt, B.K. Experimental Determination of BOLD Field Strength Dependence in Vessels and Tissue. Magnetic Resonance in Medicine 38:296-302 (1997)

Chapter 10

Conclusion and Future Directions

The research conducted in this thesis encompassed both the clinical application of functional magnetic resonance imaging (fMRI) in the study of Parkinson's disease at 1.5T, and also the investigation of the feasibility of fMRI at 4.7T. Work at each field strength led to the advancement of functional magnetic resonance research at the University of Alberta.

Several important results were derived from the clinical project at 1.5T. Although the optimal smoothing filter size has been investigated for cortical areas (Hopfinger), no such guidelines exist for specific subcortical regions like the basal ganglia. If the extent of smoothing is too great, the signal can be lost due to partial volume effects, while minimal smoothing suffers from decreased SNR and a decreased overlap of analogous anatomical areas across subjects confounding group analysis. A study in this thesis examined the optimal smoothing extent for basal ganglia activation in fMRI studies, revealing a 4mm FWHM filter size to be optimal.

A related question of interest concerned the optimal echo time for basal ganglia (BG) studies at 1.5T. Basal ganglia percent BOLD signal change is ~1% at 1.5T (Scholz 2000) – one third of that typically found in cortical areas. Furthermore, iron accumulation has been noted in the basal ganglia in healthy subjects. This information suggests that the presence of this paramagnetic agent could be creating a particularly short relaxation time such that typical echo times used to monitor cortical activity were sampling the transverse signal once most of the BG signal had already decayed, thereby explaining the observation of a 1% signal change. A study was conducted that compared the echo time to the observed basal ganglia activation, revealing the optimal echo time value was 50ms.

The present work extended optimization beyond the realm of parameter selection by implementing software revisions to existing code to simplify tedious processing steps, to allow for multiple consecutive measurements and to reduce the acoustic noise at 4.7T. The process of attaching anatomical labels to SPM-identified clusters requires a tedious series of simple steps. Through programming revisions to the SPM file spm_list.m, these steps are now conducted automatically by Matlab.

Additional software improvements, this time to the Varian sequence programming of the 4.7T system, made multiple single-slice measurements possible. Due to shoddy product development, none of the Varian imaging sequences are able to collect multiple images. In order to collect more than one image of the same slice, one must repeatedly re-enter single image acquisition commands. This approach is particularly inefficient timewise, due to command processing and parameter setup delays. For example, the average delay between successive measurements acquired this way was about 8 seconds. A macro was created, "measurements2", which instead allows for multiple acquisitions of the same slice, at a fraction of this delay, and it may be used in conjunction with any imaging sequence.

Acoustic noise is a potential safety hazard and is greatest in sequences involving rapid gradient switching – sequences like echo planar imaging. The level of acoustic noise generated by the 4.7T research magnet was unknown. In this thesis the maximum levels of acoustic noise produced by the 4.7T system were quantified, in order to ascertain whether pre-existing headgear provided adequate hearing protection. The maximum acoustic noise observed was 128dB, which was narrowly met by the 129dB safety tolerance provided by using both earplugs and headphones. Revisions to the EPI sequence (Varian programming language) allow for user-specified reductions in the rate of the gradient switching thereby reducing the acoustic noise. For example, doubling the rise time reduced the acoustic noise to 120dB, while quadrupling it reduced the noise to 112dB.

The creation of a trigger circuit to precisely control stimulus timing has made event-related functional MRI (efMRI) possible at the University of Alberta. EfMRI offers several key advantages to conventional epoch-based designs including controllable context, randomization of trials, and allowance for oddball experiments and post-hoc processing. However, in efMRI, one must know precisely when each stimulus was applied in order to model the data properly, and thereby generate meaningful results. Existing paradigm presentation software at the University of Alberta exhibited fluctuating timing, unsuitable for this purpose. A circuit was created synchronizing the stimulus presentation to the MRI scanner, thereby providing precise stimulus timing control. This circuit makes efMRI feasible and the scanner synchronization has the added benefit of allowing accurate user-specified oversampling of the hemodynamic response function.

Clinical research on the 1.5T system investigated the functional activation in Parkinson's patient using both an event-related response inhibition paradigm and a block-based motor-switching task. Results from the event-related study (also known as the Garavan study because it recreated an experiment by Garavan 1999) did not meet statistical significance. This is an example in which a negative finding nevertheless furthers our understanding of efMRI – in particular this experiment helps establish a minimum number of stimuli required in an event-related experiment. Despite the results not reaching statistical significance, they nevertheless provide evidence suggesting differences in the way that the Parkinsonian brain processes inhibition, and confirm previous findings of inhibition abnormality in Parkinson's patients (Franz 2002). Different cortical networks were involved in response inhibition in Parkinson's patients compared to healthy controls. These differences may account for the presence of Parkinson's symptoms such as resting tremor or bradykinesia.

As opposed to the Garavan study, the motor-switching experiment (based upon Scholz 2000) focused exclusively on the basal ganglia (BG). Neurodegeneration within one nucleus of the BG, the substantia nigra, creates a dopamine deficiency which gives rise to Parkinson's symptoms. However, little research to date has examined the functional behaviour of other nuclei in the BG. The present study found the caudate nucleus, globus pallidus and putamen to be relatively underactive in Parkinson's patients compared to healthy controls during motor switching. These results confirm isolated findings by others demonstrating that functional impairment extends across the basal ganglia in Parkinson's patients.

Finally, this thesis investigated the feasibility of functional magnetic resonance imaging at 4.7T. Sufficient magnetic field homogeneity could not be attained for echo planar imaging sequences, whose images suffered from severe geometric distortion. Artifacts were reduced however, by using spin-echo EPI as opposed to gradient-echo EPI. Single echo techniques such as conventional gradient echo imaging were much more robust in the presence of inhomogeneities than EPI, as demonstrated both in phantoms and in vivo. It was also discovered through extensive testing, that the pre-existing Varian shimming sequence, FASTMAP, was not capable of shimming properly. Instead a better approach was to use the more time-consuming and user-involved method of manually shimming (first and second orders) on a slice of interest.

The exciting finding of the 4.7T research was that although magnetic field inhomogeneities necessitated the use of gradient echo functional imaging instead of echo planar techniques, there were clear advantages in conducting functional studies at high field strengths. A comparison of 1.5T and 4.7T functional activation data showed an approximate twofold increase in % BOLD signal change between rest and activation and a greater spatial extent of perceived activation at 4.7T. Furthermore, despite using the slower gradient echo techniques, the increased activation cannot be attributed to subject head motion. Although not explicitly tested, the 4.7T activation should also be more localized to the actual site of neuronal activation, and one would expect a greater signal-to-noise ratio at this field strength. These observations from the first demonstration of fMRI at 4.7T at the University of Alberta, strongly encourage future studies at this field strength.

From the conclusions presented above, several directions for future research at the University of Alberta become apparent. At 4.7T, the most obvious of these is that improvements in shimming should be pursued in order to allow for EPI imaging at 4.7T, since fast imaging techniques reduce the likelihood of subject motion artifacts and allow for whole head imaging in a reasonable amount of time. In the mean time however, gradient echo fMRI should be pursued at 4.7T on the basis of the significant increases in SNR and BOLD sensitivity available over 1.5T functional imaging.

The results from both Parkinson's studies should be followed up with subsequent experiments. The response inhibition experiment should be repeated using a new format that is devoid of a working memory component which may have confounded results, and that contains significantly more inhibition stimuli thereby yielding stronger statistical results and minimizing susceptibility to the oddball effect. The switching task should be followed up with an experiment containing three or four separate tasks known to elicit basal ganglia activation, in order to further identify the particular role played by the caudate nucleus and putamen. This would allow one to determine whether or not the BG nuclei are consistently less activated in Parkinson's patients than in controls, as opposed to a task-specific lack of functional connectivity, and may highlight a link between a particular nucleus' hypoactivity and a specific Parkinson's symptom.

10.1 References

Franz, E.A., Miller, J. Effects of response readiness on reaction time and force output in people with Parkinson's disease. Brain 125: 1733-1750 (2002)

Garavan, H., Ross, T. J., Stein, E. A. Right hemispheric dominance of inhibitory control: An event-related functional MRI study. Proc. Natl. Acad. Sci. USA (1999) 96:8301-8306

Hopfinger, J.B., Buchel, C., Holmes, A.P., Friston, K.J. A Study of Analysis Parameters That Influence the Sensitivity of Event-Related fMRI Analyses. NeuroImage 11:326-333 (2000)

Scholz, V.H., Flaherty, A.W., Kraft, E., Keltner, J.R., Kwong, K.K., Chen, Y.I., Rosen, B.R., Jenkins, B.G. Laterality, somatotopy and reproducibility of the basal ganglia and motor cortex during motor tasks. Brain Research 879 (2000) 204-215

Appendix A – Excitation

It has been shown that a proton's spin angular momentum is aligned either parallel or anti-parallel to an external applied magnetic field, with slightly more protons in the parallel configuration, creating a net magnetization in the z (or $\mathbf{B_0}$) direction. (see section 2.2.1.1)

In order to simplify the explanation of Excitation, it will be presented in reverse order beginning with the behaviour of the magnetization vector in the transverse plane (thus tipping M_z into the xy plane will be dealt with later).

The magnetization vector, now denoted M_{xy}, experiences a torque given by

$$T = \mathbf{M_{xy}} \text{ X } \mathbf{B_0} \qquad (1)$$

From quantum mechanics, the nuclear spin angular momentum $\mathbf{I}\hbar$ is related to the component of the magnetic dipole momentum along the z axis, μ, by

$$\mu / \mathbf{I}\hbar = \gamma \qquad (2)$$

In addition, the angular analogue of Newton's Laws relates torque to the change in angular momentum. Putting this together,

$$T = d/dt\,(\Sigma\mathbf{I}\hbar) = d/dt(\Sigma\mu/\gamma) = (1/\gamma)d/dt\,\mathbf{M_{xy}} = \mathbf{M_{xy}} \text{ X } \mathbf{B_0} \qquad (3)$$

Expanding the cross product

$$d/dt\,\mathbf{M_{xy}} = \gamma[M_yB_0\mathbf{i} - M_xB_0\mathbf{j}] \qquad (4)$$

Or instead in complex notation with $M_{xy} = M_x + iM_y$

$$d/dtM_{xy} = \gamma B_0[M_y - iM_x] = -i\gamma B_0M_{xy} \qquad (5)$$

Solving the differential equation in Eqn (5) yields the general solution

$M_{xy} = K\exp(-Ct)$ (6)

Using the initial condition that $M_{xy}(t=0) = iM_0$ (i.e. $M_{xy}(t=0)$ lies on the y-axis) $K= iM_0$. Likewise, inserting (6) into (5) reveals that $C = -i\gamma B_0$

Thus $M_{xy}(t) = iM_0\exp(-i\gamma B_0t)$ (7)

This reveals that the frequency of precession about the z axis is equal to γB_0, known as the Larmor frequency, and is in the negative sense.

Now to step back in order to explain how the net magnetization is tipped from the z axis into the transverse plane.

Begin with the equation of motion derived above, namely

$d\mathbf{M}/dt = \gamma(\mathbf{M} \times \mathbf{B})$. Using a static reference frame $\mathbf{B_0} = B_0\mathbf{k}$ and $\mathbf{B_1}(t) = \mathbf{i}B_1\cos\omega t + \mathbf{j}B_1\sin\omega t$

Thus

$$d\mathbf{M}/dt = \gamma \begin{vmatrix} Mx & My & Mz \\ B1\cos\omega t & B1\sin\omega t & B_0 \end{vmatrix} \qquad (8) \quad \text{and}$$

$dM_x/dt = \gamma[M_yB_0 - M_zB_1\sin\omega t]$ (9)

$dM_y/dt = \gamma[M_zB_1\cos\omega t - M_xB_0]$ (10)

$dM_z/dt = \gamma[M_xB_1\sin\omega t - M_yB_1\cos\omega t]$ (11)

Equations 9-11 portray rotation of the magnetization vector, under the influence of $\mathbf{B_1}(t)$ and $\mathbf{B_0}$, about both the transverse axes and the longitudinal axis. In order to simplify conceptualization of such motion, an alternate frame of reference is adopted – one that rotates about the z-axis with the frequency and sense of $\mathbf{B_1}(t)$. In this rotating frame, both $\mathbf{B_0}$ and $\mathbf{B_1}$ are static.

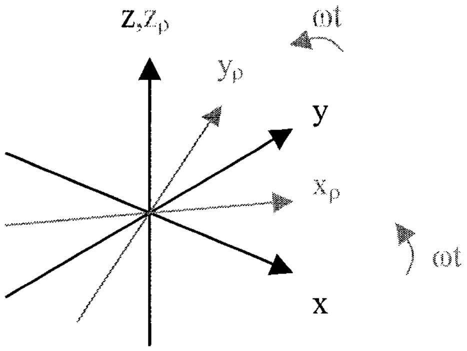

Figure A-1. Static (black) versus the rotating (gray) frames of reference. The rotating axes are identified by the subscript ρ.

Relating these two coordinate systems we get

$$M_{x\rho} = M_x\cos\omega t + M_y\sin\omega t \qquad (12)$$

$$M_{y\rho} = -M_x\sin\omega t + M_y\cos\omega t \qquad (13)$$

Differentiating these with respect to time and substituting for dM_x/dt and dM_y/dt from (9) and (10) we get

$$dM_{x\rho}/dt = (\gamma B_0 + \omega)M_{y\rho} \qquad (14)$$

$$dM_{y\rho}/dt = -(\gamma B_0 + \omega)M_{x\rho} + \gamma B_1 M_{z\rho} \qquad (15)$$

$$dM_{z\rho}/dt = -\gamma B_1 M_{y\rho} \qquad (16)$$

which in matrix form is

$$d\mathbf{M}_\rho/dt = \gamma \begin{vmatrix} M_{x\rho} & M_{y\rho} & M_{z\rho} \\ B_1 & 0 & (B_0 + \omega/\gamma) \end{vmatrix} \qquad (17)$$

In other words, this can be generalized as $d\mathbf{M}_\rho/dt = \gamma\, \mathbf{M}_\rho \times \mathbf{B}_{\mathrm{eff}}$
where $\mathbf{B}_{\mathrm{eff}} = \mathbf{i}B_1 + \mathbf{k}(B_0 + \omega/\gamma)$.

In this rotating frame of reference, the magnetization vector's motion is interpreted as a conical precession at frequency $\omega_{\mathrm{eff}} = \gamma B_{\mathrm{eff}}$ about a central axis equal to B_{eff}. Furthermore, prior to applying B_1 M lies on the z-axis, and thus the z-axis defines the edge of this cone. The rotation is also in the negative sense for protons.

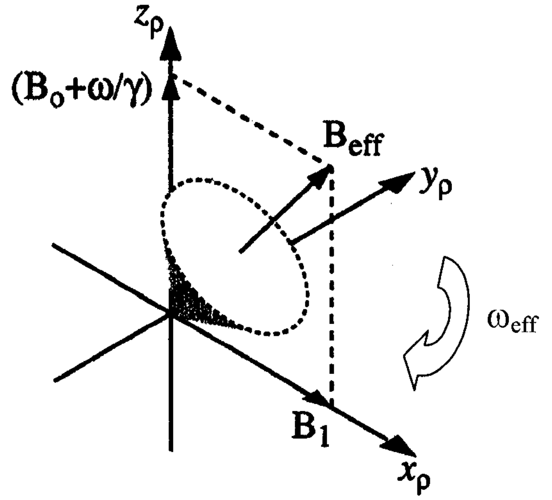

Figure A-2. Conical precession path of the Magnetization vector about the ***B_{eff}*** *axis. (Allen 1992).*

Aside from aiding visualization, the mathematical expression concerning the equation of motion for the rotating frame (17) reveals a vital point. Note that if ω (the frequency of $\mathbf{B}_1$) is chosen such that $\omega = -\gamma B_0$, the **k** terms $(B_0 + \omega/\gamma)$ cancel and the precession flattens out to a disc shape on the $y_p z_p$ plane. Now $\mathbf{B}_{eff} = \mathbf{i}B_1$ and the precession frequency is $\omega_{eff} = \gamma B_{eff} = \gamma B_1$. This condition is known as being **on resonance.**

The angle accrued by the precessing disc is given by

$$\theta = \gamma B_1 t_{rf} \qquad (18)$$

Thus the magnetization vector's position can be controlled by the duration of $\mathbf{B}_1$ application. As an example, if $\mathbf{B}_1$ is applied along the x_p -axis for $t = \pi/(2\gamma B_1)$ seconds, then **M** will be flipped onto the y_p -axis. This is perhaps the most common pulse known as a 90 degree pulse. Now that **M** lies in the transverse plane, it precesses about the z-axis, in the xy plane as described earlier. Alternatively, if $\mathbf{B}_1$ is applied for twice as long, i.e., $t = \pi/(\gamma B_1)$, then the magnetization is rotated onto the negative z axis. This is known as an inversion pulse and was discussed in section 2.3.1 pertaining to T_1 contrast.

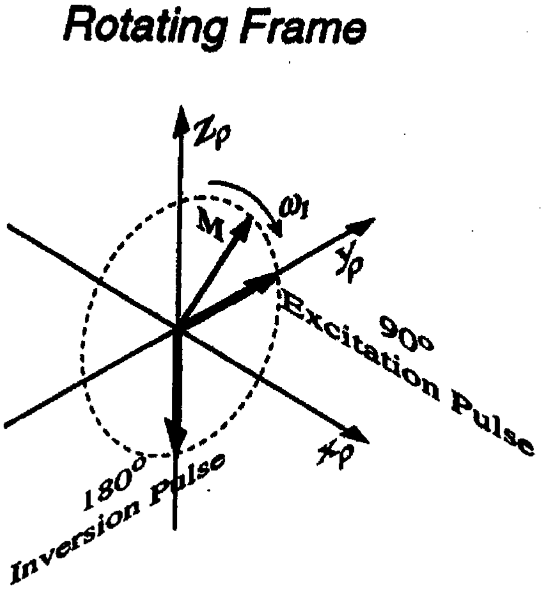

Figure A-3. Precession during the on-resonance condition. On-resonance, the conical precession flattens out to a disc shape. By appropriately choosing the time that $\boldsymbol{B}_1$ *is on, the Magnetization may be placed on the* y_ρ *axis in the transverse plane (Allen BME 564 course notes).*

Appendix B – Illustration of Spatial Encoding

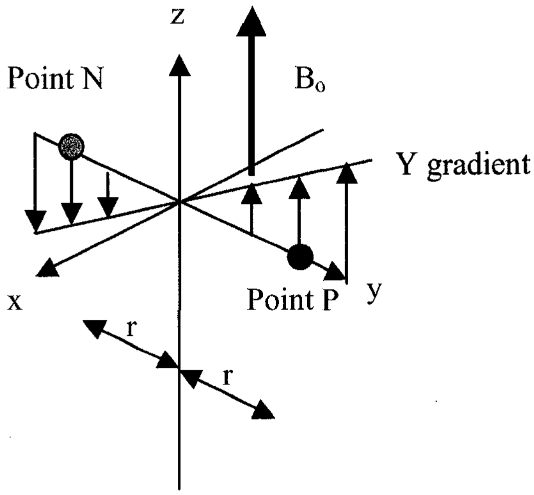

Figure B-1. Two samples exposed to a linear gradient. The two samples sense a linear gradient in the y-direction in addition to B_o.

The total field experienced by Points N (because on the Negative y-axis) and P may be expressed as
$B_N = B_o - G\bullet r$ and $B_P = B_o + G\bullet r$ where r is the distance from both P and N to the origin.

The precessional frequencies generally given as $\omega = \gamma B$ become $\omega_N = \gamma(B_o - G\bullet r)$ and $\omega_P = \gamma(B_o + G\bullet r)$ respectively. Thus the induced EMF becomes the following in frequency space:

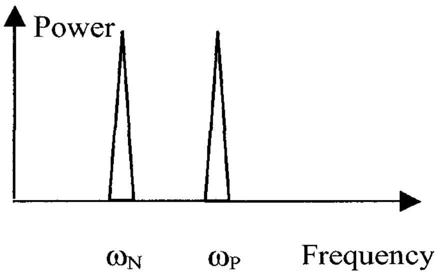

Figure B-2. Frequency space diagram for system with two separated points under the influence of a gradient.

By applying a gradient, a relationship has been established between position and the measured frequency (by $\omega \alpha G \bullet r$). Therefore measuring all of the frequencies generated by an entire object will yield information about its spatial structure. To illustrate this, carry forward the above example one step further. Suppose that point N is the signal from 1 proton, while that from P comes from 10 protons. The resulting frequency space is shown below.

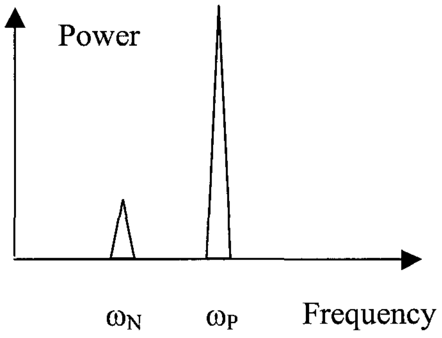

Figure B-3. Frequency space diagram showing the effects of proton density. In this instance point N has one proton, point P has 10.

Thus if a black and white image were created from the above system, the measured frequencies would be converted into positions (since $\omega \alpha G \bullet r$ and G is well known) with the intensity of the point P being much greater (whiter) than that of point N. The extension to creating an entire image is not difficult. Rather than 2 points an object will consist of hundreds.

Appendix C – Echo Time (TE) Optimization

C.1 Introduction

The Basal Ganglia (BG) is a tricky region to image: achieving consistent activation is difficult (Scholz 2000; Samuel 1998) and the task-related signal change small. At 1.5T, the BOLD signal change during activation in the BG is typically ~1% while that of other areas such as the motor cortex is closer to 3% (Scholz 2000). In addition, T_2 values of the BG nuclei are shorter than those found in the frontal cortex (Antonini 1993), attributed at least in part to the natural accumulation of iron within these regions.

In conjunction, these facts suggest that current imaging parameters, especially the echo time, may be optimal for imaging the cortex, but not the basal ganglia. Specifically, the current TE may be too long such that the basal ganglia's transverse signal has decayed too far, resulting in a very small task-related signal difference. One may speculate that by shortening TE, perhaps the BG signal can be acquired before falling off to such a small level, leading to greater observable signal (figure C-1).

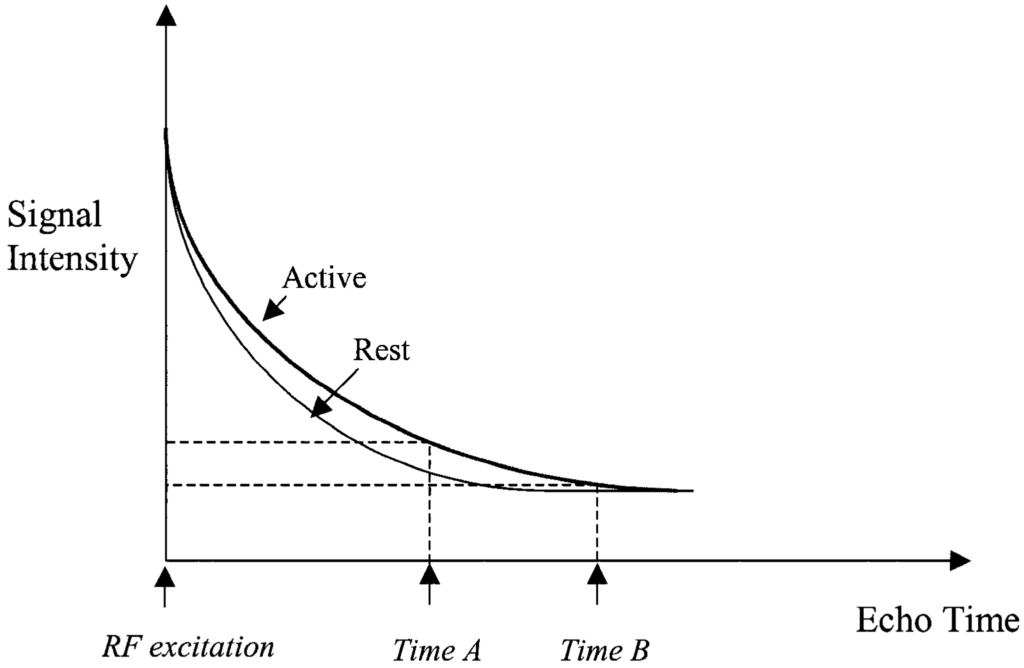

Figure C-1. Differential T_2 decay in the Basal Ganglia according to activation state. This pilot study hypothesizes that the small BOLD signal (1%) may result from too long an echo time (Time B). Perhaps a shorter TE (Time A) would sample the signal at a time where greater differential signal intensity exists between the resting and active states, leading to a >1% signal.*

Sample Experiment: Comparison of TE = 50ms vs. TE = 40ms for Imaging the Basal Ganglia

C.2 Methods

The study recruited 2 healthy male subjects. Two sets of images were acquired from each, with the echo time equal to 40ms in one case, and 50ms in the other. Subjects were asked to alternate between unilateral finger tapping and toe wiggling with all motion at a pace of 2 Hz. The experiment consisted of 30-second movement epochs alternating with 30 seconds of rest (Chapter 7 Scholz study).

The resultant data were compared on the basis of which TE elicited the most clusters that surpassed the SVC threshold in the BG. Furthermore, of those clusters that were suprathreshold, which TE evoked the maximum % BOLD signal change and the largest average % BOLD change across all epochs was also investigated.

The details of each session are included below.

Table C-1. Sequence parameters in the optimal TE pilot study data.

Subject	Stimulus	Session Duration/ # volumes collected	Sequence	Echo Time TE (ms)	Repetition Time TR (s)
A	Right, Left and Rest epochs intermingled	7min/118	Gradient Echo EPI	40	3*
A	Right, Left and Rest epochs intermingled	11min/105	Gradient Echo EPI	50	6
Y	Right vs. Rest only	6.5min/130	Gradient Echo EPI	40	6
Y	Right vs. Rest only	6.5min/130	Gradient Echo EPI	50	6

* Old data were reused in this study, therefore the TR, scan time and volume # are different in the two subject A datasets. This was deemed acceptable in that the # of volumes was similar and thus no strong statistical advantage was provided to any one image set. Secondly, even the 3 sec TR would allow sufficient time for full relaxation of BG signal, thus the difference in TR should have minimal effect other than changing the session duration.

C.3 Results

Table C-2. Activated basal ganglia clusters surpassing the small volume correction (SVC) threshold at different TEs.

Subject	Contrast	TE = 40ms			TE = 50ms		
		# of SVC BG points	Max. % BOLD of those points	Avg. % BOLD of those points	# of SVC BG points	Max. % BOLD of those points	Avg. % BOLD of those points
A	Right (movements) vs. Rest	1	1	0.9375 ±0.402	3	1.8 1.2 1.35	0.8456 ±0.4739
A	Left vs. Rest	2	1.5 1.35		2	2 2	
Y	R vs. Rest	-	N/A	N/A	-*	N/A	N/A

* No BG points surpassed the SVC threshold at either TE for subject Y. However, analysis of uncorrected data revealed BG activations in the TE = 50ms data only.

C.4 Conclusion

While the average % BOLD signal change is inconclusive, both the greater number of active clusters and the greater max % BOLD signal change within those clusters suggest that TE = 50ms is more ideal than TE=40ms for basal ganglia studies.

C.5 Additional Comments

The findings of this pilot study were later verified by Graham et al 2000 wherein the average T_2* value of all the BG nuclei is about 50ms. The largest BOLD signal change in T_2*-weighted images ensues when TE $\approx T_2^*$ (Gati 1997; Clare et al 2001). In combination, these works are in agreement with the above conclusion that the optimal TE for imaging the basal ganglia is about 50ms.

C.6 References

Antonini, A., Leenders, K.L., Meier, D., Oertel, W.H., Boesiger, P., Anliker, M. T2 relaxation time in patients with Parkinson's disease. Neurology: 697-700 (1993)

Clare, S., Francis, S., Morris, P.G., Bowtell, R. Single-Shot T_2* Measurement to Establish Optimum Echo Time for fMRI: Studies of the Visual, Motor, and Auditory Cortices at 3.0T. Magnetic Resonance in Medicine 45:930-933 (2001)

Gati, J.S., Menon, R.S., Ugurbil, K., Rutt, B.K. Experimental Determination of BOLD Field Strength Dependence in Vessels and Tissue. Magnetic Resonance in Medicine 38:296-302 (1997)

Graham, J.M., Paley, M.N.J., Grunewald, R.A., Hoggard, N., Griffiths, P.D. Brain iron deposition in Parkinson's disease imaged using the PRIME magnetic resonance sequence. Brain 123: 2423-2431 (2000)

Samuel, M., Williams, S.C.R., Leigh, P.N., Simmons, A., Chakraborti, S., Andrew, C.M., Friston, K.J., Goldstein, L.H., Brooks, D.J. Exploring the temporal nature of hemodynamic responses of cortical motor areas using functional MRI. Neurology 51(6):1567-1575 (1998)

Scholz, V.H., Flaherty, A.W., Kraft, E., Keltner, J.R., Kwong, K.K., Chen, Y.I., Rosen, B.R., Jenkins, B.G. Laterality, somatotopy and reproducibility of the basal ganglia and motor cortex during motor tasks. Brain Research 879: 204-215 (2000)

Appendix D – Minimizing the Steps between Cluster Identification in SPM and Anatomical Labelling with the Talairach Daemon: a Matlab Software Solution

The end result of statistical analysis using SPM99 is a list of voxels surpassing a specified threshold, in decreasing statistical significance. Included within this list are the voxels' corresponding P-values, T statistics, cluster sizes, etc.

In functional studies, results are more informative if anatomical labels can be attached to the activated voxel coordinates. SPM is based on an anatomical template created by the Montreal Neurological Institute. The labelling program used in this thesis, the Talairach Daemon, is grounded in the slightly different template of Talairach and Tournoux. Therefore, one must convert SPM voxels into Talairach co-ordinates before using the Daemon. Several trivial steps are involved, which are tiresome and a waste of time when many datasets are analyzed.

The steps involved manually copying the voxel coordinates from the SPM table into a .txt file, reformatting the data so that a separate matlab function can convert them to Talairach coordinates, and finally re-entering this data into another .txt file required by the Talairach Daemon.

For example:

Step 1. Matlab generates a table of statistically significant voxels. This can be printed to the Matlab screen by right-clicking on the table in the SPM window and choosing "print table".

```
==================================================================
cluster cluster cluster voxel  voxel  voxel  voxel
p(cor)  equivk  p(unc)  p(cor) T      equivZ p(unc) x,y,z {mm}
------------------------------------------------------------------
0.000   305     0.000   0.000  9.24   ( 7.14) 0.000  -40   2  50
                        0.002  6.27   ( 5.42) 0.000  -42 -12  52
                        0.006  5.98   ( 5.22) 0.000  -32  10  56
0.000   160     0.000   0.000  7.52   ( 6.20) 0.000   54  14  -2
0.000   50      0.001   0.000  6.92   ( 5.84) 0.000  -30 -58 –28
```

Step 2. The user manually enters the coordinates from Matlab into new .txt file.

```
1. –40 2 50
2. –42 –12 52
3. –32 10 56
4. …
```

Step 3. User reformats the data so that it can be used by the matlab command "mni2tal" which converts MNI coordinates to Talairach coordinates. (This is basically changing a column of coordinates into a row and inserting semi-colons as spacers)

```
1. –40 2 50 ; –42 –12 52; –32 10 56 …
2.
3.
4.
```

In Matlab

```
>>round(mni2tal([-40 2 50; -42 –12 52; -32 10 56…]))
```

Step 4. User enters the adjusted co-ordinates as a single column within a .txt file, as this is the file type and format required by the Talairach Daemon (the program that attaches an anatomical label to the coordinates).

```
1.      –40 4 46
2.       –42 –9 48
3.       –32 12 51
4.      …
```

Output from Talairach Database:

Record Number	X coor	Y coor	Z coor	Level 1	Level 2	Level 3	Level 4	Level5
0	-40	4	46	Left Cerebrum	Frontal Lobe	Middle Frontal Gyrus	White Matter	*
1	-42	-9	48	Left Cerebrum	Frontal Lobe	Precentral Gyrus	White Matter	*
2	-32	12	51	Left Cerebrum	Frontal Lobe	Superior Frontal Gyrus	White Matter	*

A number of these trivial steps were eliminated by modifying a pre-existing Matlab file, spm_list.m. Now when the user chooses to print the SPM MNI table to the screen (by right clicking the mouse and choosing print table (step 1)), the revised program automatically conducts steps 2-4, saving the result in F:\input.txt. The final step, as before, requires manual operation of the Talairach Daemon. This Matlab code is an extension of a pre-existing file and thus is easy to implement and easily transferable to other machines.

Appendix E - Determination of Optimal Smoothing Extent for BG Studies

This section summarizes the procedure used to determine the optimal smoothing extent for the recreated Scholz experiment (Chapter 7), which investigated functional activation in the basal ganglia (BG).

E.1 Background

Section 5.4.5 expounded the reasons to smooth data - the next decision concerns how much to smooth the data. This issue is currently being debated with some suggesting that the smoothing kernel's FWHM should be at least 2 to 3 times the voxel size (after normalization). Others have instead suggested that the size of the smoothing filter should be matched to the extent of the signal, i.e., if you expect a 10mm activation, use a 10mm filter. Unfortunately, the latter thought doesn't provide any clear direction in the present context, since the extent of basal ganglia activation has not been defined elsewhere. Greater smoothing increases SNR but at the risk of losing the signal entirely by partial volume effects if the source is highly localized, as it may be in the small structures of the basal ganglia.

E.2 Methods

E.2.1 Single Subject Analysis

In order to choose the optimal filter size, two subjects' datasets were fully analyzed using smoothing filter sizes ranging from 4 to 10mm. The filters were evaluated according to the resultant number of surviving BG clusters. The uncorrected datasets are shown below (figure E-1 and Table E-1).

E.2.2 Group Analysis

Single subject analysis identifies the smoothing extent best suited for detecting multiple BG activations within a single dataset, and additionally suggests the spatial extent of BG activations. However, the goal of the present research is to conduct group analysis, thus eliciting many activations becomes secondary to eliciting activations from the same BG pixel in all subjects. Therefore a second experiment tested the optimal smoothing level for fixed effects group analysis. In this study, 3 subjects' data$_1$ were smoothed at 4mm, 6mm and 8mm and analyzed using the FFX model (Table E-2).

E.3 Results

E.3.1 Single Subject Analysis

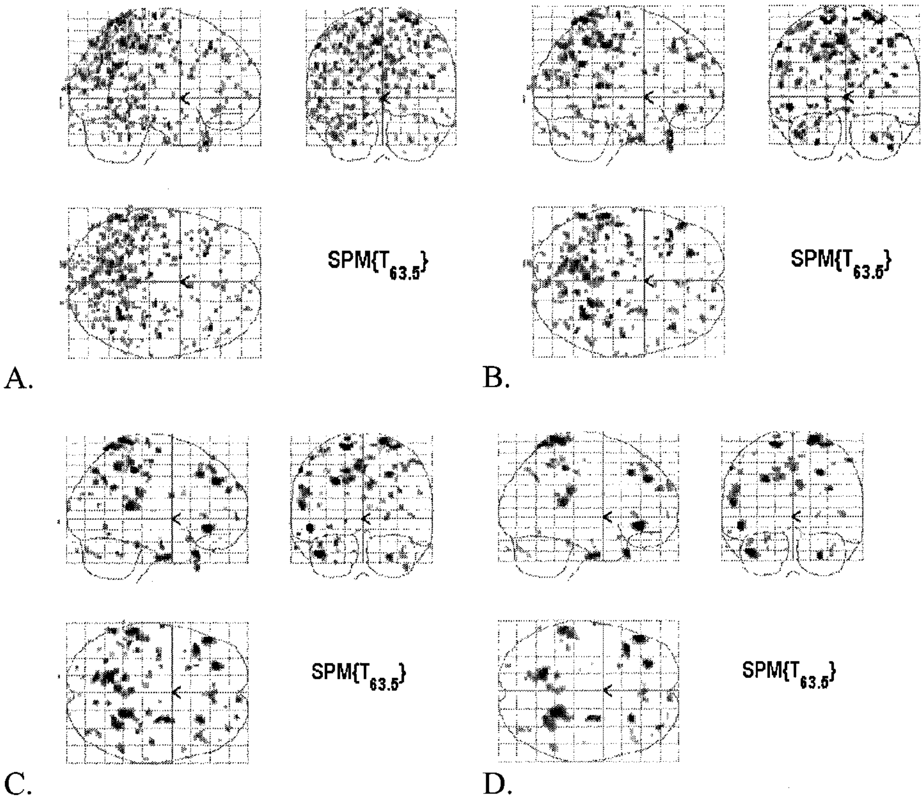

Figure E-1. A single subject's data (Scholz experiment recreated, uncorrected p-values), analyzed at four different smoothing extents. The data were smoothed to A) 4mm B) 6mm C) 8mm and D) 10mm.

Table E-1. Active basal ganglia clusters (uncorrected) across 2 subjects at different levels of smoothing

	4mm		6mm		8mm		10mm	
	Co-ords	Area	Co-ords	Area	Co-ords	Area	Co-ords	Area
Subject K (L_ Scholz)	20, 10, 14 18, 20, 6	R putamen* R Caudate**	-	-	N/A	N/A	N/A	N/A
Subject M (R_ Scholz)	6, 8, 9 -18,-10, 2	R Caudate Body L medial GP	6, 8, 9	R Caudate Body	N/A	N/A	-	-

*,** Exact region is the Right Cerebrum,Sub-lobar,Extra-Nuclear,White Matter,*, in other words a non-specific region likely not the site of the neuronal activity. The nearest gray matter area is indicated (within *(5mm) and **(3mm) of the coords)

E.3.2 Three subject Group FFX Analysis

Table E-2. The number of clusters within the basal ganglia that were either activated (task>rest) or deactivated (rest>task) in a 3-subject FFX analysis

Smoothing Extent (mm)	# BG Activation Points	# BG Deactivation Points
4	2	1*
6	0	4
8	0	3

* This point had z = 78 i.e. likely lies outside the brain

Note that deactivation or reduction of activity during the task could represent efficient allocation of mental resources by removing unnecessary activity.

E.4 Discussion

Of the filter sizes examined, the 4mm smoothing captures the most BG points in the single subject analysis. Within the group analysis the results are a little less convincing. The 6mm smooth is better than the 8mm smooth. Although a precedent exists suggesting that reduced activation (or deactivation) could indicate more efficient allocation of brain resources (Mattay 2002) the evidence came from a study on the prefrontal and parietal cortices of dopamine deplete Parkinson's patients. To my knowledge this reduced activation implying better efficiency has not been shown in the BG. Furthermore, the experiment by Scholz (Scholz 2000, upon which this study is based) reported only BG activation and not deactivation. As a result, the deactivation points should not have been considered at all. Using the activation points only, the group analysis echoes the conclusion that the 4mm smooth is optimal.

Finally, other scientists' pre-processing parameters were reviewed for comparison and further insight. Hopfinger (2000) varied several parameters and found optimal smoothing in particular, in an efMRI experiment, to be 10 mm. Unfortunately, Hopfinger's results are not entirely relevant as our regions of interest differed. In studies procuring BG activity either by intent or inadvertently, the consensus appears to be a smoothing level of about 4 mm (Cunnington 2002 (4mm), Garavan 1999 (4.2mm), Menon 2000 (4mm)).

E.5 Conclusion

Based upon both the observed results and the methods used by others, a 4mm smooth seems optimal and furthermore satisfies the standard of smoothing to twice or three times the voxel size of the normalized images (which here were 2mm).

E.6 Endnotes

1. The study used motion UNCORRECTED (i.e. normal non-moco) data from 3 subjects each of whom had shown good individual BG results (Koles series 06, Maria 08 and Paulette 08).

E.7 References

Cunnington, R., Windischberger, C., Deecke, L., Moser, E. The Preparation and Execution of Self-Initiated and Externally-Triggered Movement: A Study of Event-Related fMRI. NeuroImage 15:373-385 (2002)

Garavan, H., Ross, T. J., Stein, E. A. Right hemispheric dominance of inhibitory control: An event-related functional MRI study. Proc. Natl. Acad. Sci. USA (1999) 96:8301-8306

Hopfinger, J.B., Buchel, C., Holmes, A.P., Friston, K.J. A Study of Analysis Parameters That Influence the Sensitivity of Event-Related fMRI Analyses. NeuroImage 11:326-333 (2000)

Mattay, V.S., Tesitore, A., Callicott, J.H., Bertolino, A., Goldberg, T., Chase, T.N., Hyde, T.M., Weinberger, D.R. Dopaminergic Modulation of Cortical Function in Patients with Parkinson's Disease. Ann Neurol 2002;51:156-164

Menon, V., Anagnoson, R.T., Glover, G.H., Pfefferbaum, A. Basal ganglia involvement in memory guided movement sequencing. NeuroReport 11(16):3641-3645 (2000)

Scholz, V.H., Flaherty, A.W., Kraft, E., Keltner, J.R., Kwong, K.K., Chen, Y.I., Rosen, B.R., Jenkins, B.G. Laterality, somatotopy and reproducibility of the basal ganglia and motor cortex during motor tasks. Brain Research 879 (2000) 204-215